Stress-induced Damage and Post-fire Response of Aluminum Alloys

Yanyun Chen

Dissertation submitted to the faculty of the Virginia Polytechnic Institute and State University in partial fulfillment of the requirements for the degree of

Doctor of Philosophy
in
Engineering Mechanics

Scott W. Case, Co-Chair
Brian Y. Lattimer, Co-Chair
Norman E. Dowling
Raffaella De Vita
Matthew R. Eatherton

December 1st, 2014

Blacksburg, Virginia

Keywords: Stress-induced damage; Cavitation; Grain Elongation; Dynamic Recrystallization; Residual Strength; Fire Response

Stress-induced Damage and Post-fire Response of Aluminum Alloys

Yanyun Chen

ABSTRACT

Aluminum alloys have increasing applications in construction and transportation industries. Both 5xxx-series (Al-Mg) and 6xxx-series (Al-Mg) alloys are frequently used in marine construction because of their light weight, high strength, and corrosion resistance. One of the major concerns regarding the marine application of aluminum alloys is their mechanical performance in fire scenarios. The material strength may be degraded due to both thermal and mechanical damage during fire exposure.

This work emphasizes the stress-induced mechanical (physical) damage and its impact on the residual (post-fire) performance of 5083-H116 and 6061-T651 aluminum alloy. Thermo-mechanical tests were performed at various temperatures and stresses to study the stress-induced damage at induced plastic creep strain levels. Unstressed thermally exposed and thermo-mechanically damaged samples were examined to separate the stress-induced microstructural damage. The stress-induced microstructural damage primarily manifests itself as dynamic recovery at low creep temperatures, while cavitation, dynamic recrystallization and dynamic precipitation (in Al6061) are the types of damage developed in the high creep strains at high exposure temperatures. Different creep mechanisms are also studied for both Al5083 and Al6061.

The post-fire mechanical response at room temperature after thermo-mechanical damage was investigated with reference to the damaged microstructure present in the material. Residual material strengths based on deformed cross sectional area after the creep test were calculated to provide insight into how microstructural damage affects the post-fire material performance. The competing effects of strength degradation caused by cavitation and strengthening due to grain elongation and subgrain refinement were investigated. Engineering residual material strengths calculated based on the original cross sectional area prior to creep tests were also studied to provide guidance for structural design.

Dedication

This work is dedicated to my family and friends for their unstinting support throughout all my academic and personal endeavors. Their optimism, encouragement and generous help provide me abundant confidence to fulfill all the goals in my life.

Acknowledgements

I would like to acknowledge my advisors, group members and committee members for your great support in my completion of this work. Without the guidance from advisors, the help from group mates and friends, and the support from my family, I would never have been able to finish my Ph.D. dissertation.

I would like to express my deepest gratitude to my primary advisor, Dr. Case. Thank you for provide me valuable suggestions during this work. I really appreciate your patience and guidance on all the problems in my research. As a mentor, you've not only help me improve the experimental skills and develop my understanding in aluminum research, but also help me extend my background in material science and finite element analysis. Your positive attitude and intelligence towards difficulties and solving problems will also benefit me in my future work.

I also feel deeply grateful to my co-advisor, Dr. Lattimer. Thank you for introducing me to the field of thermo-mechanical material response. Your abundant experience in thermal analysis has given me effective guidance on experimental design and microstructure analysis. As an engineer, your professional rigor deeply impressed me throughout my graduate study and will help me grow into a qualified engineer in the future.

Patrick, thank you for being my most helpful workmate and friend during these years; you have given me plenty of invaluable advices on my research. I really appreciate your help in teaching me how to use all the experimental equipments and providing me in-time suggestions when a problem came to me. Your persistence on pursuiting knowledge and solving problems also impressed and motivated me to perform better.

Last but not least, I would like to express my thanks to Jessica, Nathan and Christian for your help with my initial test set up, DIC test system and finite element model. Also I owe my thanks to Ben, Bilel and Roozbeh, your precious friendship is irreplaceable for me. Working with you all has brought so enjoyable experience in my graduate study.

Table of Contents

List of Figures

List of Tables

Nomenclature

SYMBOL	DESCRIPTION	UNIT
H	Vickers Hardness	Kg/mm^2
E	Young's Modulus	GPa
σ_y	Yield Strength	MPa
σ_u	Ultimate Tensile Strength	MPa
m	Meyer's Hardness Coefficient	--
n	Strain Hardening Coefficient	--
T_c	Creep Temperature	ºC
σ_c	Creep Stress	MPa
ε_c	Creep Strain	mm/mm
ϕ	Cavity Volume Fraction	%
ϕ_0	Initial Cavity Volume Fraction	%
η	Growth Parameter	--
$\sigma_{0.2\%\_T}$	Post-fire True Yield Strength	MPa
σ_{ult_T}	Post-fire True Ultimate Tensile Strength	MPa
$\sigma_{0.2\%\_E}$	Post-fire Engineering Yield Strength	MPa
σ_{ult_E}	Post-fire Engineering Ultimate Tensile Strength	MPa
ε_{ult}	Post-fire Ultimate Tensile Srength	%

CHAPTER 1- Introduction

1.1 Background

Aluminum alloys have a number of attributes leading to a wide range of structural applications including those in the aerospace, automotive, marine, and mechanical industry. These attributes include high ductility, high strength, low density, good weldability, high electrical and thermal conductivities, and the exceptional performance in extreme environments including excellent resistance to seawater and corrosive chemicals.

As "light metals", aluminum alloys are important for lightweight structural applications such as in aerospace and ship engineering. Weight is a very important factor in ship construction. Low weight can greatly improve the vessel speed and the transport payload weight [1]. Compared to the most popular conventional structure material, steel, which has been widely used in shipbuilding due to its high strength and low cost, aluminum alloys overwhelm the major drawback in steel ship construction: the considerable weight. Thus aluminum alloys have been applied in marine structures for more than one hundred years and admit weight reduction in ships by over 50%.

Aluminum has been applied in shipbuilding since 1891. A steam passenger boat designed to carry 8 passengers was partially constructed from aluminum in Switzerland. Three years later, in 1894, a 58-m motor torpedo boat made of aluminum was manufactured for the navy of the Russian Empire. This boat broke the speed record at that time, reaching 32 knots. In 1895, another aluminum boat won the America's Cup, one of the most prestigious regattas in America. This award was the final proof of the advantages of aluminum as a ship construction material. However, high cost and corrosion were discovered as two drawbacks at that time. Studies of aluminum alloy properties were then initiated in the early 20^{th} century and primarily focused on the issue of aluminum corrosion in seawater. Magnesium and silicon were added as alloying elements to improve the corrosion resistance of aluminum. By the 1960s, the technology was improved to reduce the cost of aluminum manufacturing. These improvements overcame many of the disadvantages of aluminum and then led to a wide range of applications in ship

construction. Making use of aluminum alloy in shipbuilding greatly reduced the maintain cost of the vessels, also reducing the total weight and increasing the speed and carrying capacity [1].

Al5083-H116 and Al6061-T651 are two frequently used marine-grade aluminum alloys. Al5083-H116 is a work-hardened alloy containing 4 - 4.9% of magnesium as its major alloying element. It was registered by Aluminum Association in 1954 and considered the base alloy of shipbuilders. Al 6061-T651 is a precipitation hardened aluminum alloy, in which the major alloying elements are 0.8 – 1.2% of magnesium and 0.4 – 0.8% of silicon. The properties including light weight, high strength, corrosion resistance, and excellent welding characteristics of Al5083-H116 and Al6061-T651 make them popular in shipbuilding. However, the melting point and ignition temperature of aluminum are significantly lower than those of steel. An additional potential concern with the application of aluminum is the possibility of fire exposure. Several fires occurred in the 1970s involving ships that had aluminum superstructures. One of the cases is USS Belknap, the lead ship of the guided missile cruiser in US Navy. The Belknap caught fire after a collision with another naval ship in heavy weather in 1975. During the fire the aluminum superstructure on the Belknap was melted, burned and gutted to the deck level resulting in the death of seven persons in this serious incident [2]. The most recent example is the case of the Navy patrol boat HMAS Bundaberg which caught fire while undergoing routine maintenance in Brisbane, Australia on August 11th, 2014; the damage assessment of the patrol boat to determine the vessel's future is still ongoing [3]. Thus, for future application of aluminum alloy in ship construction, the fire resistance is an important factor to be considered. The evaluation of the strength of aluminum alloy subjected to high temperature exposure and mechanical loading is urgent in ship manufacturing. From those evaluations the post-fire performance of the aluminum structures can be estimated and the premature structure failure can be avoided.

When subjected to fire conditions, the performances of aluminum structures may be affected by the high temperature exposure. A preliminary study indicates that the elevated temperature mechanical properties for both alloys exhibit significant degradation during thermal exposure [4]. Moreover, permanent changes will take place in the microstructure after material exposure to fire and return to ambient temperature, which is termed as the post-fire damage. The microstructural evolution and precipitation sequence associated with the increase of temperature provide evidence for the thermally-induced damage in the material. Grain recrystallization and

precipitation evolution are discussed as the primary causes of material strength degradation for Al5083 and Al6061 respectively. The kinetics of grain recrystallization and precipitation also explain the post-fire behavior dependence on the heating rate in the absence of stress [5]. However, these internal fire damage generated in the stress-free structures is solely caused by the high temperature exposure during fire. The stress effect on microstructural damage and post-fire response in the load-bearing aluminum structures has not been accounted yet.

For a load-bearing aluminum structure, stress is an important factor to accelerate the microstructure damage and the residual material strength degradation. During fire exposure, the applied stress may cause large plastic deformation, grain elongation, dislocation agglomeration, precipitate cracking, and cavity formation associated with the increase of strain; collectively, these are the stress-induced damage [6-8]. Premature failure may occur with the accumulation of the stress-induced damage. In situations where the fire is extinguished and yet the load-bearing structure remains intact, a key concern is the future performance of the structure. In order to predict the post-fire performance of load-bearing aluminum structure, a detailed understanding of the stress-induced damage that has developed is necessary.

Hence, this research will focus on developing a fundamental understanding of microstructure-mechanical property of post-fire aluminum alloys Al5083-H116 and Al6061-T651. The purpose is to identify the stress-induced damage in aluminum alloys in addition to that caused solely by the elevated temperature exposure. Both unstressed thermal exposure and mechanically strained microstructures are studied to separate the stress-induced microstructural damage, which is manifested as cavitation, dynamic recrystallization, and dynamic precipitation. The connection between the imposed stress and the resulting response of the grains, cavities, dislocations, precipitate evolution and the post-fire material strength degradation will also be established.

1.2 Literature Review

This literature review summarizes the previous work related to the high temperature performance and the thermo-mechanical properties of aluminum. As discussed above, aluminum alloys have been widely applied in industry and engineering fields for more than one hundred years. Research has been done in many aspects of the aluminum response at elevated temperature exposure, including microstructure evolution with temperature, elevated temperature

performance, post-fire thermally-induced damage, creep damage characterization and creep models. Both testing and modeling have been performed to analyze the degradation of material properties after high temperature exposure.

1.2.1 Material Response Due to Thermal Exposure

Research has been done in evaluating the performance of aluminum alloys during elevated temperature exposure. Thermo-mechanical tests have been applied to investigate the mechanical properties of aluminum alloy 5083-H116 and 6061-T651 at elevated temperature. The commonly used heating methods for elevated temperature research are the ohmic heating and induction heating. Ohmic heating has been used to perform the ultra-high temperature mechanical tests for metal alloys up to 3000°C [9]. Another heating approach, induction heating, can provide variable heating rates and admits accurate control of the test temperature. As a result, induction heating systems are used in most steel and aluminum heating tests [10].

Aluminum alloys exhibit significant strength degradation during elevated temperature exposure. Normalized high temperature modulus, yield, and ultimate strength of aluminum alloys have been summarized by Eurocode 9 and the American Society of Metals Handbook [11, 12]. Similar tensile tests are also performed at Virginia Tech to verify the elevated temperature properties of aluminum alloys [4]. It has been reported that Al5083 exhibits ductile shear failure below 400°C and breaks at weak microstructural locations without any particular failure mode at temperatures higher than 400°C, while Al6061 shows more ductile fracture with increasing temperature [4]. The yield and ultimate strengths decline simultaneously, but the rates of decrease exhibit distinct regions of behavior. The material strength remains relatively constant between room temperature and 150°C, dramatically decreases from 150°C to 300°C. In the final region between 300°C and 500°C, material microstructure has been significantly changed and the strength decreases linearly with temperature. These mechanical properties at elevated temperature have been modeled and validated by Maljaars et al. [13, 14]. Maljaars et al performed tensile tests to several frequently used aluminum alloys (5xxx and 6xxx series) and validated the 0.2% yield stress models in Norwegian standard NS 3478 [15] and European standard EN 1999-1-2 in comparison with data at multiple elevated temperatures [11].

However, these studies only provide the information for aluminum strength degradation maintained at elevated temperature and evaluate their performance during fire exposure. The permanent microstructural change and the corresponding degradation in the material's residual properties after fire exposure and return to the ambient temperature have not been examined yet.

For those aluminum structures which have been subjected to fire but have not experienced mechanical failure, internal fire damage has been accumulated to affect the materials' performance after returning to the ambient temperature. A major concern is the mechanical performance of materials after fire exposure, i.e., the residual (post-fire) mechanical behavior of thermo-mechanically damaged aluminum. This aspect is important for evaluation of structural stability of aluminum structures after a fire.

Matulich, et al. [16] quantified the post-fire mechanical properties of Al5083 and Al6082 by heating the material from room temperature to particular temperatures up to 500°C and then cooling down to ambient temperature. Room temperature tensile tests and hardness measurements were performed on post-heated samples. Post-fire strength of Al5083 exhibit regional decline with pre-test exposure temperature: post-fire yield strength declines initially from about 150°C - 280°C, then decrease more severely from about 280°C - 380°C. More than a 50% reduction in Al5083's yield strength was measured after prior exposure to 380°C. For exposure temperature above 380°C, almost no further strength reduction was observed up to 500°C. The post-fire strength of Al6082 remains stable from room temperature to pre-test exposure temperature of 250°C, decreases from 250°C to reach the lowest residual strength at 400°C, after that the residual strength recovers somewhat for exposures up to 500°C. The relationship between hardness and mechanical properties was also examined. Empirically, it was found that a linear correlation exists between Vickers hardness and the post-fire material strength. Serrated yielding (the PLC effect) caused by the solute-dislocation interaction during grain boundary slipping was observed in Al5083 post-fire stress-strain curves; the magnitude of the serrations decreases with increasing pre-test exposure temperature was also discussed by W. Wen [17]. Magnesium atoms in solid solution are found to be the main factor associated with the intensity of serrated yielding. At higher temperature treatments, when Mg is precipitated out of solid solution, the PLC effect decreases. In contrast, the heat-treatable Al6082 only displays the serrated yielding at thermal treatment temperature of 500°C.

These past research efforts have summarized the mechanical properties of aluminum alloys during and after elevated temperature exposure. The post-fire performance of thermally affected aluminum alloys can be evaluated based on the thermal-mechanical test data. However, the changes in mechanical properties are caused by the internal microstructural damage due to thermal exposure. Thus, an understanding of how the internal damage mechanisms cause materials' strength degradation during heat treatment is necessary for future evaluation of the structural stability after fire and assessment of replacement needs of the damaged structural elements.

1.2.2 Thermally-Induced Microstructural Damage

The internal fire damage generated in the stress-free structures is solely caused by thermal exposure during fire, and is termed thermally-induced damage. Microstructure characterization of aluminum alloys has been performed to examine the evolution of grains, precipitation and dislocation due to elevated temperature exposure. Optical microscopy, scanning electrical microscopy (SEM), transmission electrical microscopy (TEM) and electron backscatter diffraction (EBSD), 3D X-Ray tomography are the techniques frequently used in examining materials' microstructure.

Aluminum alloys are strengthened from different methods, including strain strengthening, precipitate strengthening, etc. Previous studies indicate that the strength and ductility of aluminum alloys are obtained through the development of complex microstructures. May et al. [18] studied the dislocation density and grain structure in Al-Mg alloys and found the relationship between mechanical properties and the alloying elements. After severe plastic deformation, the resulting grain size is smaller and the dislocation density is higher with increasing amount of alloying elements; thus higher hardness and strength are achieved. Huskins et al. [19] also explored the various strengthening mechanisms in Al-Mg alloy. A basic strength model including dislocation strengthening, solute strengthening, precipitate hardening, grain boundary strengthening, strain and strain rate hardening was proposed. For the as-received aluminum alloy, pre-existing dislocations distribute in the grains due to the plastic deformation during the manufacturing process. The microstructures are refined by these curved dislocations and divided into sub-domain structures. The primary alloying elements, Mg and Mn, remain in solid solution to form the solute atoms. The interactions between stationary solute atoms and the

mobile dislocations result in the strengthening of the material. Mg in solid solution provides the major contribution to the solute strengthening for Al-Mg alloy. Other elements dissolve in the material matrix to form the complex precipitates. Both precipitates and grain boundaries act as obstacles to dislocation motion and contribute to strengthening of the material.

When aluminum alloys are subjected to fire, the heat treatment will cause relief of the residual stresses resulting from the manufacturing process. The stored energy will be reduced in the deformed grains by the removal or rearrangement the dislocations, termed as recovery. Subgrain structures divided by the dislocations also coarsen during the dislocation recovery. Strength reduction and the ductility increase are normally associated with the dislocation recovery. When the annealing temperature is high enough, grain recrystallization is also driven by the release of stored energy from material processing during thermal exposure. New grains will nucleate and grow until the original deformed grains are completely replaced. More reduction in the material strength and hardness is accompanied with grain recrystallization.

During thermal exposure, the precipitation sequence evolution is another important feature in Al-Mg-Si alloys. The formation and evolution of precipitates have been investigated in numerous studies using differential scanning calorimetry (DSC) and transmission electron microscopy (TEM) [20, 21]. The generally accepted precipitation sequence for Al-Mg-Si alloys during high temperature exposure is SSSS (supersaturated solid solution) → clusters/Guinier-Preston zones → β″ → β′ → β (Mg_2Si). The detailed precipitation evolution is dependent on heating rate; the peak temperature of β″, β′, and β-phase precipitation increases with the increase of the heating rate. For a heating rate of 20°C/min, the strengthening phase evolution with temperature based on DSC measurement is: the β″ dissolution peaks at ~260°C; the β′ precipitation peaks at ~310°C, then following the dissolution peak between 350°C and 420°C; the β precipitation peak is identified at ~460°C, and the dissolution peak at ~510°C [22]. Associated with the evolution from metastable β″ phase to stable equilibrium phase β, the interactions between precipitates and dislocations are weakened to cause material strength degradation.

As discussed above, thermally-induced damage can be represented as the permeant change in microstructure during thermal exposure, including dislocation recovery, recrystallization, and precipitation evolution. The post-fire material strength will be degraded as result of the microstructural damage during fire exposure. Summers et al. [5] studied the thermally-induced

damage and corresponding post-fire behavior of Al5083 and Al6061 after thermal exposure without applied stress. The material strength evolves from lightly affected to severely degraded with increasing thermal exposure temperature. The post-fire yield strength of Al5083 exhibits an initial decline from about 150°C - 280°C, then experiences a more severe decline from about 280°C - 380°C. More than a 50% reduction in yield strength was measured after prior exposure to 380°C. For further heating, almost no further strength reduction was observed from 380°C up to 500°C. Static dislocation recovery and static grain recrystallization are the primary causes of Al5083 strength degradation during stress-free thermal exposure. The initial strength reduction below 280°C is primarily caused by the subgrain coarsening during dislocation recovery; the primary strength reduction between 280°C to 380°C due to static grain recrystallization, which annihilates the subgrain structure. The kinetics of grain recrystallization studied also explains the post-fire behavior dependence on the heating rate in the absence of stress. In contrast, the post-fire yield strength Al6061 experiences a relatively steady reduction from 200°C - 450°C. After exposure to 500°C, an increase in yield strength is observed. The residual yield strength degradation is caused by the precipitation growth during heat treatment. The initiation of yield strength degradation causes by the precipitate growth from the metastable β″ to β′ phase from approximately 250 - 300°C. Significant reduction in residual yield strength after exposure to 400°C is due to the following the β′ precipitate dissolution and equilibrium β phase formation. When large β precipitates govern the strengthening phase, residual yield strength drop to the minimum value, which has great dependence on the heating rate. Increase of the heating rate will causes increases of the peak temperature of β″, β′, and β-phase precipitation, and results in different response in post-fire response.

These previous works provide comprehensive knowledge for the microstructure evolution and corresponding post-fire behavior of the heat affected aluminum alloys. However, they only focus on the solely thermally-induced damage and do not account for the stress effects on microstructural damage and post-fire response in the load-bearing aluminum structures. For most structural applications, aluminum is designed to carry mechanical loads during working period. Hence, information regarding the combined thermal exposure and mechanical loading effect on post-fire material properties is necessary for the structure stability evaluation.

1.2.3 Stress-Induced Microstructural Damage

In addition to the stress-free thermally-induced fire damage, stress also plays an important role in the development of thermo-mechanical damage in aluminum alloys. The time-temperature-stress material dependence, i.e., creep, is of major significance when considering material performance in fire. Grain elongation, dislocation agglomeration, precipitate cracking, and cavity formation occurring with the increase of creep strain are collectively referred to the stress-induced damage [6-8]. Premature failure may occur in aluminum structures due to the accumulation of stress-induced damage. The incipient causes of creep failure include cavity nucleation, growth, and the subsequent coalescence of cavities within certain proximity.

Creep cavitation in metals has been studied for several decades. Kassner et al. [23] summarized the important developments relating to both the nucleation and growth of cavities in metals. Creep cavity formation occurs during the primary and secondary creep stages; the following growth and coalescence of these cavities in tertiary creep stage can directly lead to the eventual failure of the material.

Cavities are observed to frequently nucleate on the grain boundaries, particularly on those transverse to the tensile axis or associate with second phase particles. This process is known to be affected by the external thermo-mechanical loading condition. However, consensus on the mechanism of cavity nucleation does not yet exist. Greenwood [24] proposed an early idea of vacancy agglomeration from the stable voids (nuclei). The cavity nucleation by vacancy accumulation requires a significant stress concentration with local stresses orders of magnitude greatly larger than applied stress leading to fracture [25]. Stress concentrations can be caused by grain boundary sliding at triple junction and precipitates on the grain boundaries. Sufficient local stresses on grain boundaries will promote the formation of cavities on grain boundaries [26]. With the observation that gain boundaries transverse to the principal tensile axis are more likely to cavitate, the grain boundary sliding mechanism was challenged to be an unnecessary condition for cavity nucleation [27]. However, subsequent research on the straining the copper bicrystals in an orientation favoring grain boundary sliding demonstrated the ability of grain boundary sliding to nucleate cavities [28, 29]. Moreover, cavitation on transverse grain boundaries can also be accelerated by the stress concentration generated by grain boundary sliding on those locations. Along with the relationship between grain boundary sliding and creep strain is revealed, the role

of grain boundary sliding in cavity nucleation and growth is unclear [30]. Dislocation pile-up is another factor which may cause stress concentration at the grain boundaries, particularly when dislocation pile-ups against the precipitates on the boundaries. Dislocation pile-up against precipitates may also occur inside the gains and promote the cavity nucleation, but these interior cavities are not as numerous as those nucleated at boundaries and grow more slowly [31, 32]. Thus cavity nucleation commonly occurs at grain boundaries and around precipitates, where the stress concentration is most likely to be generated during the continuous plastic deformation. The existing cavities may also result in stress concentrations and lead to new cavity formation as the damage progresses, with a probability in the stress peak which is predicted to increase as the cube of the distance from the existing cavity [33].

Vacancy diffusion has long been proposed to be the mechanism which promotes creep cavity growth. Under the external applied stress, cavities nucleated at grain boundaries can migrate along the boundaries, a process which is controlled by diffusion. By establishing the stress concentration ahead the cavities, diffusion-controlled cavity growth models have been derived [34, 35]. Relationships between cavity growth rate and stress as well as rupture time and stress have been developed based on the grain-boundary diffusion cavity growth model. The creep rupture time is found to reduce with increasing applied stress, while the rate of cavity growth varies linearly with the applied stress [36, 37]. Except for grain-boundary diffusion, surface controlled diffusion has also been proposed to control the cavity growth [38]. The cavity growth rate in terms of applied stress was determined by a coupled analysis of diffusion and stress concentration ahead of the cavity.

Grain boundary sliding has been considered as another mechanism which is important for cavity growth. During the continuous plastic deformation under thermo-stress condition, cavities are observed to grow in the plane of the sliding boundary [39]. However, surface diffusion may limit the tip velocity of the cavity growth during the grain boundary sliding. The diffusive cavity growth rates are predicted to be larger than the sliding growth rates [40].

Creep cavities are in-homogeneously distributed. The difference in geometry and orientation of grain boundaries towards applied stress also provide them different tendencies to nucleate cavities. Thus the cavity growth in the areas affected by the circumjacent cavitation may be constrained by the uncavitated areas. The constrained cavity growth rate model was first

proposed by Dyson [41], then following by Riedel [40], in which the constrained cavity growth predicts much lower growth rates and longer time to failure than the unconstrained cavity growth. Dyson [41] has demonstrated that the rate of unconstrained cavity growth is directly proportional to the maximum principal tensile stress, whereas constrained growth is proportional to some positive power of the octahedral shear stress.

Creep plasticity also plays an important role in creep cavity growth. Creep deformation of the material surrounding the grain boundary cavities will produce strains at the surface of the cavities and drive them to grow larger. A creep controlled cavity growth model without vacancy flux has been proposed by Hancock et al. [42]. The comparison between diffusive cavity growth and plastic cavity growth demonstrated that cavity grows faster when driven by plasticity. Particularly under high strain-rate conditions, the creep plasticity becomes important in the cavity growth within the region where the strain is high.

The diffusive cavity growth and creep plasticity effects on surrounding material can be coupled. The diffusion length has been defined to describe the interaction of grain boundary diffusion with the surrounding creep field. The cavity grows by diffusion within the diffusion distance from the cavity, while growth is controlled by creep plasticity outside the diffusion distance. Creep plasticity may also enhance the diffusive cavity growth by reducing the diffusion distance, particularly under high applied stress and strain rates conditions [43]. Cocks et al. [44] verified that cavity growth is controlled by diffusion when cavities are small, then controlled by power-law creep when they are large. Cavities may grow initially by diffusion, then by coupling of diffusion and power-law creep, and finally by creep plasticity alone. Thus the time to fracture is determined by both mechanisms. However, the cavity growth rate due to coupling is faster than the growth rate calculated by simply adding the diffusive growth rate and creep growth rate.

The final stage of the material life is creep crack growth, which is quite relevant to the cavity nucleation and growth. As cavities grow by diffusion controlled or plasticity induced deformation, the coalescence of cavities with each other will lead to crack formation. Nix et al. [45] developed a creep rupture model base on the plastic growth of cavities at the tips of grain boundary wedge cracks. A steady-state crack growth rate has been shown to be a result of plastic growth of cavities ahead of the crack tips. Cracks can also expand by linking up the diffusive

growing cavities. Riedel [40] suggested that the plasticity controlled cavity growth models correlates better with the crack growth data than the diffusive growth models.

In addition to cavitation, dynamic recovery, dynamic recrystallization and dynamic precipitation were also investigated as other types of thermo-mechanical damage for aluminum alloys [46-49]. Dynamic recovery is a softening effect which reduces the dislocation multiplication during the plastic deformation. The principal difference between dynamic recovery and static recovery is that stored energy continues to be introduced even as it is decreased by the dynamic recovery process. Dislocation density is reduced through the cross-slip of screw dislocations and the climb of edge dislocations. These processes have strong dependence on the elevated deformation temperature [49]. In previous research, the dislocation tangles were observed to disappear when aluminum was deformed at 100°C and 200°C. After deformation at 250°C, the dislocation tangles are nearly gone [48]. Although the mechanisms are similar between dynamic recovery and static recovery, the dynamic recovery proceeds at a rate controlled by the applied stress or strain rate, while static recovery proceeds at a declining rate which is affected by the internal stresses to cause heterogeneity [50].

Dynamic recrystallization process is contrasted to static recrystallization in that new grains nucleate and growth of the grains occurs during the plastic deformation. Dynamic recrystallization occurs in various forms, including geometric dynamic recrystallization, subgrain rotation recrystallization, and discontinuous dynamic recrystallization. The mechanism of geometric dynamic recrystallization initiates when grains are increasingly flattened until the boundaries on each side are separated by only a small distance; the serrated edges of the grain boundaries will come into contact to form new grains [51]. Subgrain rotation recrystallization is represented as the initially low-angle sub-grain boundaries rotation; the rotation will cause the crystal lattices across the boundary mismatch to be regarded as grain boundaries [52]. Discontinuous dynamic recrystallization usually occurs during the transition of softening mechanism from strain-hardening and dynamic recovery to dynamic recrystallization. When strain hardening and dynamic recovery cannot store more immobile dislocations, discontinuous dynamic recrystallization begins. Discontinuous dynamic recrystallization takes place in low stacking fault energy metals, such as magnesium alloys and beta titanium alloys. Aluminum alloys are high stacking fault energy metals and, as a result, undergo continuous dynamic

recrystallization during the high temperature deformation [53]. Numerous studies have been developed in dynamic recrystallization: Agarwal et al. [46] studied the effect of strain rate and particle size on dynamic recrystallization of Al5083 at high temperature exposure. Vatne et al. [54] developed a physically-based model to predict recrystallization kinetics, recrystallized grain sizes, and recrystallization textures during multipass hot rolling of aluminum.

Grain size, shape, and texture have been found to evolve during the continuous creep deformation of aluminum alloys. Strengthening mechanisms based on grain structure change have been studied: the Hall-Petch relation established an effective method to estimate material strength caused by average grain size change [55]. The effect of grain shape change on the material strength has also been studied [56]. Grain aspect ratio evolution has been proposed to cause the material yield strength change. Yield strength will increase as structure evolves from an equiaxed grain structure to high aspect ratio grains. A model coupling grain orientation and grain size/shape effect has been developed [57]. Flow stress strengthening with the increase of hot deformation strain for other materials was discussed [58]. Based on various strengthening mechanisms in Al-Mg alloys including grain boundary strengthening, solute strengthening, precipitate hardening, dislocation wall strengthening, dislocation sub-structure was found to be the dominant strengthening mechanism in Al5083 [19]. Grains will be highly elongated with the increase of creep strain during the dynamic recrystallization process. The grain structure strengthening effects can be referenced to the subgrain structure strengthening mechanism. Saturated dislocations have been generated in the as-received Al5083 during the strain hardening process. An increase in grain aspect ratio in the dynamic recrystallization process will cause refinement of the dislocation sub-structures. Smaller subdomains will be developed and result in strengthening in the residual material strength [19].

Dynamic precipitation is another pronounced phenomenon during the thermo-mechanical process for the age-hardening alloys, such as Al-Mg-Si Alloys. The strengthening effect of dynamic precipitation during plastic deformation for aluminum alloys of has been investigated extensively. Roven et al. [59] studied the precipitation behavior of Al-Mg-Si alloy during severe plastic deformation and discussed the interaction between precipitates and dislocations. Cabibbo et al. [60] also studied the strengthening mechanism of the second-phase particles during severe plastic deformation for 6082 Al-Mg-Si alloy. The second-phase Si particles were found to

dissolve progressively and become less effective with increasing deformation. Other second-phase Mg_2Si particles were cut and fragmented by the dislocations, and, as a result, only have limited contribution to material strength. Fine Mg_2Si precipitates were found distributed in hot deformed AA 6015 alloy at low temperatures; for higher heating temperature above 400°C, the Mg_2Si precipitates coarsen with temperature. The effect of Mg_2Si precipitate size on dynamic restoration was analyzed [61]. Dynamic precipitation of Mg_2Si during hot extrusion and its impact on the microstructures and mechanical properties of Al-Mg-Si-V alloys were also investigated [62]. Dynamic precipitation of coarse Mg_2Si particles was found to result in considerable coarsening of recrystallized grains due to reduce the solute drag on the grain boundary motion, consequently result in the considerable decrease in material strength experience. Dynamic precipitation and dynamic recrystallization in 6061 aluminum alloys during compressive hot deformation was studied by Fan et al. [47]. Strain rate sensitivity and the effect of temperature on dynamic precipitation and recrystallization are discussed. Dynamic precipitation has strong dependence on temperature with more precipitates appearing at 400°C but none at 500°C. Geometry dynamic recrystallization takes place concurrently and has stronger grain refinement effect at high temperature than at low temperature.

Previous researchers have summarized the stress-induced microstructure damage for aluminum alloys, including cavitation development, dynamic recovery, dynamic recrystallization and dynamic precipitation. However, the influence of stress-induced microstructural damage on the residual (post-fire) mechanical properties has been fully investigated yet. The combined effects caused by different stress-induced microstructure damages on residual material strength have not been fully understood yet.

1.2.4 Thermo-Mechanical Damage Models

Based on the above fundamental studies, thermo-mechanical damage models have been developed to provide engineering design criteria and fracture life prediction for the structures working under high temperature environment. Yao et al. [63] reviewed the existing theories and creep design approaches including the models based on classical plasticity theory (CPT), the cavity growth mechanism (CGM) and the continuum damage mechanics (CDM), in which the constitutive equations and design criteria are presented for each approach.

By assuming the similarity in multi-axial creep behavior and classical plasticity, the classical plasticity theory (CPT) has been initially used in creep behavior analysis. A uniaxial creep constitutive relationship has been derived based on the tensile data under constant load and high temperature. The Norton-Bailey law has been established to describe the primary, secondary, or tertiary creep strain in term of stress and time under isothermal conditions. The primary creep strain rate is also derived based on time hardening or strain hardening effect [64]. For multi-axial stress states, creep is found to be a shear-dominated process. The concept of effective stress is used to describe the creep strain based on the uniaxial creep analysis. However, creep models derived from the classical plastic theory are limited to the yielding failure criteria. Cavity nucleation, growth, and coalescence-the primary factors causing the creep failure-are not accounted for.

Models based on the cavity growth mechanism (CGM) consider the creep damage caused by cavity nucleation and growth process, including three categories: diffusion-controlled cavity growth, plasticity-controlled cavity growth, and constrained cavity growth. The diffusion-controlled cavity growth model was first proposed by Hull and Rimmer [34]. In this model, the influence of cavity shape and diffusion process on cavity growth rate is analyzed. The chemical potential gradient of vacancies in the plane of grain boundaries is defined to determine the cavity growth rate, and then creep rupture time is obtained from the integration of cavity growth rate. As discussed in previously, the cavity growth will switch from diffusion-controlled to plasticity-controlled with the enlargement of cavity size. In the plasticity-controlled growth model, plastic deformation of surrounding materials is considered as the mechanism that promotes cavity growth. The cylinder cavity model in the plastic material was initially proposed by McClintock [65] to study the effect of imposed stress and strain on cavity growth. Following that, Rice [66] proposed a spherical cavity model in a remote-uniformed stress and strain rate field to investigate the relation between stress triaxiality and void growth. The relationship between multi-axial failure strain and uniaxial failure strain can be also obtained from the ratio of average cavity radius strain rate to the remote-imposed strain rate. When local strain rate exceeds surrounding strain rate, the cavity growth is constrained. The constrained cavity growth model was first proposed by Dyson [41], then further developed by Edward and Ashby [67] who suggested that cavity growth followed the power law rule. After they derived the equations for cavity growth

and creep strain rate, they expressed the time to fracture in terms of the steady creep rate without cavities and the cavity area fraction.

Continuum damage mechanics (CDM) models work by introducing the damage variables based on the equivalence principle and a representative volume element to eliminate the micro defects inside the material. The stress and strain states can be considered homogeneous in this approach. The CDM model for creep rupture was first proposed by Kachanov [68] by defining a damage variable ω to represent the cavity volume fraction during the creep process. He assumed ω was zero in the as-received state and then increased to approach unity at fracture. After that, Robotnov [69] introduced the concept of effective stress at a given damage state; based on that the equivalent strain can be coupled with damage and constitutive laws can also be derived [70]. This model assumes isotropic damage and adopts the scalar damage variable, can be easily applied in engineering applications. In the uniaxial tensile loading condition, a constitutive model was proposed by Kachanov to simulate the tertiary creep region and predict the rupture time and strain. For multi-axial creep, single variable models which consider only one damage mechanism in creep fracture were developed from classical Kachanov–Robotnov equation in uniaxial condition or the irreversible thermodynamics [70]. However, multi variable models show more advantages by considering different mechanisms in the damage evolution [71].

1.3 Research Objective

In previous research, elevated temperature and post-fire mechanical properties of Al5083 and Al6061 have been studied. Material strengths were found to degrade due to high temperature exposure. Microstructure evolution has also been characterized to investigate the linkage between internal thermally microstructural damage and residual (post-fire) material strength. Basic material strength models including different strengthening mechanisms have also been established. However, these researchers primarily focused on the solely thermally-induced damage and did not account for the stress effect on microstructural damage and the post-fire response in the load-bearing aluminum structures. A lack of understanding still exists on the effect of stress-induced damage on the residual material strength for the aluminum alloy after fire exposure.

The purpose of this research is to develop an understanding of the impact of stress, temperature, and time on fire damage development in aluminum alloys. Stress-induced damage is emphasized and separated from the thermally-induced damage in both microstructure and residual mechanical properties. Fundamental damage quantifications are established to analyze the simultaneously evolving mechanisms in damaged microstructure. The post-fire response after thermo-mechanical damage is investigated with reference to the damaged microstructure present in the material. Different behavior in the creep mechanisms between Al5083 and Al6061 are discussed.

Preliminary effort is made to study the effects of different heat treatment methods on the residual material strength degradation of aluminum alloys, including aging time, heating and cooling rate. Heating rate dependences at critical exposure temperature (400°C) are analyzed for both Al5083 and Al6061.

In the stress-induced damage study, a uniaxial stress state and selected temperatures are adopted to simulate the fire-load creep condition for aluminum alloys. Damage associated with the creep response is examined by two-dimensional scanning electron microscopy, high resolution optical microscopy, and three-dimensional X-ray micro-tomography. Both unstressed and mechanically strained states are examined to separate the stress-induced damage. The cavitation and dynamic grain structure evolution in aluminum alloy during creep are analyzed to study the stress-induced damage mechanism for both Al5083 and Al6061. The differences in microstructure evolution caused by imposed stress between strain-hardening Al5083 and precipitate-hardening Al6061 are discussed. Different stress influence on grain growth and cavity development, interaction between dynamic recrystallization and dynamic precipitation are identified.

To link the microstructural details to residual mechanical properties, residual mechanical properties are also determined from the room temperature quasi-static tensile tests after creep. Materials' post-fire performances are evaluated and their dependence on the stress state during prior elevated temperature exposure is analyzed. Residual material strengths calculated based on deformed cross sectional area are analyzed to ascertain the impact of stress-induced microstructural damage on the post-fire material response. The competing mechanisms of cavitation and grain structure evolution are discussed. Engineering residual material strengths

calculated based on original cross sectional area are also studied to provide some information useful for structural design.

CHAPTER 2 - Heating Method Effects on Residual Mechanical Properties

2.1 Introduction

Aluminum alloys are important for lightweight structural applications such as in automobiles, aerospace, and ship engineering. The properties of aluminum alloys including high strength, low density, good weldability, and excellent resistance to seawater and corrosive chemicals distinguish them from conventional structural materials and have increased their construction application.

A major concern with the application of aluminum is the safety during extreme fire conditions. While an aluminum structure is subjected to fire, the mechanical properties of the material may be degraded and premature failure may occur with the accumulation of fire damage. Thus particular consideration must be given to the structural stability during fire exposure. Mechanical properties at elevated temperature have been summarized to provide design standards for aluminum alloys [11, 12]. The property degradation for aluminum alloys initiates at temperatures as low as 150°C; more than 50% strength reduction occurs after 380°C exposure [16]. Thus in situations where the fire is extinguished and the structure remains intact, it is necessary to evaluate the future performance of the structure.

Fire exposure may have large variability as a result of distances from the fire, structural insulation, and the fire extinguishing method(s) employed. These factors may lead to different impacts on the post-fire performance of aluminum structures. Moreover, the time after fire exposure may cause aging to affect the post-fire residual strength of the aluminum structure. In order to make an accurate estimation of the post-fire performance of an aluminum structure, a detailed understanding of the thermal exposure damage caused by different heating methods and aging time is necessary.

2.2 Experimental

2.2.1 Materials and Sample Geometry

Marine-grade aluminum alloy Al5083-H116 and Al6061-T651 were included in this study. Aluminum 5083 is a work-hardened alloy that contains 4 - 4.9% of magnesium as its major alloying element. It is a weldable, moderate strength alloy which exhibits excellent corrosion resistance in the H116 condition. Aluminum 6061-T651 is a precipitation hardened aluminum alloy; the major alloying elements are 0.8 – 1.2% of magnesium and 0.4 – 0.8% of silicon. It exhibits high strength, good welding ability and also has good corrosion resistance to sea water and chemicals. Both alloys are frequently used in ship construction. Both materials were supplied by Alcoa in form of 6.35mm inch thick sheets. The nominal chemical compositions for both alloys are shown in Table 1.

Table 1 Chemical composition of Al5083 & Al6061 material (wt.%)

Chemical element	Al	Mg	Mn	Si	Fe	Zn	Ti	Cr	Cu
Al5083	Balance	4.0-4.9	0.4-1.0	0.4	0.4	0.25	0.1	0.05-0.25	0.1
Al6061	Balance	0.8-1.2	~0.15	0.4-0.8	~0.7	0.25	0.15	0.04-0.35	0.15-0.4

The test sample geometry, illustrated in Fig. 1, was selected based on the ASTM standard E21-09. Specimens were machined from the 6.35mm thick as-received plate to dog-bone geometry, as shown in Fig. 1. The overall length of test samples was 178mm with the longitudinal axis of the specimen aligned with the material rolling direction. The sample gage length is 76.2mm with uniform width of 12.7mm. All test samples of each alloy were machined from the same aluminum sheet to keep uniform material properties.

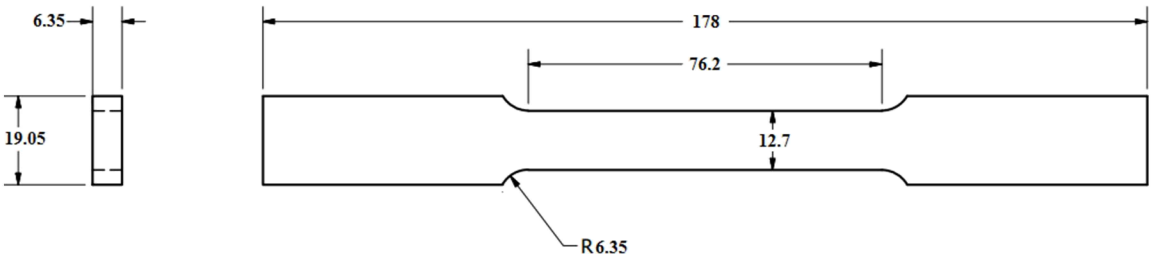

Fig. 1 Tensile test specimen geometry (mm)

2.2.2 Heating Methods

Specimens were heated from room temperature to pre-selected temperatures (200°C, 300°C, 400°C and 500°C) to simulate fire exposure. Once the target temperature was reached, samples were cooled down immediately to room temperature. Uniaxial tensile tests were then conducted to study the post-fire tensile behavior and residual work hardening rate at various temperatures. Previous work revealed that 400°C was a critical temperature at which grain recrystallization was completed in Al5083 and equilibrium β phase precipitate formation in Al6061; the lowest post-fire yield and ultimate strengths occurred after 400°C exposure [5, 16]. Thus 400°C was selected to study the effect of different heat treatment methods and aging times on residual mechanical properties for Al5083 and Al6061.

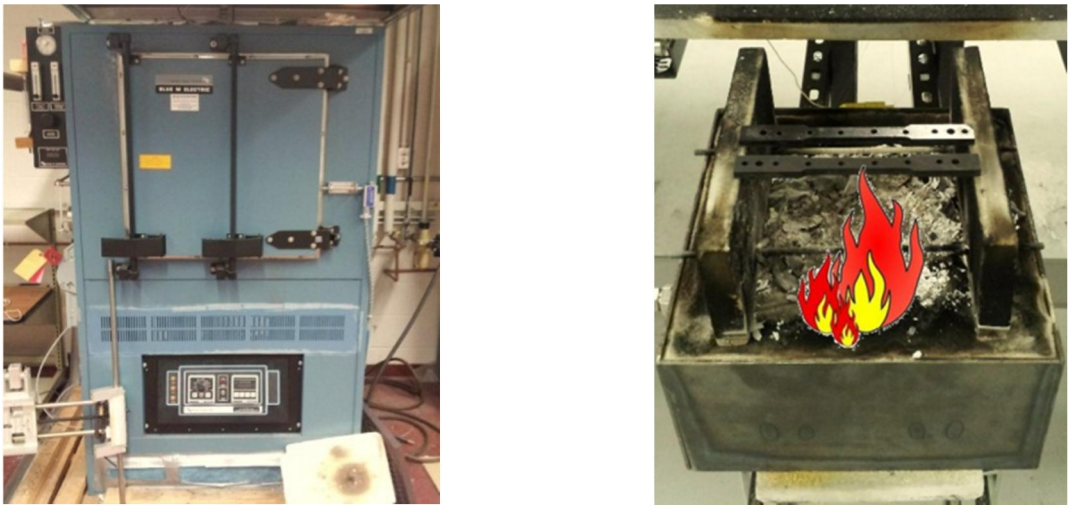

(a) (b)

Fig. 2. Heating equipment (a) Blue M Furnace (b) Sand Burner

In the 400°C exposure test, specimen heating was conducted by two methods: furnace heating and fire exposure. Furnace heating was performed in a Blue M Furnace, as shown in Fig. 2a. The furnace temperature was controlled by a PID controller, and the specimen temperature was measured by a dummy sample with a thermocouple attached to the center. Specimens were heated in the furnace from room temperature to 400°C at an approximate heating rate of 30°C/min. Fire exposure tests were conducted using a sand burner, in which the fuel for the fire was supplied by propane gas. An IR camera was placed about 1 meter above the specimens to measure the center temperature of the specimens during the heat exposure. The approximate heating rate for samples heated by the sand burner with a $10m^3$/min gas flow rate is 80°C/min.

After reaching 400°C, the specimens were immediately removed from the heat source and cooled down to ambient temperature in one of two ways (either air cooling or water quenching). They were then aged at room temperature for 1, 3, 10 and 30 days, after which Vickers hardness tests and post-fire uniaxial tensile tests were conducted to measure the residual material properties at room temperature.

2.2.3 Hardness and Post-Fire Tensile Tests

The Vickers hardness tests were performed at room temperature prior to the tensile test, by using HVA-10A Vickers hardness tester with an applied load of 5kgf. Six diamond pyramid indentations were made by the Vickers hardness tester within the grip region of the specimen, after which the diagonal lengths of each indentation were measured and averaged to calculate the post-fire hardness of the material. The average diagonal length of the indentations was used to calculate the hardness.

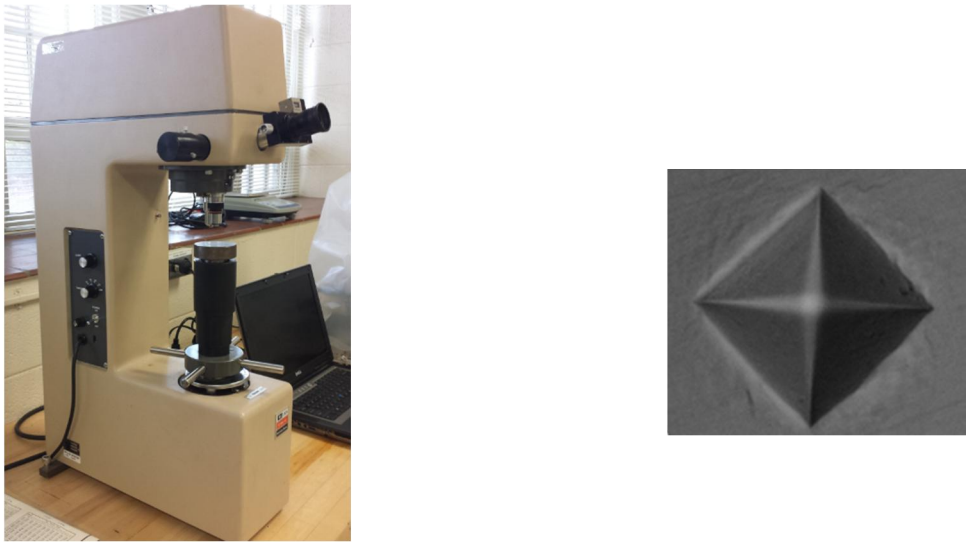

(a) (b)

Fig. 3 (a) Leco V-100-A2 Hardness Tester (b) Diamond pyramid indentation

All the post-fire uniaxial tensile tests were conducted after heated samples returned to ambient temperature. An MTS 880 Test Frame equipped with a 10 kN load cell was used for conducting the post-fire tensile tests. A MTS 458.91 Micro-Profiler was used to program the test procedure and control the experiment process. Hydraulic grips were used to provide constant grip force to both ends of the dog bone sample. All the tensile tests were conducted at room temperature. A

tensile load was applied until failure. Tests were performed using displacement control at a rate of 5 mm/min. Sample strain was measured using a MTS 634.11E-54 type extensometer with 1 inch gage length and 50% calibration extension. A Vishay 2310 Signal Conditioning Amplifier is used for convert the voltage in the extensometer to strain signal. Data acquisition was performed through LabView program to record the real time load, stroke, strain and time data during the tensile tests.

(a) (b)

Fig. 4 (a) MTS 880 Load Frame (b) MTS Micro Profiler

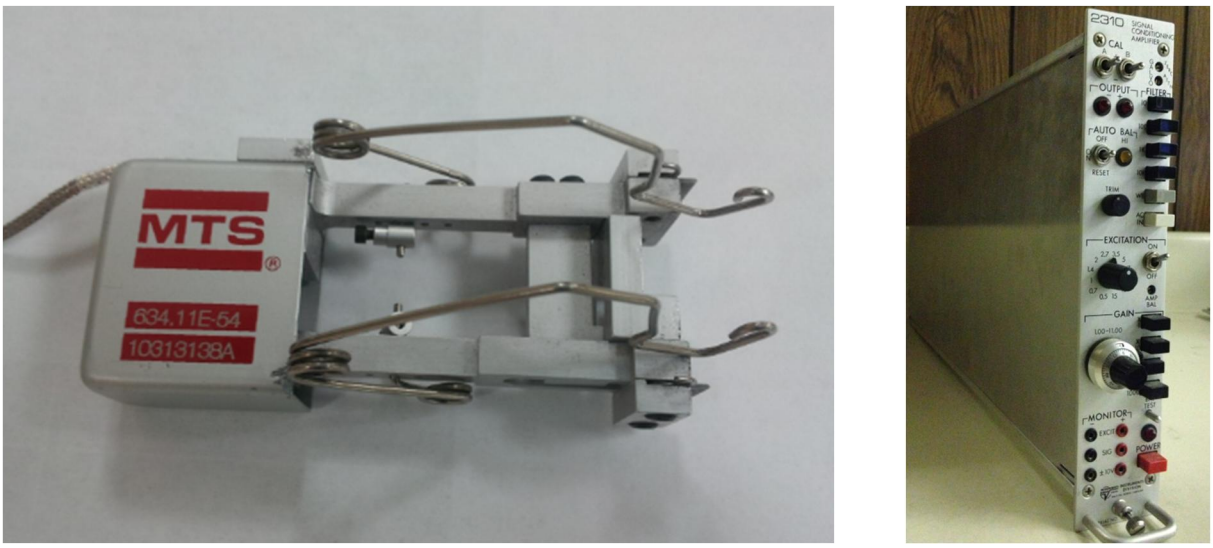

(a) (b)

Fig. 5. (a)MTS 634.11E-54 extensometer (b) Vishay 2310 Signal Conditioning Amplifier

2.3 Post-Fire Tensile Behavior

Post-fire stress-strain relations at different exposure temperatures for both alloys are summarized in Fig. 6. For comparison, the as-received stress-strain curves for specimens that have not been heat treated are also plotted. There are some oscillations shown in the plastic region of the Al5083-H116 stress-strain curves, which is attributed to the interaction of dislocations with solute atoms; the behavior is called Portevin–Le Chatelier (PLC) effect. This phenomenon is also known as dynamic strain aging (DSA). The DSA causes spatially inhomogeneous plastic flow over a range of applied strain. When the exposure temperature increases, the oscillations in the plastic region are decreased. For Al6061-T651, only the tensile behavior for samples previously exposed to high temperatures (400°C and 500°C) exhibits similar dynamic strain aging. This behavior is due to the large β precipitate formation in Al6061 for thermal exposure above 400°C [22]. The interaction between β precipitates and dislocations cause the serrated hardening zone in the post-fire tensile stress-strain curves for exposures above 400°C.

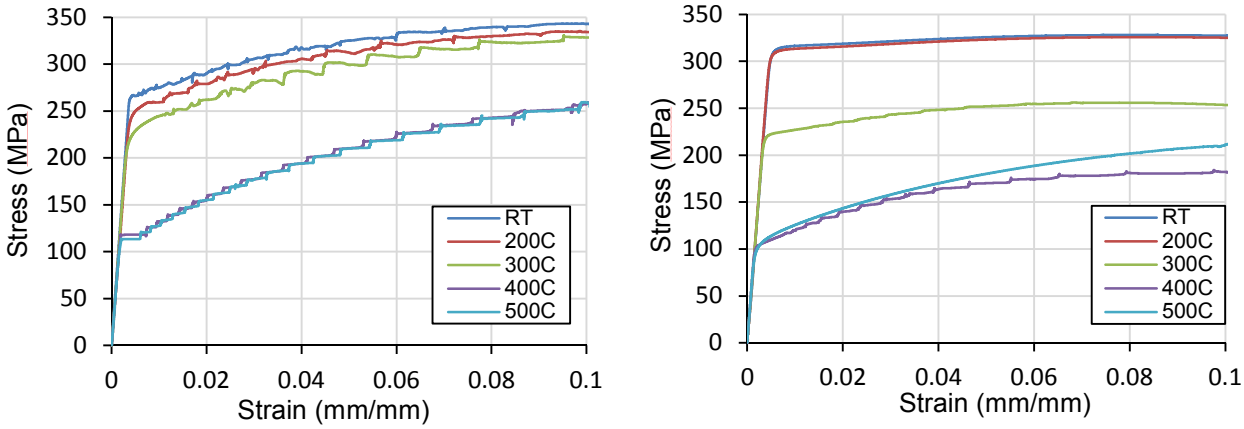

Fig. 6. Post-fire stress-strain relations (a) 5083-H116 (b) 6061-T651

As expected, with an increase in exposed temperature, the post-fire mechanical properties decrease. Post-fire mechanical properties for both alloys are summarized in Fig. 7. Exposure temperature up to 200°C have only small effect on 5083-H116 and almost no effect on 6061-T651. For both alloys, both yield and ultimate strengths decreases from 200°C to 400°C exposure temperature, the lowest post-fire strengths took place after 400°C exposure, as shown

in Fig. 7. Thus in the subsequent study, 400°C is selected to study the impact of aging time, heating and cooling rate in the post-fire mechanical properties for both alloy.

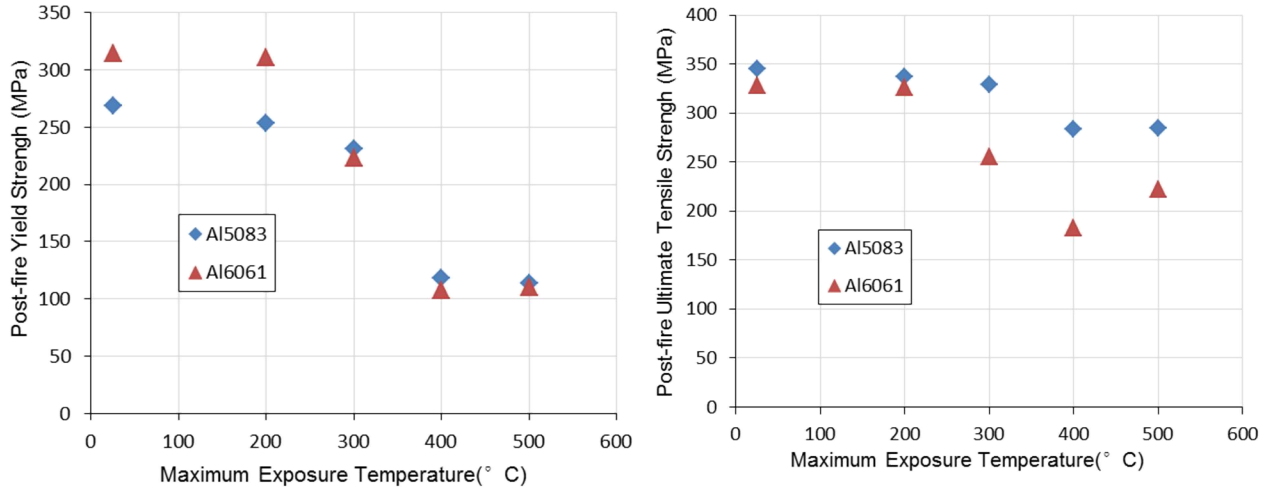

(a) (b)

Fig. 7. Post-fire mechanical properties (a) 5083-H116 (b) 6061-T651

The post-fire residual work hardening rate ($d\sigma/d\varepsilon$) also exhibits different behavior in Al5083 and Al6061. As seen in Fig. 6, a steady increase in residual work hardening rate with the increase of exposure temperature until 300°C is observed in Al5083 tensile behavior. For further exposure to 400°C and 500°C, the residual work hardening rate increases significantly. In contrast, Al6061 displays almost zero residual work hardening rate in the as-received and 200°C post-fire tensile behavior. After exposure to 300°C, the material experiences an increase in the residual work hardening rate. For further exposure above 300°C, the Al6061 residual work hardening rate also exhibits significant increase. A detailed study in plastic flow characteristics for both alloys are provided by Summers et al [5].

2.4 Effect of Heating Methods

In the 400°C exposure tests, the parametric study includes examining the effects of heating rate, cooling rate and aging time on the residual material properties. Both alloys were heat treated to 400°C by furnace heating and fire exposure, cooled down by water quench and air cool, then aged in room temperature for 1, 3, 10 and 30 days. After that, the residual material properties were measured by Vicker hardness test and post-fire uniaxial tensile test.

Post-fire yield strength and ultimate tensile strength were determined from the stress-strain relationships obtained in the tensile tests after the samples were heat treated and cooled down. The 0.2% proof stress method was used to calculate the yield strength and the ultimate tensile strength was determined based on the maximum stress achieved in a tensile test.

As shown in Fig. 8 and Fig. 9, compared to the as-receive specimen test results, post-fire yield strength and ultimate tensile strength for both Al5083-H116 and Al6061-T651 decreased after 400°C exposure. The post-fire yield strength decreased about 55% for Al5083-H116 while more than 60% for Al6061-T651. The post-fire ultimate tensile strength decreased only 18% for 5083-H116, but more than 45% for 6061-T651, which indicates Al6061-T651 is much more sensitive to heat exposure than Al5083-H116.

Test results from different heating and cooling methods, aging time are all listed in Fig. 8 and Fig. 9. Compared to as-received strength, the post-fire strength shows significant decrease for both alloys after 400°C exposure. For the post-fire strength after fire damage and cooling back to ambient temperature, the Al5083-H116 data shows similar values for different heating and cooling methods, which means the post fire strength of Al5083 is insensitive to heating rate and cooling rate. In addition, within the same set of columns, the bars also exhibit almost the same values for different aging time, which indicate the aging time does not affect the post-fire mechanical properties. Al6061-T651 data shows similar trends for cooling methods and aging time. However, different heating methods cause dramatic changes in post-fire yield strength and ultimate tensile strength: the furnace heated samples had a post-fire yield strength 80% lower than the as-received; while the fire exposure data decrease was 60% compared to the as received test specimen. For post-fire ultimate tensile strength, furnace heating samples had a 55% decrease in properties while fire exposure samples decrease 45% of the as received strength. These results indicate that the post-fire yield strength and ultimate tensile strength of Al5083-H116 are not sensitive to heating rate, cooling rate and aging time; for Al6061-T651 samples, they are not sensitive to the cooling rate and aging time, but sensitive to heating rate.

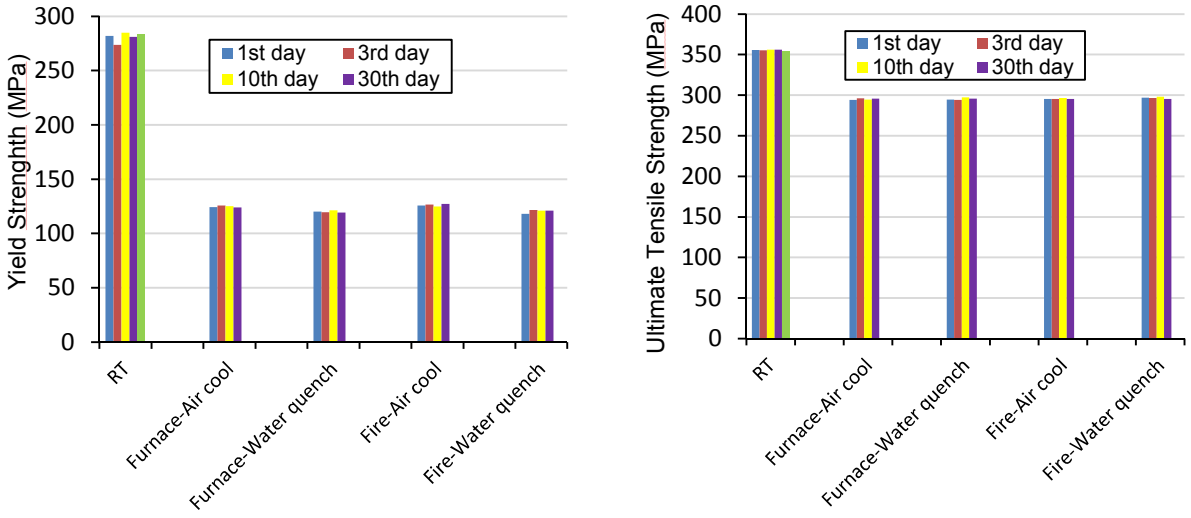

(a) (b)

Fig. 8. Post-fire (a) Yield strength and (b) Ultimate tensile strength for 5083-H116

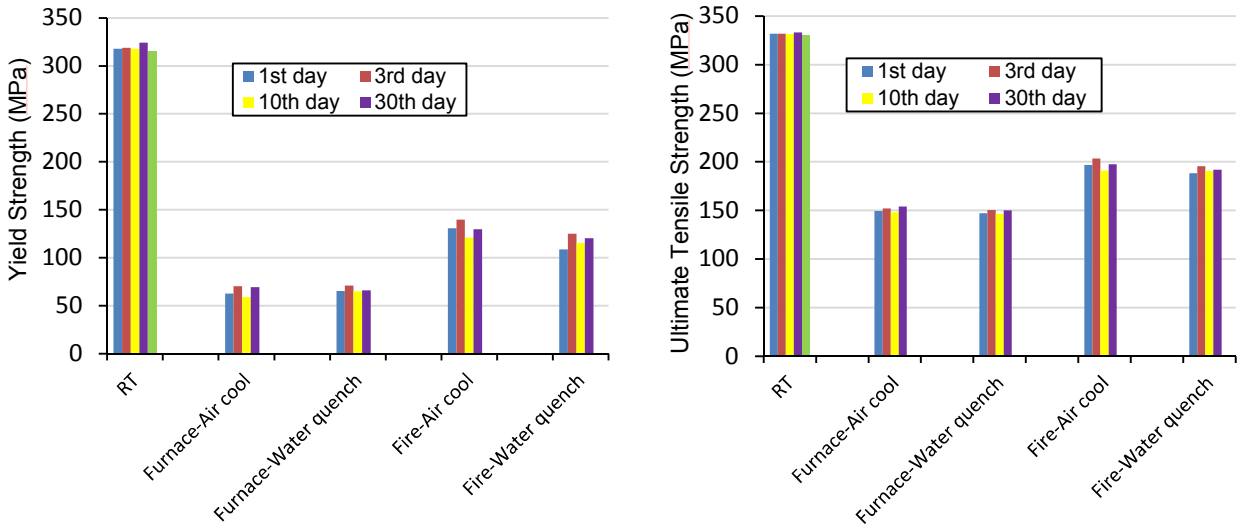

(a) (b)

Fig. 9. Post-fire (a) Yield strength and (b) Ultimate tensile strength for 6061-T651

2.5 Dependence on Heating Rate

To further investigate the heating rate effect on the residual material strength degradation of aluminum alloy, four heating methods including cone calorimeter heating, fire exposure, furnace heating and furnace heating plus 30 minutes soak time, which provide different heating rates, were applied to heat treat the samples to 400°C. The cone heater is an electric heater assembly

that provides irradiances ranging from 0 to 65 kW/m^2; it can produce heating rates up to 200°C/min.

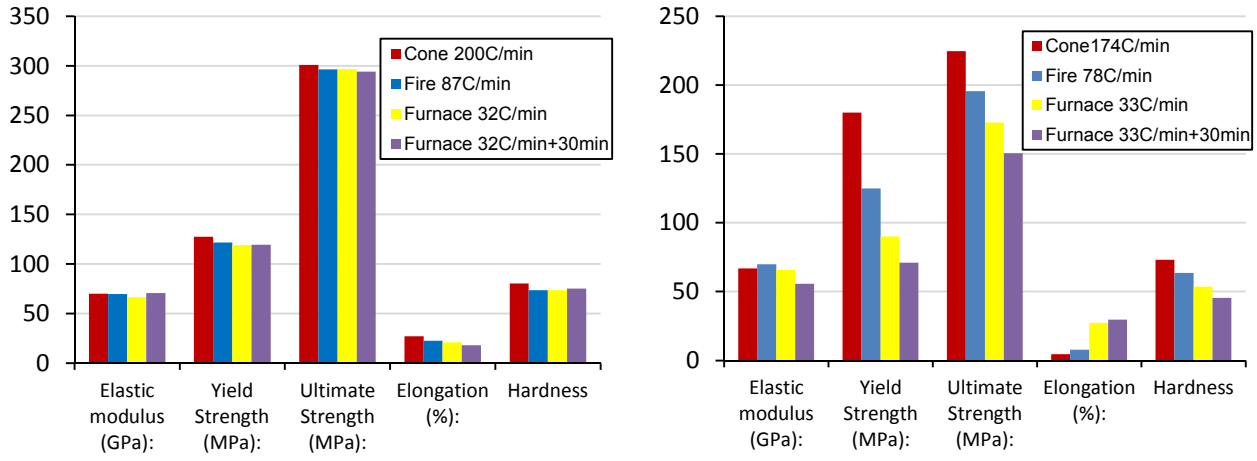

(a) (b)

Fig. 10. Heating rate effect on (a) 5083-H116 and (b) 6061-T651

Fig. 10 shows the post-fire tensile test results for both Al 5083-H116 and Al6061-T651 after heat treating by four methods, which provide different heating rates of approximately 180°C/min, 80°C/min, 30°C/min and 30°C/min followed by 30min soak time. As shown in Fig. 10(a), the four different heating methods cause little difference on the Al5083-H116 post-fire yield strength, ultimate tensile strength, elongation and hardness despite the wide differences in heating rates examined. As a result, we conclude that the 400°C post-fire mechanical properties of Al5083-H116 exhibit nearly no sensitivity to heating rate. Based on the post-fire mechanical properties analysis by Summers et al. [5], material strength degradation for Al5083 includes two parts: the initial reduction below 280°C caused by the subgrain coarsening during the dislocation recovery and the primary reduction between 280°C to 380°C due to the static recrystallization, which annihilates the subgrain structure. Grain recrystallization initiates at temperatures between 280°C to 320°C depending upon the heating rate. However, recrystallization initiates at about the same residual strength independent of heating rate and causes similar strength reductions. Therefore, material strength reduces to similar value after grains are fully recrystallized at approximate 380°C. This phenomenon provides the explanation for the residual strength of Al5083 is insensitive to the heating rate at 400°C.

However, Al6061-T651 shows significantly different results: the post-fire yield strength and ultimate tensile strength decrease with the decreasing heating rate; the material ductility increases with the decrease of heating rate. Vickers hardness test results are also consistent with post-fire ultimate tensile strength. As discussed by Summers et al. [5], Al6061 is a precipitation hardened alloy and is strengthened by the interaction of precipitates and dislocations, which is in terms of precipitate size and volume fraction. This interaction will be weakened by the elevated temperature growth of the strengthening phase. Therefore, the yield strength will be reduced. The strength degradation initiates when the precipitate grows from the β″ to β′ phase at temperatures range from 250°C to 300°C depending on the heating rate. Since the peak temperature of β″, β′, and β-phase precipitation increases with the increase of the heating rate, the residual strength degradation also initiates at higher temperature associated with the formation of β′ precipitate. The β precipitation peak is identified at approximately 460°C with 20°C/min heating rate, which indicates that the strength degradation has not been completed at 400°C. Therefore, for 400°C post-fire tests, the residual strength of Al6061 is still sensitive to the heating rate: the higher heating rate, the higher the precipitate peak temperature and the lower the strength degradation.

2.6 Hardness Correlation

As we discussed previously in regard to heating rate effect, the change in post-fire hardness is consistent with the change of post-fire yield strength and ultimate tensile strength. To study the hardness correlations with the post-fire residual strength, the Vickers hardness versus post-fire yield strength and ultimate tensile strength for both 6061-T651 and 5083-H116 are plotted in Fig. 11 and Fig. 12.

In a previous study, Tabor [72] suggested that Vickers hardness could be correlated to the material strength in an elastic-perfectly plastic material. Theoretical model has been developed to calculate material's ultimate strength in term of diamond pyramid hardness and Meyer's hardness coefficient, m, which can be determined from the strain hardening coefficient, n , as shown in Eq. (1) and (2) [73]. Considering both the strain hardening effect and different indenter geometries, correlations between hardness and yield strength in strain hardening materials have also been developed in Eq. (3) [74], where σ_y and σ_u are the yield strength and ultimate tensile strength, H is the Vickers hardness, E is the young's modulus.

$$\sigma_u = \frac{H}{2.9}\left[1-(m-2)\right]\left[\frac{12.5(m-2)}{1-(m-2)}\right]^{(m-2)} \quad (1)$$

$$n = m - 2 \quad (2)$$

$$\frac{H}{\sigma_y} = \frac{2}{3}\left\{\left(1-\frac{1}{n}\right)+\left(\frac{3}{4}+\frac{1}{n}\right)\left(\frac{1}{3}\frac{E}{\sigma_y}\cot\alpha\right)^n\right\} \quad (3)$$

Since the strain hardening coefficient, *n*, is not constant for the as-received and post-fire materials, *n* values are fitted from the as-received and post-fire stress strain curves to present the strain hardening effect on hardness. The fitting curves based on the correlation model for both elastic power-laws hardening material and perfect elastic-plastic material are plotted in Fig. 11 and Fig. 12.

Compared to the experimental data, the yield strength-hardness correlation model for elastic-perfectly plastic behavior under predicts materials' hardness. This is as expected, as no strain-hardening behavior is included in the model. For the Al6061, the predicted correlation between hardness and yield strength is in good agreement with the experimental results. However, the hardness prediction for Al5083 is not in agreement with the data; the reason for this discrepancy is unclear. In many works, attempts have been made to develop linear correlations between hardness and yield strength. We note that the predicted hardness-yield strength curve for strain hardening materials is concave down. Thus, linear fits to it (or to experimental hardness versus yield strength data) are expected to have hardness intercepts which are greater than zero.

The correlation between hardness and ultimate tensile strength calculated by the strain hardening model for both materials are plotted in Fig. 12. The theoretical model gives very good prediction for the post-fire ultimate tensile strength for both Al5083 and Al6061. However, for the as-received material with higher ultimate strength, the theoretical model gives under prediction for Al5083 and over prediction for Al6061 ultimate strength.

The above data and models indicate that Vickers Hardness can be correlated to a material's residual strength after fire damage based on the power-law strain hardening model. Thus, as a

simple and convenient test method, Vickers Hardness can be used to estimate the post-fire yield strength and ultimate tensile strength for aluminum alloys after fire exposure.

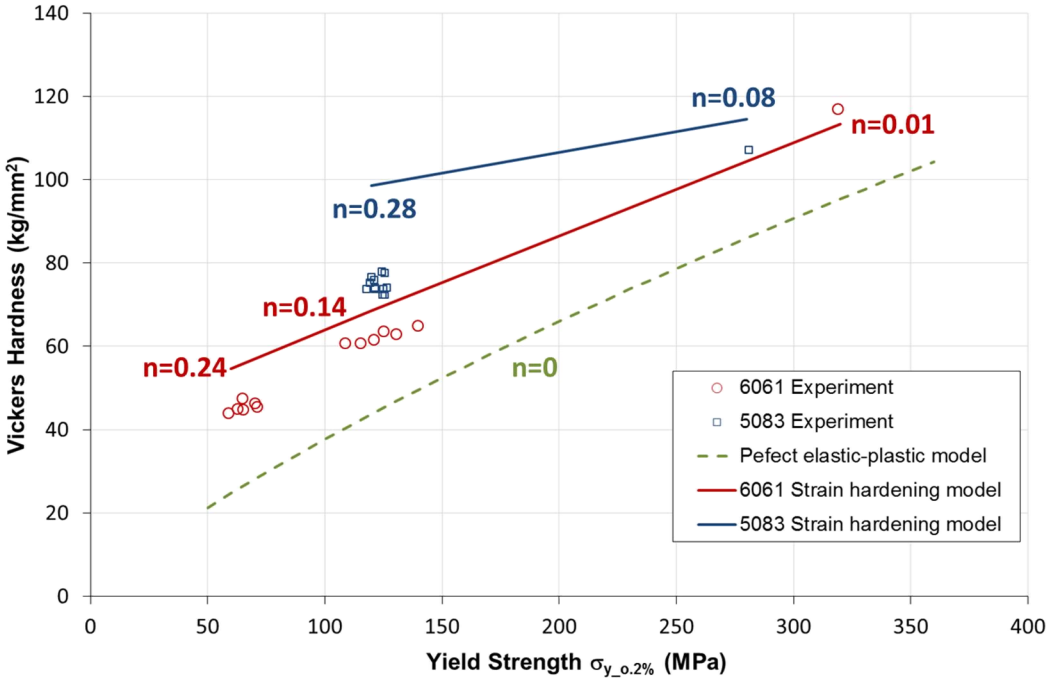

Fig. 11. Vickers hardness correlations with yield strength

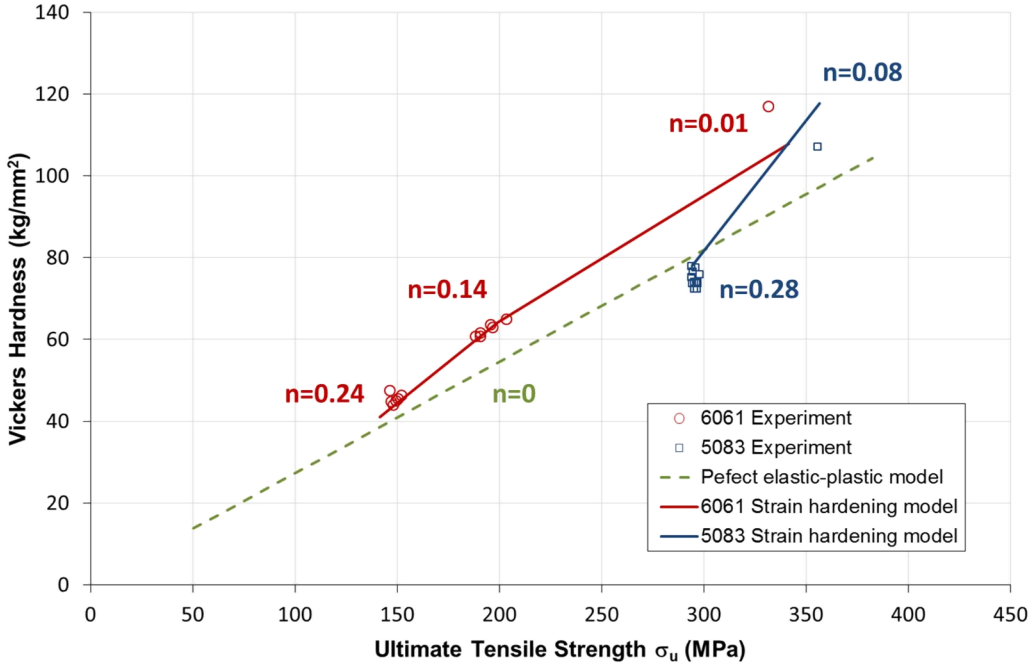

Fig. 12 Vickers hardness correlations with ultimate tensile strength

2.7 Conclusion

In this chapter, the post-fire tensile behavior and the response to different heating methods and aging times were studied for both Al5083-H116 and Al6061-T651 alloys. Different tensile behaviors were exhibited in the low exposure temperatures below 300°C for both alloys. However, for higher exposure temperature 400°C and 500°C, both alloys exhibit dynamic strain aging effect and significant increase in residual work hardening rate ($d\sigma/d\varepsilon$).

The study on the effects of different heat treatment methods at the 400°C critical temperature shows that the post-fire behavior of Al5083-H116 was insensitive to heating rate, cooling rate and aging time; Al6061-T651 samples were found to be insensitive to the cooling rate and aging time, but sensitive to heating rate. These phenomenon were explained by the different mechanisms in microstructure evolution: Al5083 has completed grain recrystallization after 400°C exposure; while the precipitation sequence in Al6061 are dependent on the heating rate, 400°C is still within the temperature region where β′ phase dissolution and β-phase precipitation.

The correlation between Vickers Hardness and the post-fire residual strength base on elastic power-law hardening model indicates that the Vickers Hardness test can be a simple and reliable method to estimate the post-fire residual strength for aluminum alloys after fire exposure.

CHAPTER 3 - Cavitation Development

3.1 Introduction

Aluminum alloys as lightweight and high strength materials have increasingly been used in load-bearing structural applications in the aerospace, automotive, marine, and mechanical industry. One potential concern with the use of aluminum is its behavior during extreme fire conditions. During fire exposure, the material strength may be degraded and failure may occur because of the accumulation of fire damage. This damage to aluminum is a complex combination of thermal exposure damage and stress-induced damage.

Previous studies have indicated that aluminum alloys exhibit significant strength degradation during elevated temperature thermal exposure. Normalized elevated temperature Young's modulus, yield strength, and ultimate strength are summarized in Eurocode 9 [11] and the American Society of Metals Handbook [12]. Similar elevated temperature properties were measured by Allen [4]. Due to thermal exposure, internal microstructural damage may be accumulated in surviving aluminum structures after returning to ambient conditions. The thermally-induced microstructural damage and corresponding residual (post-fire) mechanical behavior were also studied [5, 16]. However, these researchers only studied the thermally-induced damage and did not account for the stress influence on microstructural damage and post-fire response of the load-bearing aluminum structures.

In addition to the stress-free thermally-induced fire damage, stress also plays an important role to cause thermo-mechanical damage to aluminum alloys. These damages in aluminum are complex and may be a combination of grain growth, precipitate cracking, and cavity formation [6-8]. In situations where the fire is extinguished and the structure remains intact, a key concern is the future performance of the thermo-mechanically damaged structure. In order to predict the post-fire performance of fire damaged aluminum structure, a detailed understanding of the developed stress-induced microstructural damage is necessary.

Cavitation is examined as one major types of stress-induced damage in aluminum alloys during thermo-mechanical deformation. Premature failure may occur due to the cavity nucleation, growth, and the subsequent coalescence. Cavity nucleation requires significant stress

concentration that is orders of magnitude greater than the applied stress [23, 25]. The early idea of vacancy agglomeration was from the nuclei (precipitation and solid inclusions) [24]. Grain boundary sliding and dislocation pile-up will generate sufficient local stresses and promote the formation of cavities, particularly when they occur against precipitates on the grain boundaries [31, 32]. Existing cavities will also cause stress concentration and lead to new cavity formation as the damage progresses [33]. Once formed, cavity growth is primarily driven by two different mechanisms: vacancy diffusion and creep plasticity [34, 35, 42]. The comparison between diffusive cavity growth and plastic cavity growth demonstrated that cavities grow faster when driven by plasticity. Grain boundary sliding has also been considered as another mechanism for cavity growth [39].

A number of creep damage studies have been performed on superplastic aluminum alloys [75-78]. The effects of thermal exposure and stress state on the cavitation evolution were investigated. It was found that diffusive cavity growth and the effect of creep plasticity in the surrounding material can be coupled. Cavity growth was verified to be controlled by diffusion when cavities are small (<0.5 μm), then controlled by power-law creep when they are large (>0.5 μm) [44]. Cavities may grow initially by diffusion, then by coupling of diffusion and creep plasticity, and finally by creep plasticity alone. A plastic cavity growth model was proposed, implying that with an initial cavity volume fraction value, cavities grow exponentially with the increase of creep strain [75].

This work seeks to establish a fundamental level of damage quantification to aid in the analysis of these simultaneously evolving mechanisms. In this section, a uniaxial stress state was induced during tensile creep experiments to simulate fire exposure conditions. Tests were interrupted at multiple engineering creep strain to investigate the cavitation damage. Cavity development associated with the creep response was examined by two-dimensional scanning electron microscopy, high resolution optical microscopy, and three-dimensional X-ray micro-tomography. The cavitation evolution in both 5083-H116 and 6061-T651 aluminum alloy during creep were examined to study the stress-induced microstructural damage mechanism.

3.2 Experimental

3.2.1 Materials and Sample Geometry

The materials included in this study are the same marine-grade aluminum alloy AA5083-H116 and AA6061-T651 used in Chapter 2. The nominal chemical compositions for both alloys are shown in Table 1. Aluminum 5083-H116 is a work-hardened alloy that contains 4 - 4.9% of magnesium as its major alloying element. This alloy is known for exceptional performance in extreme environments and has excellent resistance to seawater and corrosive chemicals. Aluminum 6061-T651 is a precipitation hardened aluminum alloy; the major alloying elements are 0.8 – 1.2% of magnesium and 0.4 – 0.8% of silicon. It exhibits good weld ability and also has good corrosion resistance to sea water and chemicals. Both alloys are frequently used in ship construction.

The material was supplied by Alcoa in form of 6.35mm inch thick sheets. Test sample geometry was selected based on the ASTM standard E21-09, as illustrated in Fig. 13. Specimens were machined from the as-received plate to dog-bone geometry with the longitudinal axis oriented in the rolling direction. The specimens had an overall length of 304.8mm and uniform thickness of 6.35mm, with a gage length and width of 190.5 and 12.7 mm, respectively. All test samples of each alloy were machined from the same aluminum sheet to keep uniform material properties. Sample geometry is designed by NX Unigraphics software, and then machined using a Tormach PCNC 1100 Mill.

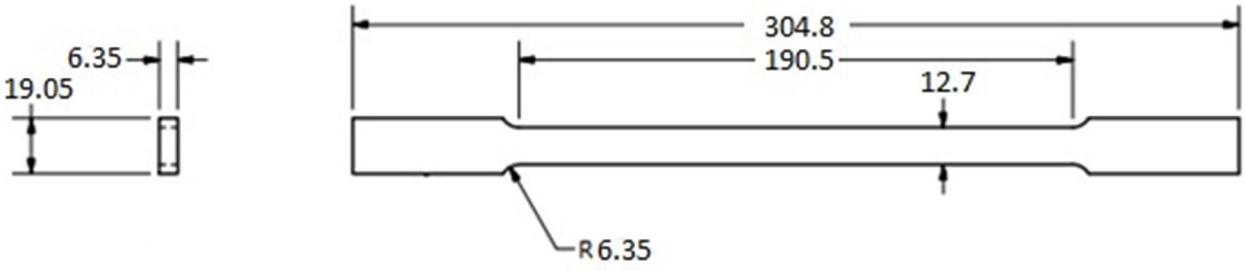

Fig. 13. Tensile test specimen geometry (mm)

3.2.2 Simulated Thermo-Mechanical Test (creep test)

A previous post-fire study [5] indicates that the strength degradation of Al5083 during thermal exposure without applied stress is attributed to two types of microstructural changes: (1) an initial strength reduction below 280°C primarily caused by the subgrain coarsening during dislocation recovery [79] (2) the primary strength reduction from about 280°C to 380°C due to static recrystallization, which annihilates the subgrain structure change. Grain recrystallization initiates at different temperature from about 280°C to 320°C depending upon the heating rate. Recrystallization initiates at approximately same residual strength (235MPa) and leads to similar strength degradation; which is observed to be independent of heating rate. For Al6061, the post-fire yield strength experiences a relatively steady reduction from 200°C - 450°C. After exposure to 500°C, an increase in yield strength is observed. The initiatial yield strength degradations caused by precipitate growth from the metastable β″ to β′ phase from approximately 250 - 300°C. Significant reduction in residual yield strength after exposure to 400°C is due to the β′ precipitate dissolution and equilibrium β phase formation.

Thus, the following temperatures were chosen to separate the stress-induced microstructural damage during thermo-mechanical creep from damage induced solely due to thermal exposure: 200°C as the subgrain coarsening and initial strength degradation temperature for Al5083; 300°C as the initial recrystallization temperature for Al5083 and precipitate transformtion from β″ to β′ phase for Al6061; 400°C as the complete recrystallization temperature for Al5083 and equilibrium β phase formation for Al6061.

During the thermo-mechanical tests, the thermal exposure step was performed with an Ameritherm 5060LI Induction heater. A Micro-Epsilon optical infrared pyrometer and a Watlow PID controller were used to control the induction heater to provide the desired sample temperature. The induction coil was designed in a curved shape to provide uniform temperature to the center region of the samples, as shown in Fig. 14b. To separate the stress-induced damage from the damage due to solely thermal exposure, both thermal exposure tests and thermo-mechanical tests were performed to evaluate the post-fire performance.

For all thermo-mechanical tests, samples were heated to the specified temperature at a constant heating rate. Since precipitate evolution in Al6061 at 20°C/min heating rate has been studied in

literature, 20°C/min heating rate was selected to perform the thermos-mechanical tests for Al6061. Higher heating rate of 50°C/min was selected in Al5083 creep test due to grain structure evolution is not that insensitive as the precipitate evolution in Al6061. The following mechanical step was performed using a Material Tests System (MTS) 880 Load Frame. The test programs are controlled by a MTS Micro Profiler, as shown in Fig. 15. A preselected stress was applied once the samples reached the target temperature. Samples were then held at constant temperature and stress for a period of time. Data acquisition was performed through LabView program to record the real time load, stroke, strain and exposure time during the creep tests. Tests were interrupted at various exposure times to investigate the stress-induced damage at multiple engineering creep strains.

For the tests with only thermal exposure, samples were heated under the same heating rate and then held at same target temperature for the same exposure time as the corresponding thermo-mechanical creep test. No stress was applied during the exposure, samples are restrained on both ends to prevent freely expand. Only small thermal expansion strain (~1%) was measured in the sample center during thermal exposure, which was recovered after sample cooled back to ambient temperature.

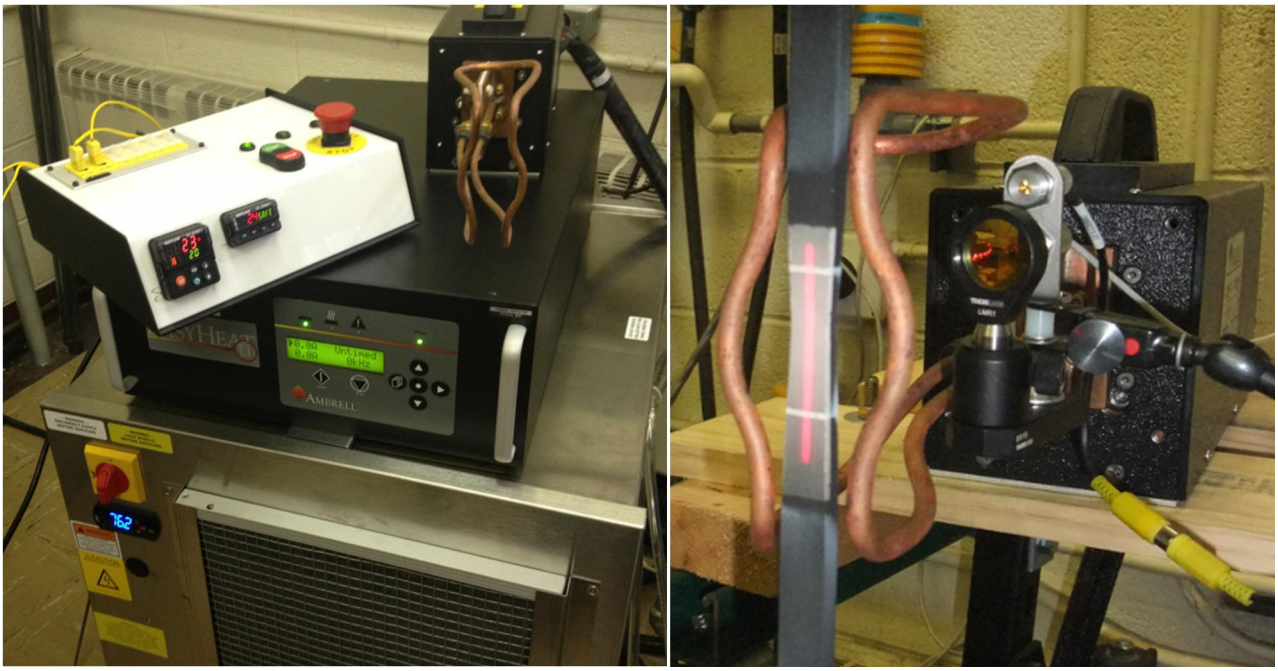

(a) (b)

Fig. 14 (a) Ameritherm 5060LI Induction heater (b) Induction heating coil

(a) (b)

Fig. 15 (a) MTS 880 Load Frame (b) MTS Micro Profiler

3.2.3 Strain Measurement

Strain measurement is an important process to record the material deformation during the mechanical tests. Various methods have been used to perform the strain measurement, including strain gauges, mechanical extensometer, digital image correlation, and laser extensometer, etc. Although strain gauges and mechanical extensometer can provide very accurate strain data, they need to be attached on the sample surface to read the deformation. In a high temperature environment, both strain gauge and mechanical extensometer may lose contact with the surface and result in loss of accuracy. Thus strain gauge and mechanical extensometer are not suitable for the elevated temperature mechanical tests.

Digital image correlation (DIC) technique is a fast and high-accuracy optical method for strain measurement. The principle of the DIC measurement method is tracking the same subsets located in the reference image and deformed image to retrieve the full-field displacements. The Newton–Rapshon (NR) algorithm has been adopted as the gold standard for accurate sub-pixel displacement tracking in DIC technique [80]. As a non-contact optical measure metrology, DIC method can provide accurate full field displacement and strain information for the test sample. Thus DIC technique was the first choice for strain measurement in the thermo-mechanical tests. As shown in Fig. 16, the DIC measurement is coupled with the induction heater to measure the

creep strain during thermo-mechanical test. High temperature paint which can remain effective up to 648ºC is applied to paint the center region of test sample. The paint pattern of white dots distributed randomly in the black background provides high resolution to the DIC deformation measurement, as shown in Fig. 17.

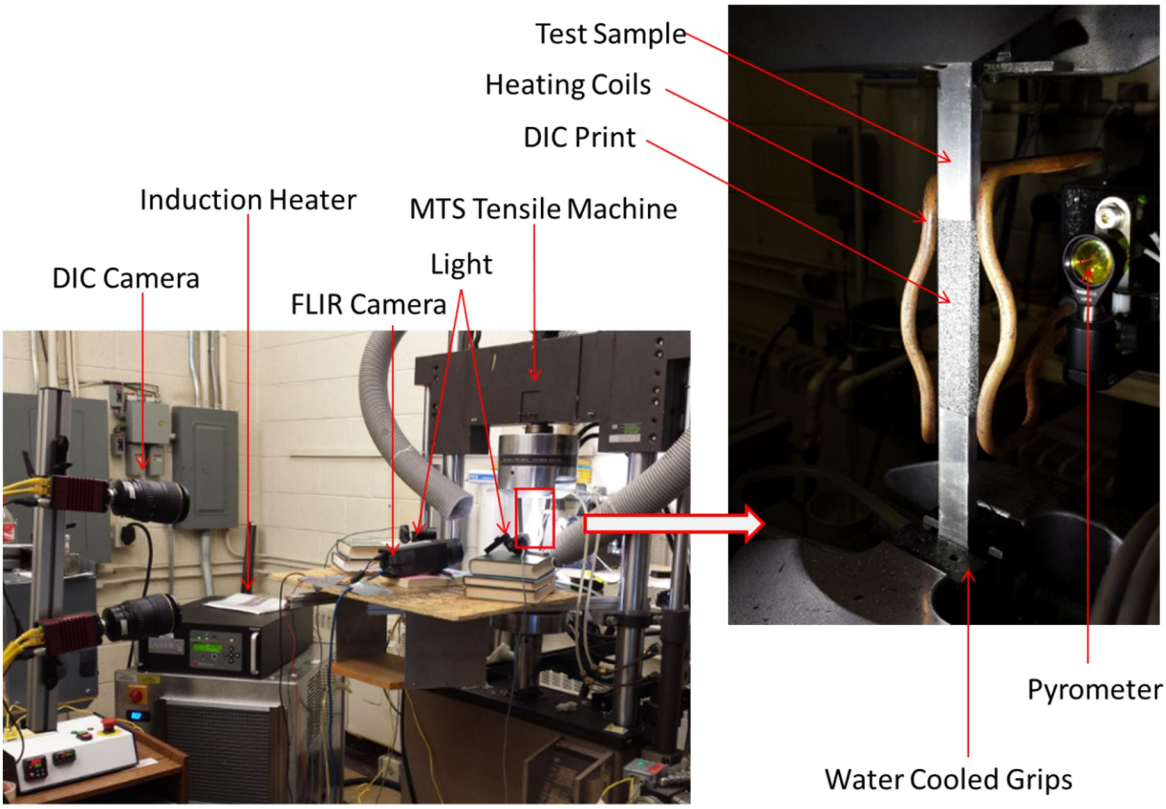

Fig. 16 DIC strain measurement applied in the thermo-mechanical tests

Fig. 17 Paint pattern for DIC test sample

However, DIC has several drawbacks for the strain measurement in the thermo-mechanical tests. The paint peels off when sample experiences large plastic deformation in the center region, even

when high temperature paint was applied. Thus the strain information may be lost at the high strain stage before sample failure, as shown in Fig. 18. Another disadvantage is the DIC method cannot provide real-time strain information during the thermo-mechanical tests. All the deformation and strain data are obtained during post-test processing. These two drawbacks prevent the use of DIC to determine the pre-selected strains during creep tests to investigate the stress-induced damage in these experiments.

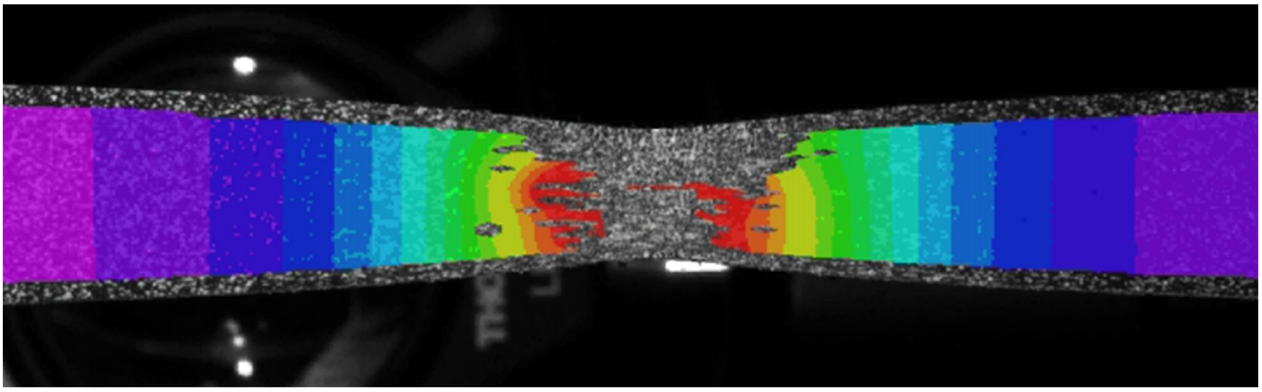

Fig. 18 Strain data lost at high strain for the DIC measurement during creep test

Laser extensometry is another non-contact optical method to measure the sample deformation. Compared to the DIC measurement, the laser extensometer is a relatively convenient measurement technique and is suitable for one-dimensional strain measurement. A 55mm long laser line is projected on the sample center to perform the strain measurement within a designated region (the distance between two white reference lines). The major drawback of laser extensometer is the limitation of measurement length. Since the creep strain at failure is about 150% for Al5083 (less for Al6061), 22mm gage length is selected to perform the stain measurement. Within the 22mm gage length, both maximum creep strain and the strain localized (necking) region can be fully captured.

As shown in Fig. 19, a Fiedler Optoelektronik GmbH laser extensometer is applied in the creep tests to measure engineering strain over a 22mm gage length. Real time strain information can be read from the sensor during the creep test; thus suitable strain can be determined to stop the creep and investigate the stress-induced damage at multiple stages.

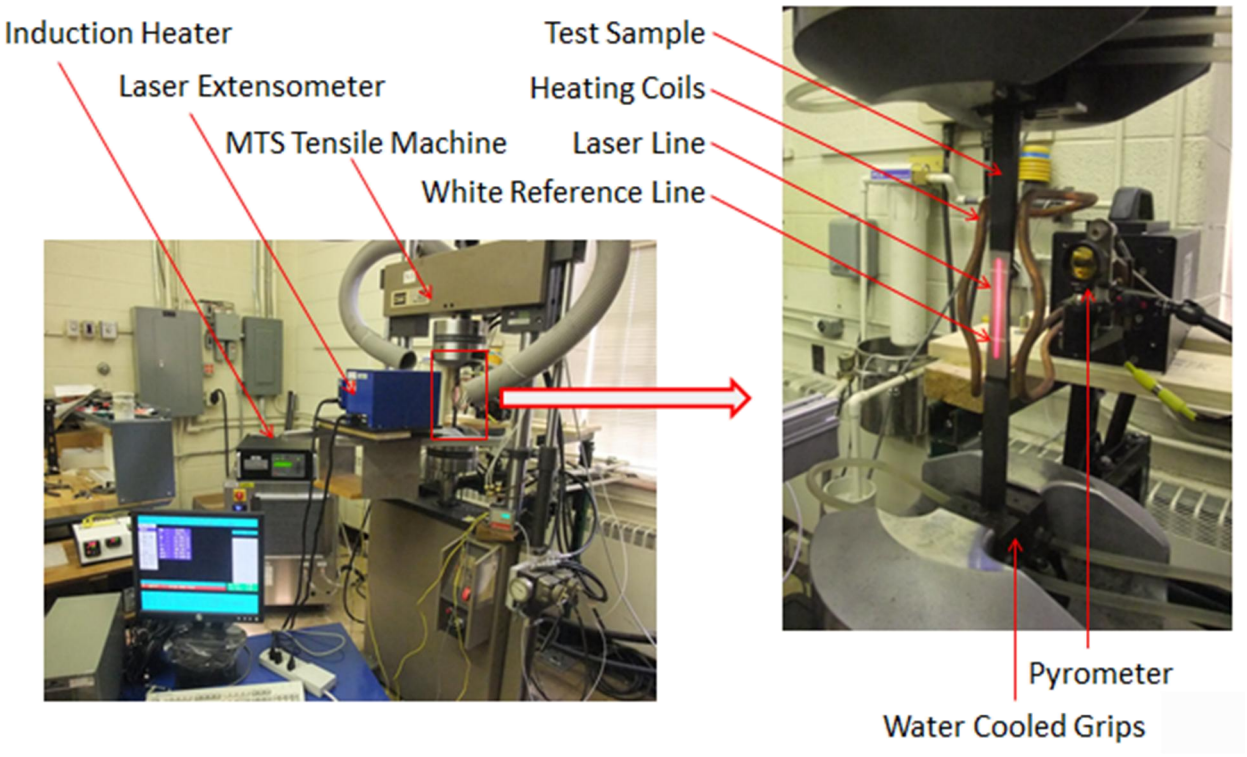

Fig. 19. Laser extensometer strain measurement applied in thermo-mechanical tests

3.2.4 Microstructural Quantification

After thermo-mechanical tests, samples demonstrated necking in the center of the gauge region, indicating the presence of creep-induced damage. Sections were cut from the necked regions (approximately 6 mm in length) to examine the microstructural damage. Samples were mounted in the epoxy base and polished to a mirror finish using multiple steps of SiC grinding, 3μm and 1μm diamond polishing, and 0.5μm colloidal silica final polish. The polished sample surface is then examined by the secondary electron detector of a FEI Quanta 600 FEG SEM at low accelerate voltage and Zeiss Axiovert.A1 MAT optical microscope. Element quantification of some large intemetallics is performed by Energy Dispersive Spectrometer (EDS).

To understand the stress-induced damage mechanism, these two-dimensional characterization techniques were performed on all three perpendicular material surfaces of the damaged sample (rolling, transverse and normal surfaces, as shown in Fig. 20). Both cavity morphology and volumetric development with the accumulation of creep strain were examined.

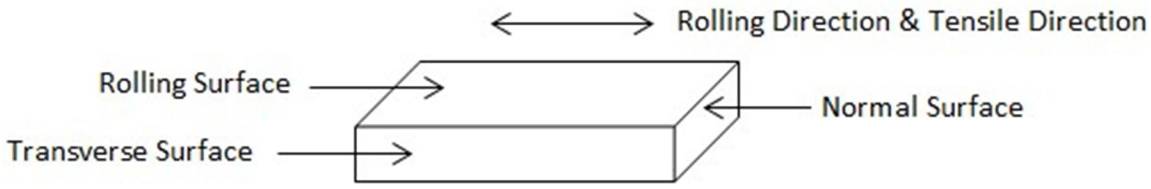

Fig. 20. Sectioning terminology

SEM images for each sample, including tem images for each surface (rolling, transverse and normal) at different location, were collected to quantify the cavity volume faction. Images taken at 500x magnification were selected to study cavity evolution. This magnification shows a sample surface area of 512×443μm, which is the optimal size to analyze cavities larger than 1μm and measure the overall creep damage state. To estimate the cavity volume fraction, grey-scale SEM images were converted to binary images using a thresholding process in Matlab. The threshold value was adjusted for each SEM images based on their contrast and brightness. The average cavity size was calculated based on the total cavity area and the number of cavities in each image (assuming spherical cavities and circular cross-sections).

3.3 AA5083-H116 Cavitation Evolution

3.3.1 Cavitation Dependence on Temperature

Cavitation development in Al5083 at various exposure temperatures was examined. Fig. 21 compares the microstructure evolves from the unstressed thermal exposure condition to strained thermal-mechanical condition at multiple temperatures. Fig. 21a-c illustrates the solely thermal exposure microstructures without applied stress. No cavitation is observed in these sample surfaces, indicating that the thermal exposure condition by itself does not cause the cavity formation. In contrast, cavities developed in the samples with mechanical load due to the local stress concentration inside the material. The following cavity growth is controlled by diffusion when cavities are small, then controlled by coupling of diffusion and creep plasticity, and finally by creep plasticity alone [44]. Thus the development of the cavitation is primarily dependent on the plastic strain. Fig. 21d-f displays the microstructures from samples which were tested at different temperature and stress levels to reach various strains during the creep tests. It is apparent that cavity size and volume fraction increase with the increase of creep strain.

The high temperature properties of Al5083 shows that the material ductility increases with the increase of sample temperature [4]. For the same exposure time, samples at higher temperatures exhibit more plasticity than samples at lower ones. As shown in Fig. 21d, due to the low plastic strain (15%) before sample failure, cavitation has not been developed in the 200°C, 140MPa strained sample yet. However, the material ductility is highly increased after 300°C and 400°C exposure; strains before creep failure are about 136% for 300ºC and 150% for 400ºC. In Fig. 21e and f, 100% and 143% engineering creep strain samples are shown. The small spherical cavities appear on the 300°C, 100% strained microstructure; while the 400°C, 143% strained sample is close to fracture, large creep strains are produced around the surface of the cavities and the small cavities are driven to coalesce into larger irregular shape and randomly distribute inside the sample [14]. Grain boundary sliding occurs during the large plastic strain also promotes cavities grow into large size.

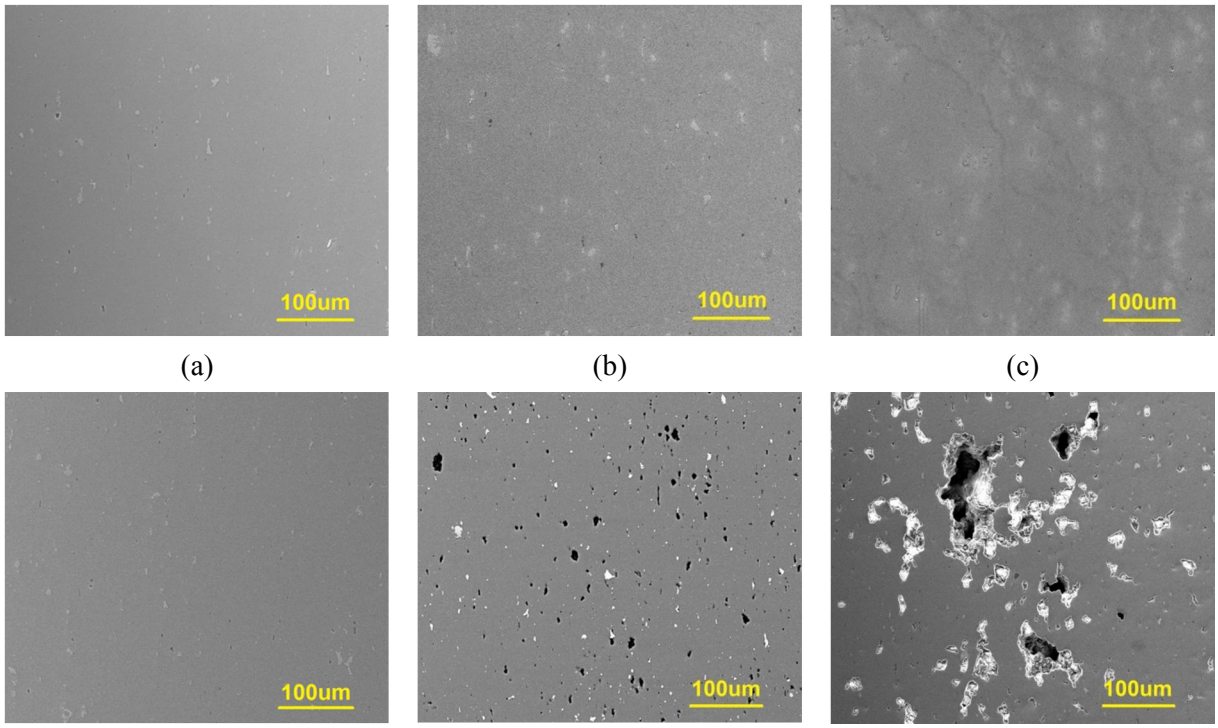

Fig. 21 Cavitation evolution from solely thermal exposure state to thermo-mechanical damaged state (a) 200°C, 2000s, (b) 300°C, 2000s, (c) 400°C, 2000s, (d) 200°C, 140MPa, 2000s, ε=15%, (e) 300°C, 50MPa, 2000s, ε=100% and (f) 400°C, 17MPa, 2000s, ε=143%

3.3.2 Cavitation Evolution at 400°C

Samples exposed to 400°C temperatures exhibit more cavitation damage than samples exposed to other temperatures. Previous work on the Al5083 alloy revealed that 400°C was a critical temperature at which grain recrystallization was completed, and the lowest post-fire yield and ultimate strengths occurred after 400°C exposure [16]. Thus 400°C was chosen to study the effect of creep stress and strain on microstructural damage in this work. Samples were heated from room temperature to 400°C at a controlled heating rate of 50°C/min. Loads corresponding to a engineering tensile stress of 17MPa, 15MPa, or 14MPa were applied once the sample reached 400°C. Samples were then soaked in constant loading and temperature to achieve specified creep strains. As shown in Fig. 22, the creep tests were interrupted at engineering strains of 50%, 80%, 100%, and 143% for samples subjected to a constant tensile stress of 17 MPa; 100% and 133% axial strain for 15MPa; and 100% and 144% for 14MPa.

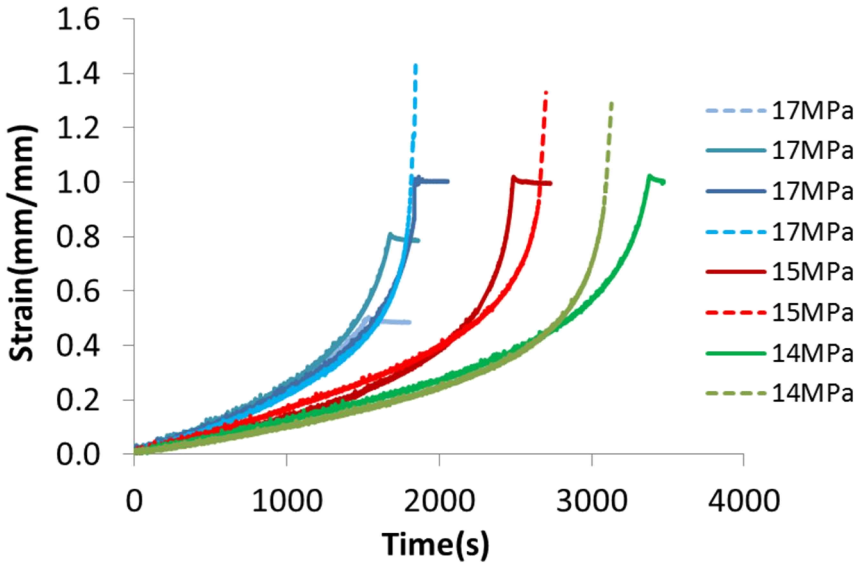

Fig. 22. Creep curves of the fire-load conditioning tests for Al5083 samples

As mentioned previously, samples were interrupted at various creep strains to isolate various stress-induced damage states, as shown in Fig. 23. Both strained and fractured (broken) samples tested at 17MPa, 15MPa and 14MPa are shown in Fig. 23a-c with the fractured samples on the right side of each sample set. Large plastic deformation and severe necking were observed in the fractured samples. The fracture surfaces are almost necked to a thin line, with a 90% reduction in area, indicating highly ductile failure. Fig. 23d shows an isolated view of the necked portion for

a highly deformed and damaged sample tested at 14MPa. Several cracks are observed on the rolling surface indicating impending failure. Similar cracks are also observed on the neck surface of 17MPa, 143% strain creep sample. These highly damaged samples have similar elongation to the fracture ones shown in the right in Fig. 23 indicating they have reached a state just prior to material failure. For the 15MPa and 133% strain sample, necking is not as severe as those strained to 143% and 144% at 17MPa and 14MPa; no cracking was observed on the sample surface, implying that this sample was approaching failure but had not yet reached the just-before-fracture state.

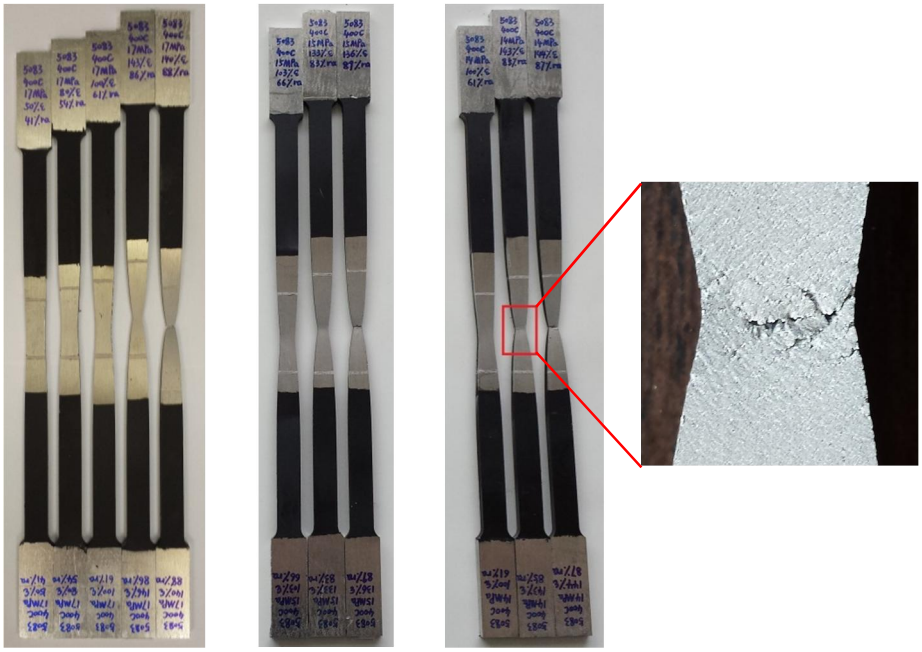

(a) (b) (c) (d)

Fig. 23 (a)17MPa, 50%, 80%, 100%, 143% creep strain and fracture samples (b)15MPa, 100%, 133% creep strain and fracture samples (c)14MPa, 100%, 144% creep strain and fracture samples (d) Necking region of just-before-fracture sample

Microstructures of the damaged samples were examined by SEM to observe the cavitation evolution with the development of creep strain, as shown in Fig. 24. Creep damage is manifested by the increase in the number of visible cavities as well as the growth of those cavities. The cavities are randomly distributed and appear darker on the light aluminum background. Fig. 24a shows the as-received microstructure, no cavities were observed in the aluminum matrix except for several randomly distributed Fe and Mn-rich intermetallic inclusions. In thermo-mechanical loading conditions, significant stress concentrations will be generated around the intermetallic

and on the junction of grain boundaries. New cavities will nucleate at these locations due to sufficient local stress concentrations during the plastic deformation.

Strain localization and necking occurs with the increasing plastic strain. Severe necking coincides with stress-induced damage accumulation in the sample; one of the features is cavity growth. For creep microstructures at strains lower than 100%, the cavities appear mostly spherical shape, randomly distributed on the inner sample surface. The cavity sizes at these strains are relatively small and similar. As the creep strain exceeds 100%, the cavities begin to grow and agglomerate; more cavities with elongated shapes appear in the microstructure. This indicates the cavities are stretched and coalesce at high creep strains. After the sample deforms beyond 100% creep strain and approaches failure, more spherical cavities were stretched and coalesce into crack-like cylindrical cavities parallel to the rolling/loading direction with lengths ranging from 50μm-150μm and aspect ratios larger than 5.

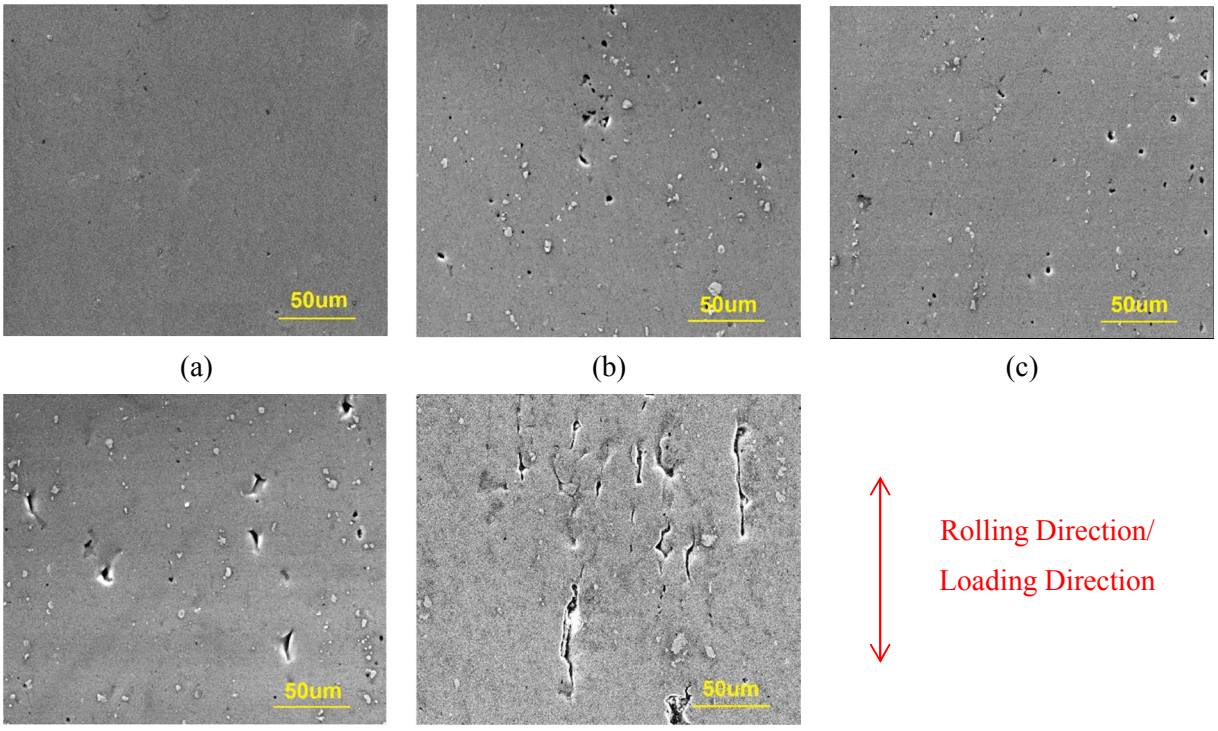

Fig. 24 Cavitation evolution with creep strain for Al5083(SEM, 500x, rolling surface) (a) as-received ε = 0%; and 400ºC 17MPa applied stress (b) ε = 50% (c) ε = 80% (d) ε =100% (e) ε = 143%

Closer inspection of the microstructures on each sample surface gives more evidence of creep cavity orientation, as shown in Fig. 25. The rolling and transverse material planes display

vertical crack-like cylindrical cavities along the rolling/loading direction, while spherical cavities are randomly distributed on the normal material plane. The cavity morphologies indicate that during high plastic deformation, creep cavities grew from an initial spherical shape into the longer, cylindrical shapes along the rolling/loading direction. Similar cavity morphologies are displayed on all three material planes of the 17MPa and 14MPa samples, indicating similar damage has been developed during the creep tests within 14MPa-17MPa range. Several small cracks are also observed in the microstructure just prior to rupture, as shown in Fig. 25f. These cracks grow transversely to the rolling/loading direction and connect the closely spaced cavities, implying micro-cracks will develop after cavity coalescence and crack propagation causes eventual sample failure.

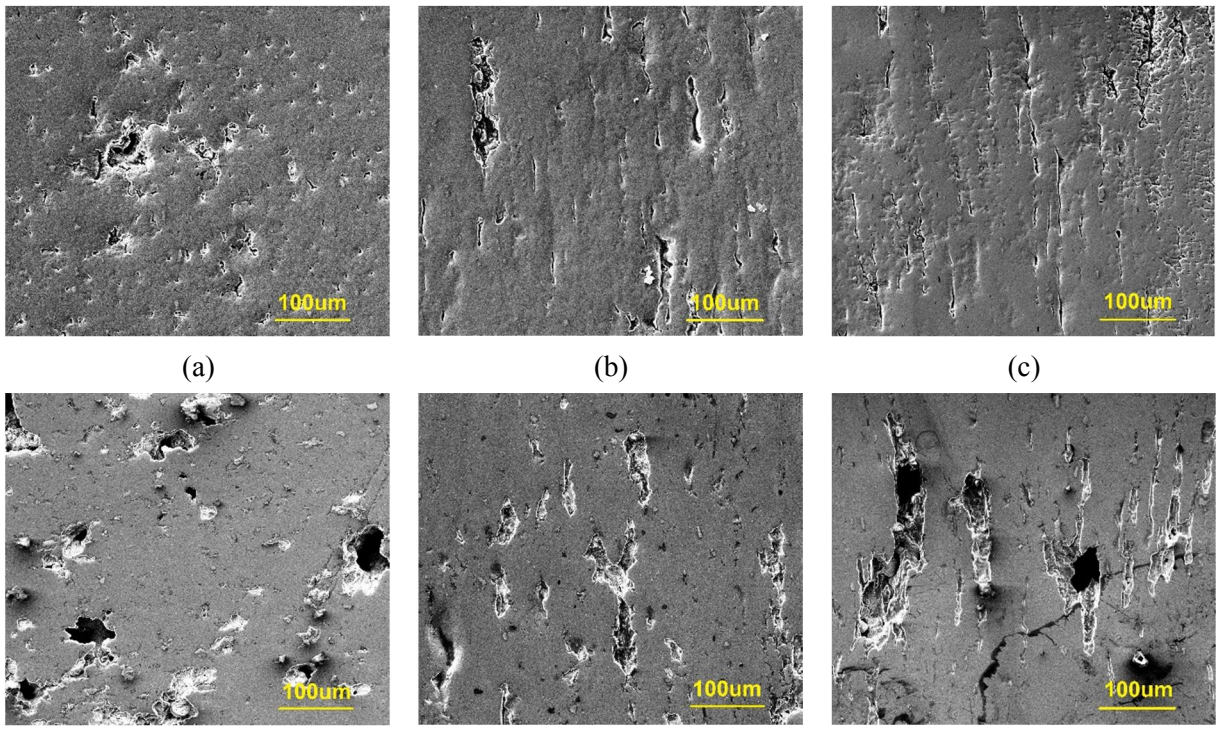

Fig. 25 Just-before-rupture samples creep cavity morphology on each material plane (SEM, 500x) (a)17MPa, Normal (b)17MPa, Rolling (c)17MPa, Transverse (d)14MPa, Normal (e)14MPa, Rolling (f)14MPa, Transverse

Cavitation can be quantified based on cavity volume fraction and cavity size in the deformed material. As shown in Fig. 26, the cavitation parameters for the above microstructures are summarized for multiple creep strain and stress levels. For samples subjected to 17MPa stress, the cavity volume fraction shows a gradually increasing trend with increasing creep strain below

100%; however, it is limited to 1% cavity volume fraction at 100% strain. As the sample continues to deform above 100% creep strain, sample necking becomes more severe and the rate of cavity growth dramatically increases. However, the critical cavity volume fraction before sample failure is still relatively small (approximately 4.7% for 17MPa applied stress).

Similar quantification was performed for samples with 14MPa and 15MPa applied stress. Samples with 100% creep strain and those at the just-before-fracture state (approximately 140% strain) were selected to compare the stress-dependence of creep damage. As shown in Fig. 26a, the cavity volume fractions at 100% strain are about 1% for all 14-17MPa creep samples. The just-before-fracture data of 14MPa and 17MPa samples also gives similar cavity volume fraction (around 5%), which corresponds to the similar microstructural damage states in Fig. 25. Thus 5% cavitation can be defined as the critical cavity volume fraction before sample failure. The 15MPa, 133% strain sample exhibits about 3% cavity volume fraction, which lies between the volume fractions at 100% axial strain and the just-before-rupture state. The standard deviations of the cavity volume fraction at multiple locations are more than +/- 1% for the just-before-fracture state, which is quite large compared to the small standard deviations below 100% strain. These large values of standard deviation associated with cavity volume fraction are also coincident with the non-uniform distribution of large crack-like cylindrical cavities inside the necking region when the material is approaching failure.

Cavity size evolution with creep strain is similar to that for cavity volume fraction. As shown in Fig. 26b, the average cavity size gradually increases below 100% strain and sharply increases when creep strain exceeds 100%. Cavity sizes are similar at the same creep strain levels for all 14-17MPa applied stress levels. The randomly distribution of large crack-like cavities also cause larger standard deviation of cavity size at the just-before-fracture states.

Previous work has indicated that the cavity growth transitions from diffusion-controlled to plasticity-controlled with the enlargement of cavity size. In the small cavity state, cavity growth is dominated by the diffusion-controlled mechanism and migrates along the boundaries. In contrast, plasticity-controlled growth is the dominant mechanism at large cavity sizes under high creep strain [81]. The superplastic cavity growth model [82] suggests a critical cavity size of 0.5 μm. When average cavity size is smaller than 0.5 μm, cavity growth is diffusion-controlled; cavitation is plasticity-controlled when the cavity size is greater 0.5 μm. Fig. 26b shows that the

average cavity sizes are greater than 0.5 μm for all tested conditions. Thus, cavity growth during Al5083 creep is primarily plasticity-controlled based on the data gathered in this work.

When cavity growth is plasticity-controlled, the cavity volume fraction can be given by a simple model in Eq.(4):

$$\phi = \phi_0 \exp(\eta\varepsilon) \tag{4}$$

Where ϕ is the cavity volume fraction at the strain ε, ϕ_0 is the initial cavity volume fraction of the as-received material, and η is a growth parameter usually ranging from 2 to 4, and is dependent on material, strain rate, temperature, and grain size. An exponential fit based on the data collected at all stress levels in Fig. 26a yields an η of 2.07, which lies between the upper bound value of 2.5 calculated by Cocks and Ashby's model and the conservative value of 1 predicted by Budiansky [83, 84].

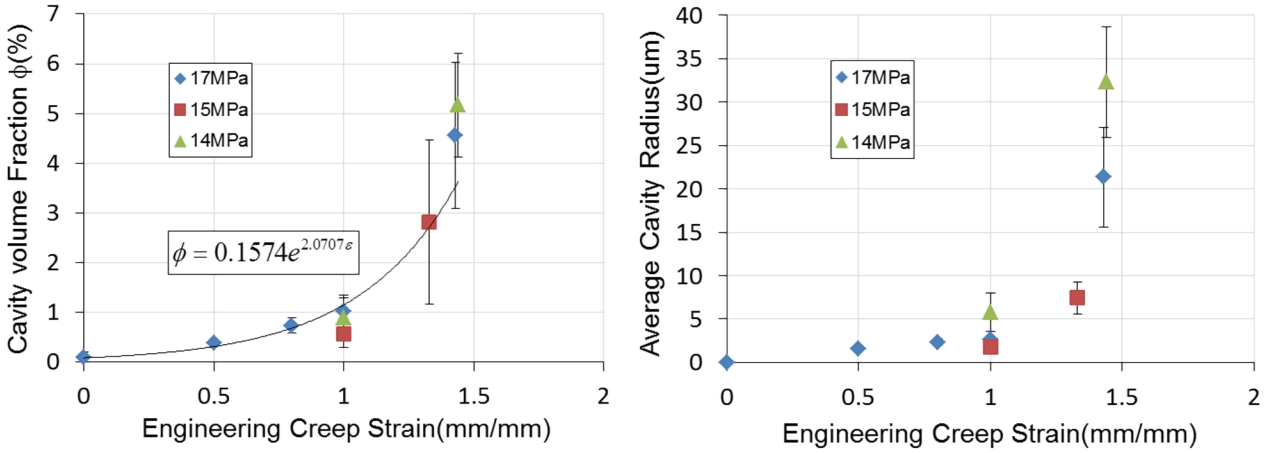

(a) (b)

Fig. 26 (a) Cavity volume fraction versus creep strain (b) Average cavity size evolution versus creep strain

3.4 AA6061-T651 Cavitation Evolution

3.4.1 Cavitation Dependence on Temperature

Cavitation development in Al6061 is also examined for 200°C-400°C exposure temperature. Both unstressed thermal exposure and strained samples which were exposed for the same duration are examined to study the effect of stress on the cavitation nucleation and growth. Since Al6061 is strengthened by precipitation, the damaged microstructure after thermal exposure appears more features than Al5083. Fig. 27 displays the as-received and thermo-mechanical damaged microstructure for Al6061. In the as-received microstructure, no cavities were observed in the aluminum matrix except for some Mg and Si rich intermetallic inclusions randomly distributed on the surface. After simulated fire exposure at 400°C, some large rod shape precipitates appeared in the damaged microstructure. The primary element of these rod shape precipitates examined by the Energy Dispersive Spectrometry is Si. Some cavities have also been developed due to the local stress concentrations on the grain boundaries and around precipitates during the plastic deformation.

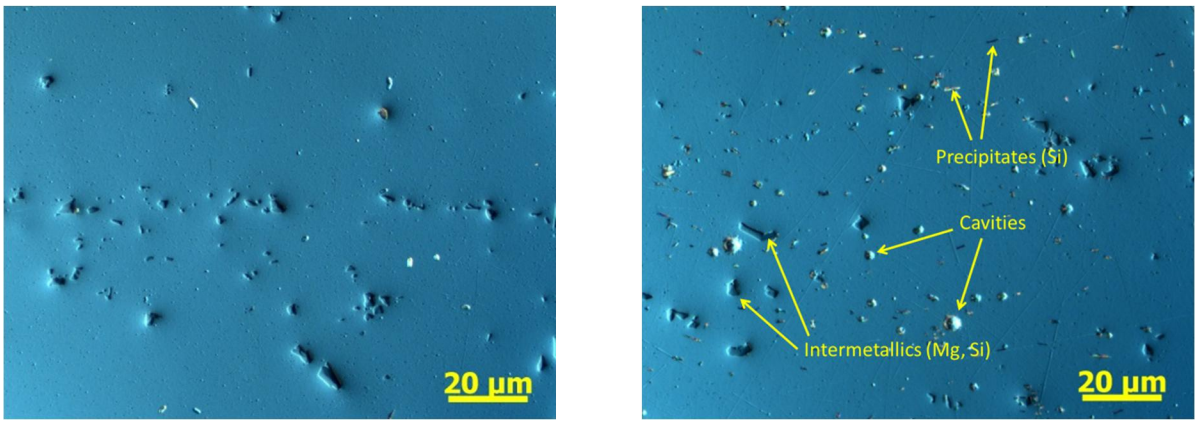

(a) (b)

Fig. 27 Microstructures of Al6061 (a) As-received (b) 400°C, 20MPa, ε = 47%

Cavitation developments from solely thermal exposure state to thermo-mechanical damaged state are examined at different exposure temperatures. Fig. 28a-c, d-e, f-i exhibit the unstressed thermal exposure and strained microstructures tested at 200°C, 300°C and 400°C respectively. Since the solely thermal exposure condition does not cause any cavity formation, no cavitation is observed in the solely thermal exposure samples. Even these samples were soaked in the

elevated temperature for extended durations, no cavities will be developed due to the solely heat treatment.

As the stress was applied, samples began to creep and large plastic deformation developed with the increase of exposure time. The severely damaged states for each exposure temperature were examined to explore the stress-induced cavitation before sample fracture. In Fig. 28c, the strained sample exposed at 200°C does not show any cavity formation; there are only several intermetallic inclusions randomly distributed in the microstructure. This phenomenon occurs because the material ductility has not been greatly increased at the low temperature exposure. The strain before sample failure (12%) is too low to cause local stress concentration. However, a significant number of cavities are displayed on the strained microstructure tested at 300°C and 400°C, as shown in Fig. 28f and i.

The damaged state in Fig. 28f and i are close to sample fracture at 300°C and 400°C exposure. Samples heat treated to 400°C have higher ductility than those exposed to 300°C, thus the 400°C strained sample obtains higher strain (58%) before facture than the 300°C one (19%). However, the cavitation displays opposite feature with ductility in the just-before-fracture states exposure at 300°C and 400°C. Although the 400°C strained sample has higher strain (58%) before facture than the 300°C one (19%), the number of cavities in the 300°C strained sample appears more than the 400°C strained one. These cavities remain spherical shape instead of being stretched into large cylindrical shape before sample failure, which is distinctive with the just-before-fracture state in Al5083. Quantification data also shows the 300°C strained sample has a lager critical cavity volume fraction before failure (4.4%) than the 400°C strained sample (1.9%). These differences in the stress-induced cavitation development result in distinct fracture mechanism in 300°C and 400°C creep samples. Fig. 29 exhibits the fracture surfaces for samples creep at both temperatures. The large amount of cavitation leads to brittle fracture of the 300°C creep sample; while 400°C creep sample experience a more ductile failure due to the higher ductility and lower cavitation in the before failure stage.

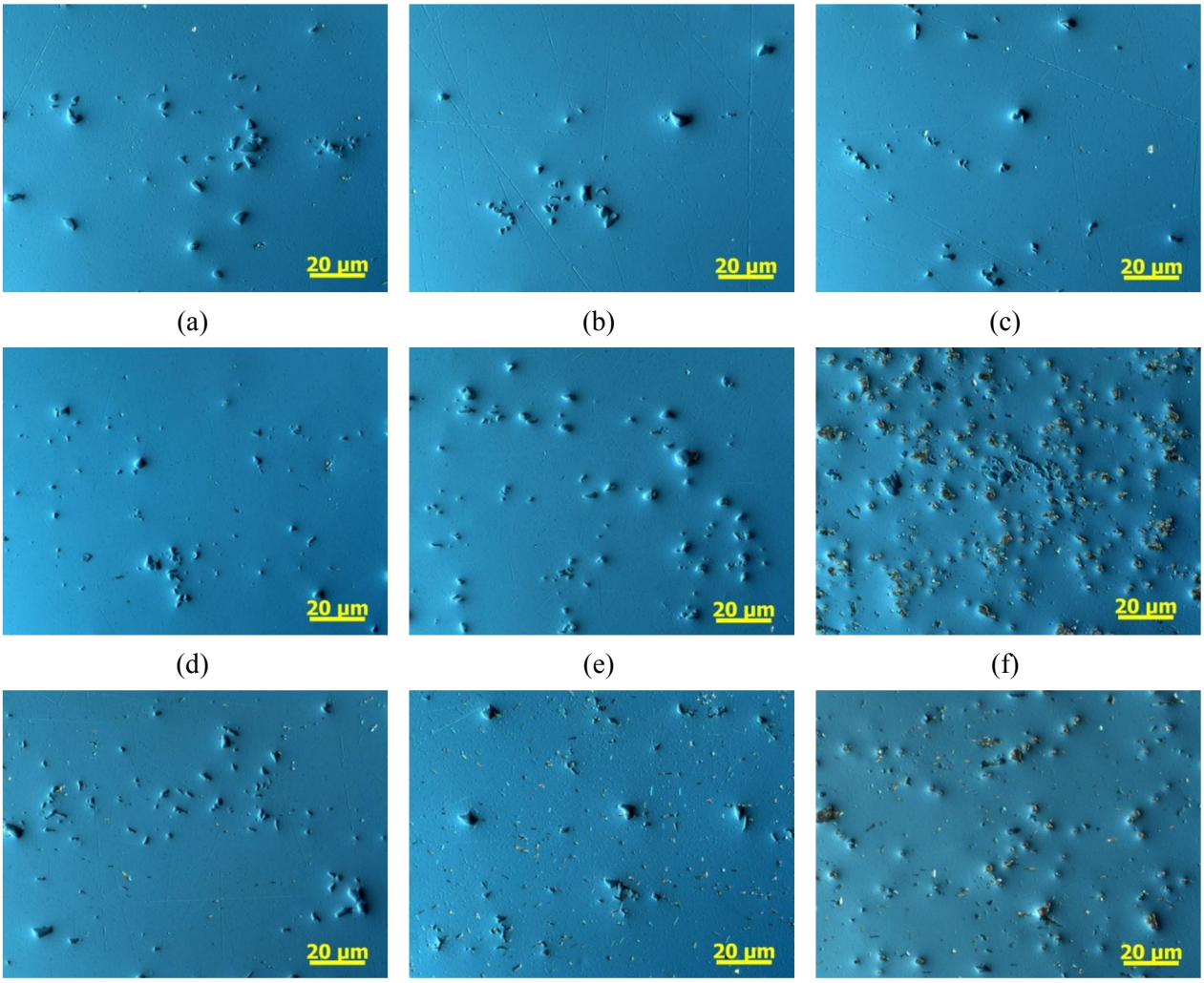

Fig. 28 Cavitation evolution from solely thermal exposure state to thermo-mechanical damaged state

(a) 200°C, 0MPa, 0s, (b) 200°C, 0MPa, 2000s, (c) 200°C, 220MPa,1400s, ε=12%

(d) 300°C, 0MPa, 0s, (e) 300°C, 0MPa, 4000s, (f) 300°C, 80MPa, 4000s, ε=19%

(g) 400°C, 0MPa, 0s, (h) 200°C, 0MPa, 2900s, (i) 400°C, 20MPa, 2900s, ε=58%

Fig. 29 Fracture surface of thermo-mechanical tested samples (a) 300°C, (b) 400°C

3.4.2 Cavitation Evolution at 400°C

400°C was also a critical temperature for Al6061 alloy; since the equilibrium β phase precipitates at 400°C. After heat treatment at 400°C, the material exhibits the lowest post-fire yield and ultimate strengths and highest ductility. It is constructive to explore the cavitation development with the increase of creep strain, and how cavitation leads to ductile failure for Al6061 at that temperature. Thus thermo-mechanical tests at 400°C were interrupted at multiple engineering creep strain from 25% to 58% (before fracture) to examined the stress-induced damaged states.

Fig. 30 displays the as received microstructure and cavitation evolution with the increase of creep strain at 400ºC, 20MPa tested condition for Al6061. As expected, the unstressed thermal exposed sample in Fig. 30b exhibits similar microstructure to the as received state: no cavitation appears except for some Mg-Si rich intermetallic inclusions randomly distributed on the sample surface. When samples are strained after stress applied, local stress concentrations will be generated at the grain boundaries, particularly around the precipitates and at the junction of grain boundaries. Cavities will nucleate at those locations where the local stress concentration is sufficient to pull the material apart. As shown in Fig. 30c-f, some cavities have appeared on the creep samples surface with the accumulation of creep strain. As we discussed in the cavitation evolution for Al5083, cavity growth primarily depended on the creep strain. Since the ductility of Al6061 is not as high as Al5083 during elevated temperature exposure, the strain before Al6061 sample failure is only around 60%, which is much lower than the 150% creep strain before Al5083 failure. Therefore, compared to the cavitation evolution in Al5083 alloy, cavitation in Al6061 strained microstructures are quite low and the area fractions are less than 1% for creep strains under 50%. Even the critical cavity area fraction is only 1.9% before Al6061 sample fails at 400 ºC. Moreover, the cavity morphology remains spherical shaped until Al6061 sample failure. No cavities have been stretched to large cylindrical shapes as those in Al5083 before fracture state. Thus the stress-induced cavity damage in Al6061 is not that intense as Al5083.

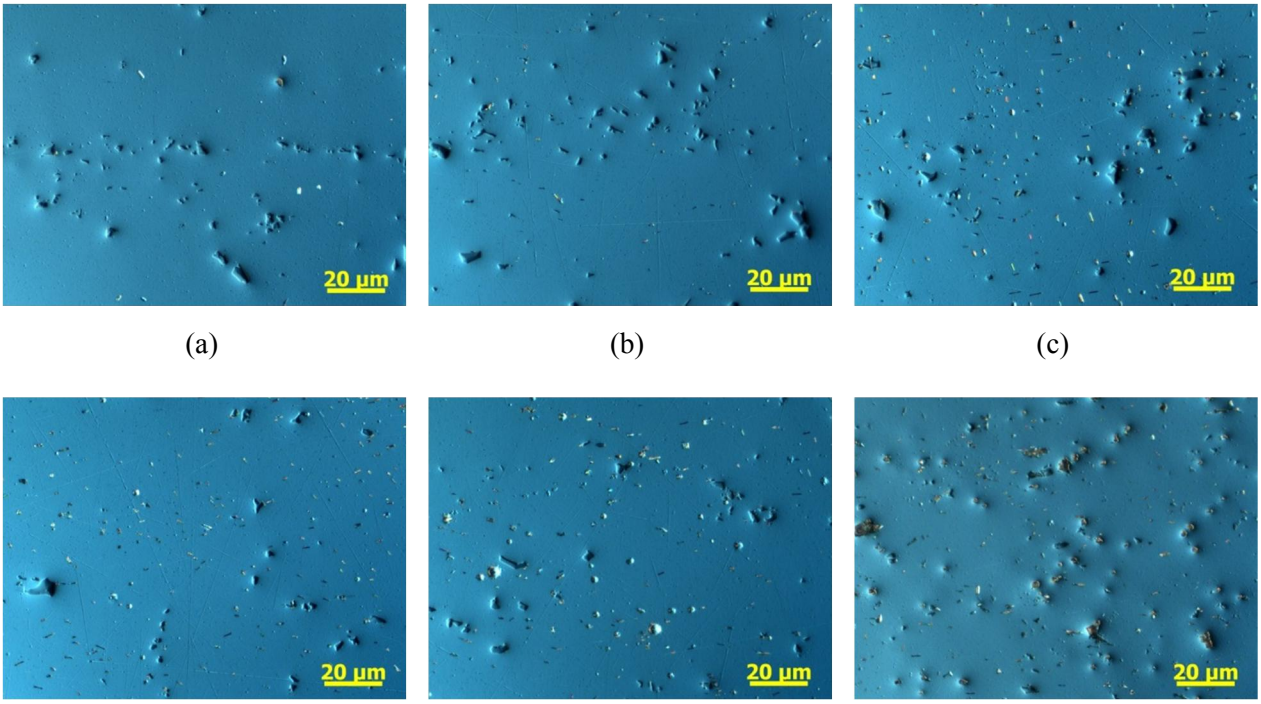

(a) (b) (c)

(d) (e) (f)

Fig. 30 Cavitation evolution with creep strain (1000x, rolling surface) for Al6061
(a) As-received ε = 0%; (b) 400ºC, 0MPa, 0s, ε = 0%;
and 400ºC, 20MPa (c) ε = 25% (d) ε = 36% (e) ε =47% (f) ε = 58%

3.5 Conclusion

This work examined the damage evolution in both unstressed thermal exposure and strained samples for both Al5083 and Al6061 thermo-mechanical tested samples. Two-dimensional techniques including scanning electrical microscopy (SEM) and high resolution optical microscopy were applied to study the internal stress-induced cavity damage.

Cavitation at various creep strain levels was analyzed to study the damage mechanism at 200ºC - 400ºC. Stress concentrations promote cavity formation on the grain boundaries while creep plasticity dominates the subsequent cavity growth. In both alloys, cavitation has not been developed in 200ºC thermo-mechanical tested samples due to the low ductility. The creep strain before sample failure in the 200ºC creep tests is less than 20%. Cavitation is developed at 300ºC and 400ºC strained samples, but exhibits different features for both alloys.

For Al5083, the ductility is highly increased after 300ºC and 400ºC exposure; strains before creep failure are about 136% for 300ºC and 150% for 400ºC. The cavity morphology changes from a small spherical shape at low strain level to a large crack-like cylindrical shaped cavities orientated along the rolling/loading direction at higher strain. The cavity volume fractions are quantified and exhibit an increase as a function of creep strain.

However, Al6061 strained samples exhibit relative low cavitation due to the limitation in the elevated temperature ductility. The critical cavity area fraction before sample failure is only 1.9% for 400ºC thermo-mechanical tests. The cavities remain spherically shaped until sample failure. Samples strained at 300ºC exhibit more cavities and as a result exhibit brittle fracture, while 400ºC has higher ductility and low cavitation and lead to ductile failure.

CHAPTER 4 - Grain Structure and Precipitation Evolution

4.1 Introduction

Aluminum alloys are frequently used in marine applications due to their light weight, high strength, exceptional corrosion resistance, good weldability, and formability. A major concern in the marine application of aluminum alloys is the mechanical performance of materials after fire exposure, i.e., the residual (post-fire) mechanical behavior of thermo-mechanically damaged aluminum. This aspect is important for evaluation of structural stability of aluminum structures after a fire.

In previous studies, it has been shown that aluminum alloys exhibit significant strength degradation during and after elevated temperature exposure. The strength degradation due to heat treatment is closely related to the microstructural damage inside the materials. Numerous studies have been conducted to examine thermally-induced microstructural damage including dislocation recovery, recrystallization, and precipitation sequence [19-22, 79]. Among those microstructural damages types, evolution of grain structure and precipitation has been shown to make significant contributions to the material strength degradation after fire exposure. Grain structure change is the major feature to cause residual strength degradation in Al5083. The subgrain coarsening during dislocation recovery below 280°C has been shown to cause about 15% strength reduction in Al5083 [79]; from 280°C to 380°C grain recrystallization caused the major strength degradation. More than 50% strength reduction is observed after grain recrystallization in Al5083. In contrast, Al6061 is a precipitate hardened alloy; the precipitation evolution sequence is the main factor to cause material strength degradation during thermal exposure. The transformation from β″ to β′ phase at temperatures from approximately 250 - 300°C causes initial strength degradation in Al6061 and the following equilibrium β phase formation causes significant reduction in residual yield strength after exposure to 400°C.

However, these previous studies have only examined the thermal effect on the microstructural damage and the resulting impact on post-fire response. Limited research has been done to examine the influence of stress on grain structure and precipitation evolution and the resulting impact on post-fire response. In addition to the grain recrystallization and precipitate evolution

caused by thermal exposure, stress will cause additional damage to the microstructure during plastic deformation. As discussed in the previous chapter, cavity nucleation and growth occurs in association with the accumulation in plastic strain. Structural failure will occur due to the coalescence of cavities and crack growth. In addition to cavitation, dynamic recovery (DRV), dynamic recrystallization (DRX) and dynamic precipitation also occur during thermo-mechanical process and are classified as the stress-induced microstructural damage for aluminum alloys [46-49].

Dynamic recovery is a softening effect during plastic deformation in which the stored energy in the deformed grains is reduced by the removal or rearrangement the dislocations. The dislocation density is reduced through the cross-slip of screw dislocations and the climb of edge dislocations. Even though the stored energy is decreased during the dynamic recovery process, it continues to be introduced. This is the principal difference between dynamic recovery and static recovery. Previous studies suggest that the dynamic recovery process has a strong dependence on the elevated deformation temperature [49] and primarily takes place between 100°C and 200°C. The dislocation tangles were observed to disappear when aluminum was deformed at this temperature range. After deformation at 250°C, the dislocation tangles are nearly gone [48]. Although the dislocation density is reduced during both dynamic recovery and static recovery, the dynamic recovery proceeds at a rate controlled by the applied stress or strain rate, while static recovery proceeds at a declining rate which is affected by the internal stresses to cause heterogeneity [50].

The dynamic recrystallization process is caused by the thermo-mechanical process as new grains nucleate and growth will take place during the plastic deformation. Geometric dynamic recrystallization (GDRX), subgrain rotation recrystallization, and discontinuous dynamic recrystallization are three forms of dynamic recrystallization. Discontinuous dynamic recrystallization occurs during the transition of softening mechanism from strain-hardening and dynamic recovery to dynamic recrystallization. Low stacking fault energy metals undergo discontinuous dynamic recrystallization, such as magnesium alloys and beta titanium alloys. Aluminum alloys are high stacking fault energy metals which undergo continuous dynamic recrystallization during high temperature deformation [53]. As a type of continuous dynamic recrystallization, the mechanism of geometric dynamic recrystallization initiates when grains are increasingly flattened until the boundaries on each side are separated by only a small distance. At

that point, the serrated edges of the grain boundaries will come into contact to form new grains [51]. Subgrain rotation recrystallization is represented as the initially low-angle sub-grain boundary rotations; the rotations will cause the crystal lattices across the boundary mismatch to be regarded as grain boundaries [52]. Many previous studies investigated the dynamic recrystallization behavior. Continuous dynamic recrystallization (DRX) which occurs during hot deformation at 450°C has been observed in 7075 aluminum alloys. Subgrain growth and subgrain coalescence rather than particle-simulated nucleation make the primary contribution to the nucleation of new grains [85]. The effect of strain rate and particle size on dynamic recrystallization of Al5083 has been studied [46]. Related research also suggests that the strain required for the same DRX volume fraction increases with decreasing deformation temperature for a fixed strain rate. In contrast, it increases with increasing strain rate for a fixed temperature [86]. Physical models used to predict recrystallization kinetics, recrystallized grain sizes, and recrystallization textures were also developed for aluminum alloys [54].

Dynamic precipitation usually occurs during the thermo-mechanical process for the age-hardening alloys, such as Al-Mg-Si Alloys. The strengthening effect of dynamic precipitation during plastic deformation for aluminum alloys of was investigated extensively. Roven et al. [59] studied the precipitation behavior of Al-Mg-Si alloys during severe plastic deformation and discussed the interaction between precipitates and dislocations. Cabibbo et al. [60] also studied the strengthening mechanism of the second-phase particles during severe plastic deformation for the 6082 Al-Mg-Si alloy. The second-phase Si particles were found to dissolve progressively and become less effective with increasing deformation. Second-phase Mg_2Si particles are cut and fragmented by the dislocations and only have limited contribution to material strength. Fine Mg_2Si precipitates were found to distribute in hot deformed AA 6015 alloy at low temperatures; for higher heating temperature above 400°C, the Mg_2Si precipitates coarsen with temperature. The effect of Mg_2Si precipitate size on dynamic restoration was analyzed [61]. Dynamic precipitation of Mg_2Si during hot extrusion and its impact on the microstructures and mechanical properties of Al-Mg-Si-V alloys were also investigated [62]. Dynamic precipitation of coarse Mg_2Si particle was found to cause a considerable coarsening effect on recrystallized grains due to reduction of the solute drag on the grain boundary motion, consequently resulting in a considerable decrease in material strength. Dynamic precipitation and dynamic recrystallization in 6061 aluminum alloy during compressive hot deformation were studied by Fan et al. [47].

Strain rate sensitivity and different temperature effects on dynamic precipitation and recrystallization were discussed. They found that dynamic precipitation has strong dependence on temperature, with more precipitates appearing at 400°C but none at 500°C. Geometry dynamic recrystallization takes place concurrently and has stronger grain refinement effect at high temperature than at low temperature.

These previous studies have summarized the stress influence on the microstructural damage during plastic deformation. However, limited research has been done in examining the influence of temperature and creep strain on the grain structure growth and precipitation evolution for Al5083 and Al6061. The resulting residual strength reduction caused by grain structure and precipitation change has been fully investigated yet. In this work, dynamic grain structure and precipitate evolution at various temperatures are studied to evaluate the post-fire performance of Al5083 and Al6061.

4.2 Experimental

4.2.1 Materials and Test Method

The marine-grade aluminum alloys AA5083-H116 and AA6061-T651 were selected to perform to study the grain structure and precipitate evolution. The nominal chemical compositions of both alloys are shown in Table 1. Aluminum 5083-H116 is a work-hardened alloy with magnesium as its major alloying element. Grain strengthening is the mechanism from which material gains its strength. During thermal exposure the grain recrystallization also causes major strength degradation to Al5083. Aluminum 6061-T651 is a precipitation hardened aluminum alloy with magnesium and silicon as major alloying elements; the precipitation evolves during heat treatment resulting in significant residual strength reduction. Thus, it is necessary to examine the grain structure and precipitation evolution during thermo-mechanical deformation and estimate the consequent residual strength degradation.

Both materials were supplied by Alcoa in form of 6.35mm thick sheets. The test sample geometry was the dog-bone sample selected based on the ASTM standard E21-09, as shown in Fig. 13. All dog-bone samples for each alloy were machined from the same aluminum sheet to keep uniform material properties. Specimens were machined by Tormach PCNC 1100 Mill, with a gage length of 190.5 mm and a uniform width of 12.7mm.

Test conducted before microstructure characterization was the same thermo-mechanical test discussed in section 3.2.2. Based on the microstructure changes during pure thermal exposure [5], the following temperatures were selected to perform the thermo-mechanical tests and to study the influence of stress on grain structure and precipitate evolution:

- 200°C as the subgrain coarsening and initial strength degradation temperature for Al5083
- 300°C as the initial recrystallization temperature for Al5083 and precipitates transformation from β″ to β′ phase for Al6061
- 400°C as the complete recrystallization temperature for Al5083 and equilibrium β phase formation for Al6061.

During the thermo-mechanical tests, samples were heated to the specified temperature at a constant heating rate. Since Al6061 is quite sensitive to the heating rate and the precipitation evolution sequence in 20°C/min was well studied [22], 20°C/min heating rate was selected in the Al6061 thermo-mechanical tests. Al5083 has partially recrystallized and completely recrystallized grain structure at 300°C and 400°C respectively, which is not that sensitive to heating rate. Thus 50°C/min heating rate is applied in Al5083 creep tests. The desired sample temperature is provided by an Ameritherm 5060LI Induction heater, which is controlled by a Watlow PID controller using temperatures measured by a Micro-Epsilon optical infrared pyrometer as the feedback signal, as shown in Fig. 14. Once the sample reached the target temperature, a pre-selected stress was applied by an MTS 880 Load Frame, which is controlled by a MTS Micro Profiler, as shown in Fig. 15. Samples were then held at constant temperature and engineering stress for a period of time. During this time, strain was measured over a 22mm gage length using a Fiedler Optoelektronik GmbH laser extensometer, as shown in Fig. 19. Real time load, stroke, strain and exposure time data during the creep tests are all recorded by LabView program. Tests were interrupted after various exposure times to investigate the stress effect on the grains and precipitates at multiple engineering creep strains.

Non-stressed thermal exposure tests were also performed to provide the background information of thermally-induced damage on grains and precipitates. Samples were heated at the same heating rate and then held at same designed temperature for the same exposure time as the corresponding thermo-mechanical creep test. The only strain experienced by these samples was

the thermal expansion (~1%) which was recovered after the samples cooled down to ambient temperature.

4.2.2 Grain Structure Examination

In a procedure similar to that used to observe the cavitation development, damaged sections with dimensions of approximately 6 mm were cut from the severely necked regions to examine grain structures and precipitates at each creep stage. The sectioned samples were mounted and polished with SiC sandpaper, 3μm and 1μm diamond suspensions, and 0.5μm colloidal silica to produce a mirror surface. After that different etching methods were applied to observe the grain structure evolution in the deformed samples.

The first etching method is the Poulton's Etch. This etchant for Al5083 consists of 50 mL of Poulton's reagent (12mL HCl, 6mL HNO3, 1mL HF (48%), 1mL H2O), 50mL of HNO3, and 12g of chromic acid (chromium oxide) per 40mL of H2O. Al5083 samples were then immersed in etchant for about 30 seconds after etchant was prepared and held for 4 hours. For Al6061, 25ml of HNO3 was used instead of 50ml HNO3 in the Al5083 etchant. Al6061 samples were immersed in the etchant for 20 seconds immediately after the etchant was prepared. The Poulton's Etch can provide clear view on the grain structures. However, hydrofluoric acid is used in this etching method and introduces safety concerns to the lab because hydrofluoric acid is a contact-poison with the potential for deep, initially painless burns and ensuing tissue death. As a result, it is extreme dangerous and must be used with great caution. In addition, with the use of Poulton's Etch it is hard to prevent over etched on aluminum samples and with many pits on the grains.

To prevent injury from the use of hydrofluoric acid and to obtain better observations of the grain structure, a second etching method was applied: anodizing. Anodizing is an electrolytic etching procedure which works by depositing a film on the specimen surface. Grain structures can be then revealed under cross polarized light. Anodizing is the most widely etching technique for aluminum and its alloys and successfully reveals their grain structures. Barker's solution consisting of 5 mL HBF4 (48%) in 200 mL water is applied in this electrolytic etching method. During the etching, stainless steel is used as the cathode and aluminum is the anode in a Buehler ElectroMet Etcher, as shown in Fig. 31a. Al5083 samples were anodized for 90 seconds at 0.2

mA/cm^2. Al6061 samples required longer anodizing times of approximately 5 minutes. Samples etched by Barker's solution also showed clear grain boundaries except for some grains which could not be fully revealed. However, the use of Barker's Etch provided a more convenient and safer method to etch aluminum alloys and reveal clear grain boundaries on the etched microstructure.

After etching, samples were cleaned by distilled water and ethanol, then dried in nitrogen. Grain structures in all three material surfaces (rolling, transverse and normal surfaces) were examined using Zeiss Axiovert.A1 MAT optical microscope under cross polarized light, as shown in Fig. 31b. Grain length, width, and thickness were then estimated by line intersection method. Grain aspect ratio was calculated as grain length divided by grain width on the rolling surface.

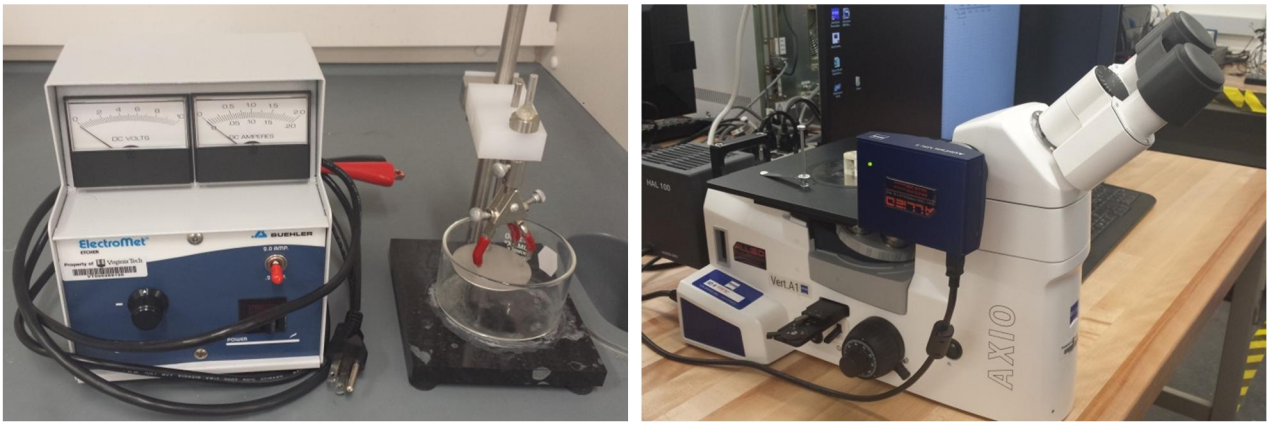

(a) (b)

Fig. 31 (a) Buehler ElectroMet Etcher (b) Zeiss Axiovert.A1 MAT Optical Microscope

4.3 AA5083-H116 Grain Structure Evolution

During plastic deformation, temperature, time, and stress all affect the grain structure evolution. To study the stress influence on grain structure, both grain structures from unstressed thermal exposure and strained grain structures were examined to investigate the stress-induced damage. Temperature is one of the major factors to cause grain structure change, thus various temperatures are selected to examine the different features of grain structure evolution in Al5083: 200°C as the subgrain coarsening and initial strength degradation temperature, 300°C as the initial recrystallization temperature, and 400°C as the complete recrystallization temperature.

4.3.1 200°C Exposure

The grain structures for both unstressed thermally exposed and strained samples treated at 200°C are shown in Fig. 32. Large pancake grains orientation parallel to rolling direction (horizontal direction in Fig. 32) are displayed in the as-received microstructure. Grain structures in the 200°C heat treated sample exhibit similar morphology with the as-received state. The extension of exposure time up to 2000s does not cause any change in grain structure, as shown in Fig. 32b and c. These observations verify that a 200°C exposure temperature is too low to cause any grain structure change. Only dislocation recovery occurs in this temperature range.

Grain structure in the mechanically strained sample also maintains a similar size and shape with the unstrained sample, a result which is due to the low ductility of aluminum alloys at 200°C. Samples which are thermo-mechanically deformed at 200°C can only reach a 15% creep strain before fracture. Thus the slightly strained gains do not exhibit obvious changes in the grain aspect ratio.

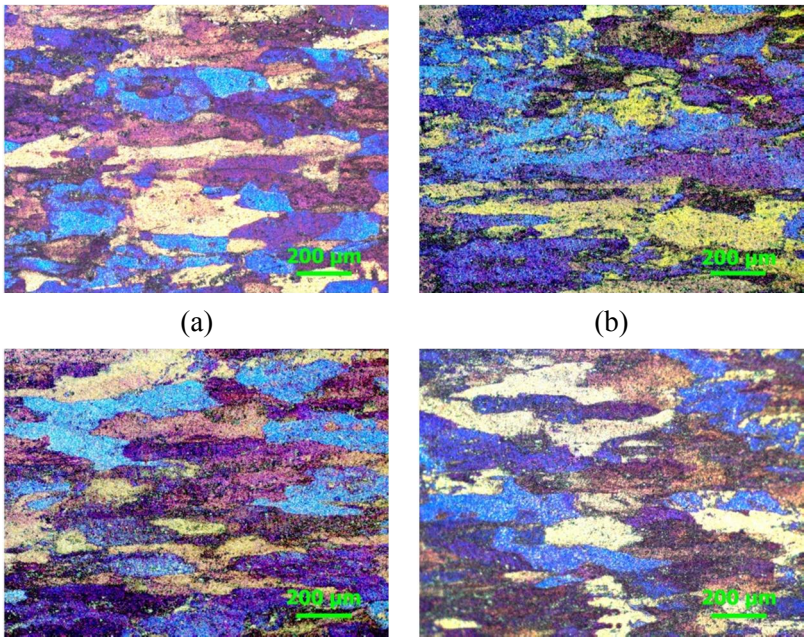

(a) (b)

(c) (d)

Fig. 32 Al5083 grain structure evolution at 200°C (a) as-received, (b) 200°C, 0MPa, 0s, (c) 200°C, 0MPa, 2000s and (d) 200°C, 140MPa, 2000s, ε=15%

4.3.2 300°C Exposure

Samples heat treated at 300°C display complete different features of grain structure evolution compared to the 200°C treated ones. Fig. 33 shows the grain structure evolution of samples thermal exposed to 300°C under 50°C/min heating rate and held for different times. As discussed in previous research, grain recrystallization initiates at temperatures between 280°C and 320°C depending on the heating rate [5]. A temperature of 300°C is within the initial recrystallization temperature range. However, the grain structure of sample that just reaches 300°C does not displayed obvious recrystallization, as show in Fig. 33b. As samples are held at the 300°C temperature for longer times, more thermal energy is absorbed and the initial large pancake grain structure starts to recrystallize. Fig. 33c shows the partially recrystallized grain structure for samples held at 300°C for 500s. Some small equiaxed grains appear at the edges of the original larger pancake grains. After exposure at 300°C for 1000s, the recrystallization process is nearly completed; the pancake grain structure has evolved into the equiaxed grain structure.

The strained samples show a different recrystallization process than those with pure thermal exposure, as show in Fig. 34. As the sample strain increases with the increase of exposure time, the grain structure appears to be stretched longer and thinner along the horizontal direction (direction of rolling and loading). This stretching effect is not that obvious in the low strain samples. The grains in the 13% to 30% creep strain samples in Fig. 34a-c are only slightly stretched compared to the higher strain (100%) sample in Fig. 34d. The grains for the 100% strain sample have been stretched into extreme thin and long shape. The grain aspect ratio is significantly increased from the as-received grains in Fig. 33a. The original grain boundaries become serrated. In some locations, the serrated grain boundaries are pinched off to form new equiaxed grains. This phenomenon can be addressed as the geometric dynamic recrystallization during the plastic deformation. The mechanism of geometric dynamic recrystallization initiates when grains are increasingly flattened until the boundaries on each side are separated by only a small distance; the serrated edges of the grain boundaries will come into contact to form new grains [51].

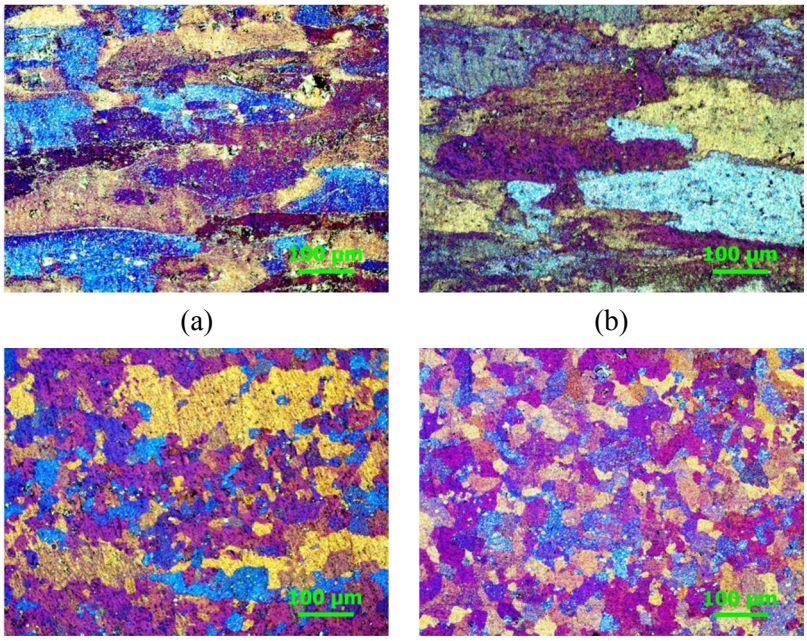

(a) (b)

(c) (d)

Fig. 33 Al5083 grain structure evolution at 300°C (a) as-received, (b) 300°C, 0MPa, 0s, (c)300°C, 0MPa, 500s and (d) 300°C, 0MPa, 1000s

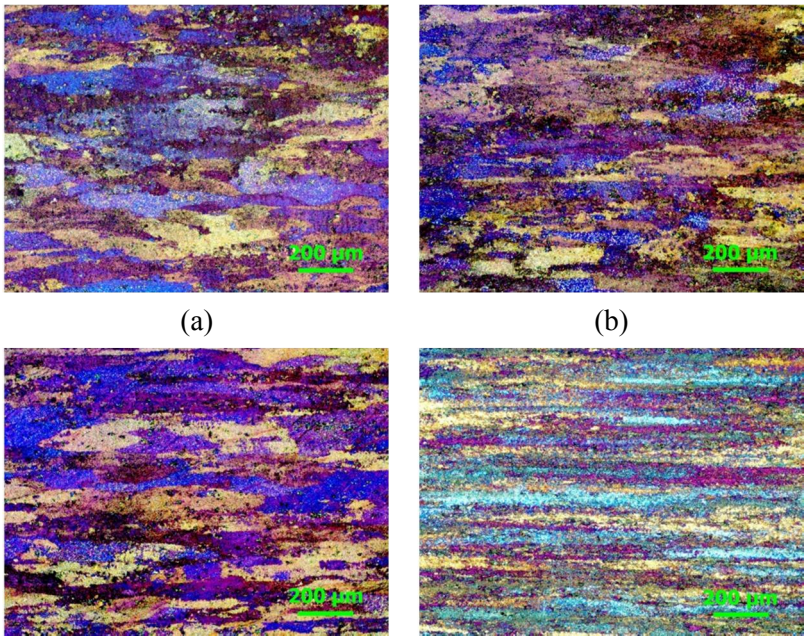

(a) (b)

(c) (d)

Fig. 34 Al5083 grain structure evolution at 300°C, 50MPa (a) 500s, ε=13%, (b) 1000s, ε=20%, (c) 1500s, ε=30% and (d) 2000s, ε=100%

4.3.3 400°C Exposure

As mentioned above, grain recrystallization occurs in the temperature range between 280°C and 380°C depending on the heating rate. Thus, 400°C is a temperature at which the grain structure has been fully recrystallized. The grain structure evolution at 400°C displays distinct features compared to the lower exposure temperature. Fig. 35 shows the unstressed grain structure evolution at 400°C. The as-received pancake grain structure has been fully developed into equiaxed grain structure after sample heating to 400°C, as show in Fig. 35b. The average grain size is significantly reduced from 80 μm to 46 μm. At this time the grain structure has reached the stable state and the Gibbs free energy is minimum in the material. Thus, even as the exposure duration is increased, the stable equiaxed grain structure remains the unchanged; no further changes are observed in the grain structure held at 400°C for 2000s in Fig. 35c.

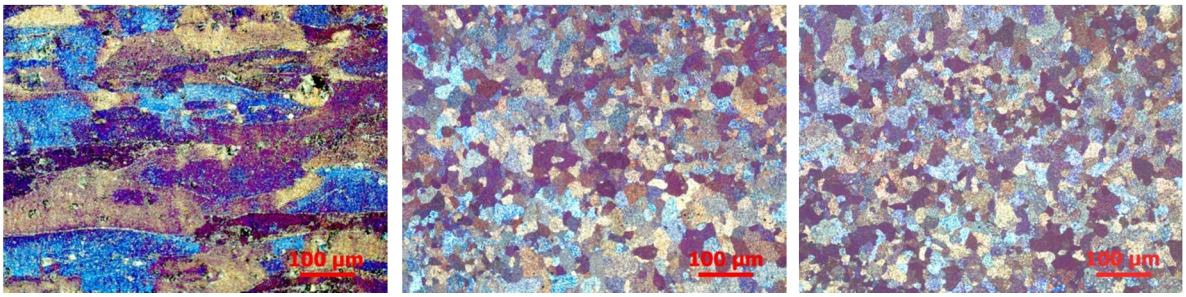

(a) (b) (c)

Fig. 35 Al5083 grain structure evolution at 400°C (a) as-received, (b) 400°C, 0s, (c)400°C, 2000s

After stress is applied to the sample at 400°C, large amounts of strain will be generated and localized in the sample center. The cross sectional area reduction will increase with the accumulation of plastic strain. Since stress has not been applied until after the sample reaches 400°C and static grain recrystallization is competed at that time, the grain structure evolution in the strained sample will progress from the initial equiaxed grain structure at 400°C in Fig. 36b. After stress is applied, material begins to creep along the loading direction; grains will be deformed concurrently to accommodate the creep strain as shown in Fig. 36c-f.

With the increase of plastic strain/cross sectional area reduction, the grains are observed to be stretched along the horizontal direction (direction of rolling and loading) from the equiaxed structure to thin, long grain structure. The quantified data in Fig. 37a shows that grain aspect ratio increases with the accumulation of reduction area. The grain aspect ratio is 0.91 at the state

initially heated to 400°C, gradually increases to 2.9 at 63.8% reduction in area, and then significantly increases to 7.5 at 84.3% reduction in area, indicating that the grains are highly elongated along the tensile direction to accommodate the large plastic deformation during creep. For the highly strained sample in Fig. 36f, the serrated grain boundaries come into contact with each other in some locations to cause new grain nucleation during this dynamic recrystallization process. On the other hand, cavitation is also developed with the accumulation of creep strain. As shown in Fig. 37b, the cavity volume fraction slowly grows to 1% at 63.8% reduction in area, but drastically increases to 5% at 84.3% reduction in area. The two phenomena show similar evolution trends: slowly increasing at low strain level/reduction in area and rapidly increasing after significant plastic strain accumulation.

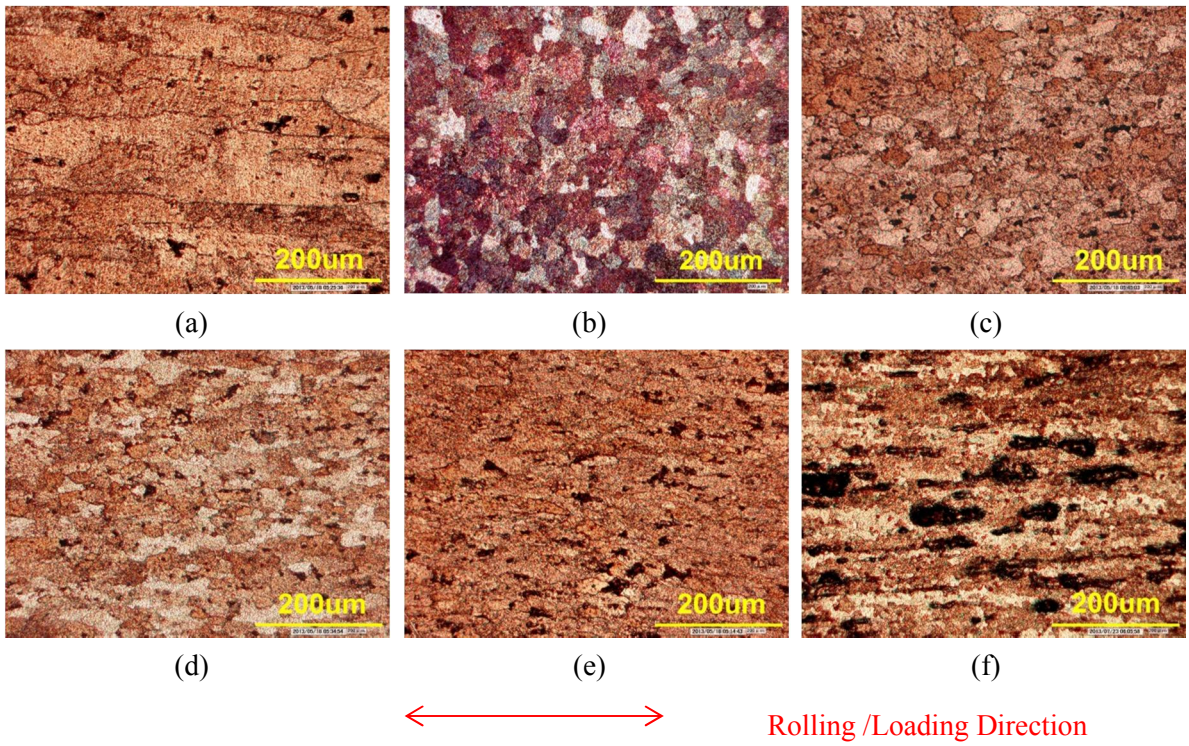

Fig. 36 Al5083 grain structures (560x, rolling surface) of (a) as-received sample (b) 400ºC, 0MPa, ε = 0%, and (c)-(f) 400ºC, 17MPa creep samples, ε = 50% , 80%, 100% and 143%

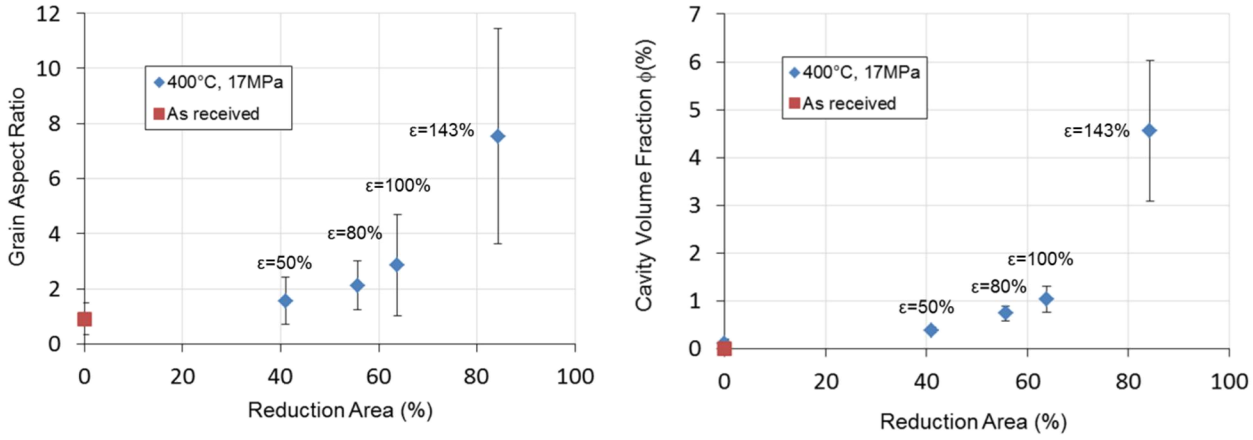

(a) (b)

Fig. 37 (a) Al5083 grain aspect ratio(calculated based on rolling surface grains) (b) Al5083 cavity volume fraction for 400°C, 17MPa creep samples

4.4 AA6061-T651 Grain Structure and Precipitate Evolution

The stress influence on microstructural damage in Al6061 was also examined. Since Al6061 is strengthened by precipitate hardening, dynamic precipitation is another important phenomenon in additional to the dynamic grain structure evolution during plastic deformation. To separate the stress effect on precipitation and grain structure, unstressed thermally exposed samples are also examined to provide background knowledge of thermally-induced microstructural damage. The same temperatures investigated with the Al5083 have been selected to examine the grain structure in Al6061: 200°C as the initial strength degradation temperature, 300°C as the temperature at which precipitates transformed from the β″ to β′ phase, and 400°C as the equilibrium β phase formation temperature.

4.4.1 200°C Exposure

Grain structures for samples exposed at 200°C are displayed in Fig. 38. The microstructure of the as-received sample prior to thermal and mechanical treatments is also illustrated. Since Al6061 is manufactured by hot extrusion, the grains have not been deformed during the manufacturing process. Thus, the as-received grains exhibit large pancake shapes with no specified orientation. A similar grain morphology are displayed in the microstructures after 200°C heat treatment in Fig. 38b and c, which also verifies that the 200°C exposure does not have any effect on grain

structure, even for long time exposure. The 200°C exposure temperature is also too low to cause precipitate transformation.

During thermo-mechanical tests, the sample begins to creep and the plastic strain will accumulate with exposure time. However, only a small increase in the ductility of Al6061 is observed under 200°C heat treatment. Less than 15% of creep strain can be achieved before sample fracture. Thus almost no change can be observed in the 200°C strained grain structure before sample failure, as shown in Fig. 38d.

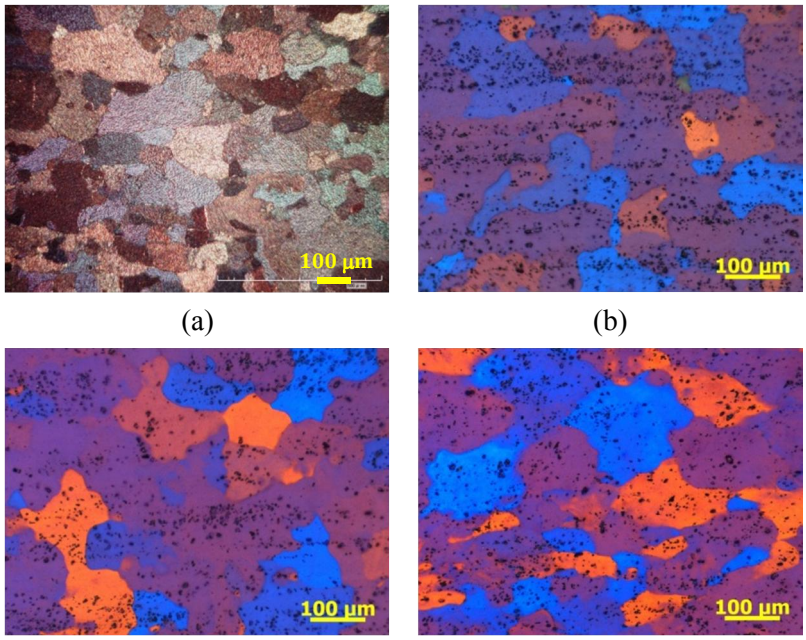

(a) (b)

(c) (d)

Fig. 38 Al6061 grain structure evolution at 200°C (a) as received, (b) 200°C, 0MPa, 0s, (c)200°C, 0MPa, 1400s and (d) 200°C, 220MPa, 1400s, ε=12%

4.4.2 300°C Exposure

Fig. 39 illustrates the grain structure evolution for both unstressed and strained samples exposed at 300°C. Reference pancake grain structures are shown in the as-received sample. Similar pancake grain structures are displayed in the 300°C heat-treated samples. Even as the exposure duration is increased, the grain morphology and size still appear similar to the as-received sample, as shown in Fig. 39b and c. Thus 300°C heat treatment will not cause any change to the grain structure of Al6061.

Sample tested at the 300°C thermo-mechanical condition was stopped just before failure to examine the damaged grain structure. Appoximately 19% creep strain was developed before sample failure at 300°C creep condition. The microstructure displays slightly stretched grain structures corresponding to the low creep strain. Grains are observed to be elongated in a small amount along the horizontal direction (direction of rolling and loading) in Fig. 39d. The increase in grain aspect ratio in the 300°C strained sample is also small due to the limitation of low creep strain before creep failure at 300°C.

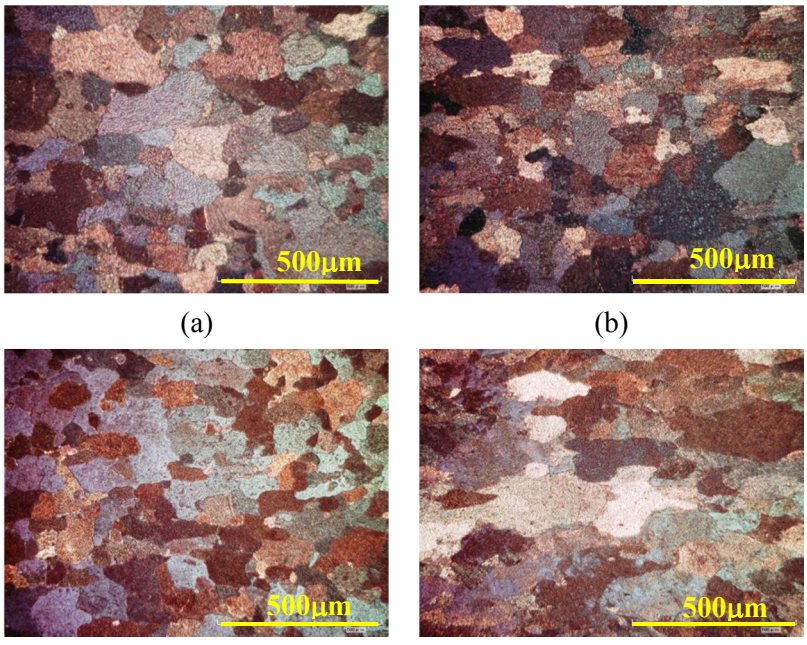

(a) (b)

(c) (d)

Fig. 39 Al6061 grain structure evolution at 300°C (a) as received, (b) 300°C, 0s, (c)300°C, 4000s and (d) 300°C, 80MPa, 4000s, ε=19%

Fig. 40 shows both the unstressed and strained microstructures for samples tested at 300°C. 300°C is within the temperature range in which precipitates have transformed from the metastable β″ phase to β′ phase. The metastable β″ phase growth into β′ phase is associated with the transition in the precipitate/dislocation strengthening mechanism. Since precipitate growth from the β″ to β′ phase occurs from approximately 250 - 300°C, and the β′ precipitation peak temperature at ~310°C, the β′ phase will be the primary precipitates at 300°C. Although the β' phase precipitates are larger than the fine β″ precipitates, the size is still in nanometer scale and not easy to be observed from the SEM images. Thus, no precipitates can be observed from the SEM images for the 300°C heat treated samples in Fig. 40b and c. The strained sample in Fig.

40d does not display any precipitation either. Only some cavities are shown on the microstructure of strained sample.

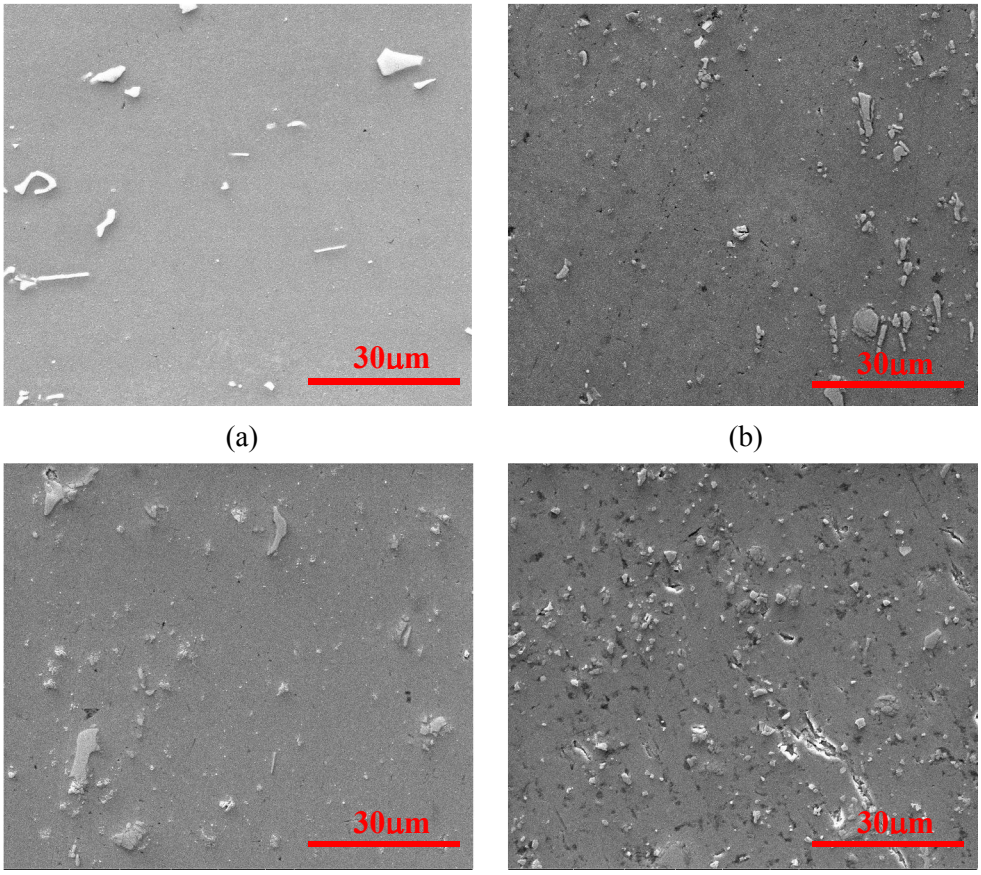

Fig. 40 Al6061 microstructures (SEM, 2800x, Normal surface) (a) as-received sample (b) 300ºC, 0MPa, 0s, (c) 300ºC, 0MPa, 4000s, and (c) 300ºC, 80MPa, 4000s, ε = 19%

4.4.3 400°C Exposure

Samples exposed to the 400°C condition exhibit similar grain structure evolution features with 300°C exposure conditions for both unstressed and strained samples. Samples heated to 400°C display similar pancake grain structures with the as received state; grain morphology and size still appear the same even after exposure duration is increased, as shown Fig. 41b and c. Because the primary strengthening mechanism in Al6061 is the precipitation phase evolution during the thermal exposure; the grain structure will remain unchanged during the heat treating process. Both the as-received and the 400°C, 0s exposure sample exhibit similar smooth grain surfaces. However, the grain surface in the 400°C, 2900s exposure sample appears to be more textured

than the 400°C, 0s exposure one. This observation indicates that extend the exposure duration at 400°C may cause some changes to the microstructure.

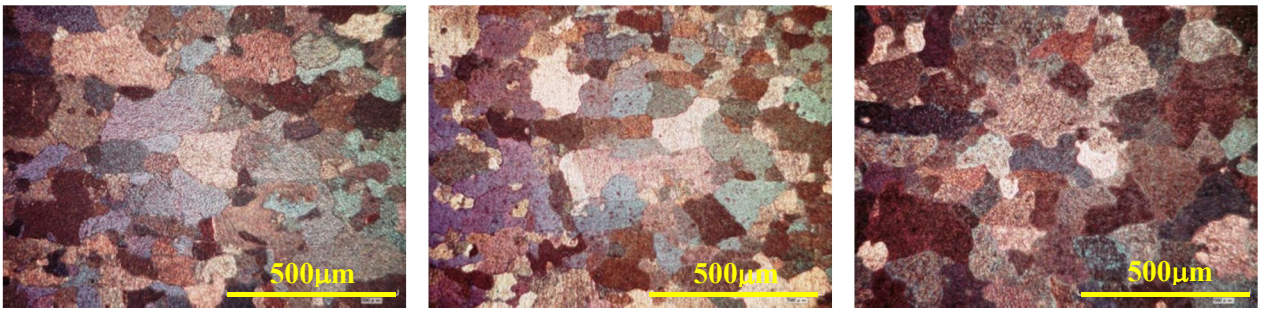

(a) (b) (c)

Fig. 41 Al6061 grain structure evolution at 400°C (a) as received, (b) 400°C, 0MPa, 0s, (c)400°C, 0MPa, 2900s and (d) 400°C, 20MPa, 2900s, ε=58%

Thermo-mechanical tests conducted at 400°C introduced more plastic strain to Al6061 sample than the lower temperatures. The strain localizes disproportionately in the sample center. About 60% creep strain and 75% reduction in area have been developed in Al6061 samples before the 400°C creep failure occurs. Grain structures for both unstressed thermally exposed samples and those strained at 400°C are displayed in Fig. 42. Grain structure evolution in the strained samples progresses from the initial state treated at 400°C in Fig. 42b, which appears similar with the as-received grains. The strained samples display stretched grain structures corresponding to the creep strain levels. Grains are gradually elongated along the horizontal direction (direction of rolling and loading) with the increase of creep strain.

The grain aspect ratio of the 400°C strained sample increases with the accumulation of reduced area as shown in Fig. 43. The grain aspect ratio is 1.34 at the as-received state; it is slightly increased to 2.2 at 33.4% reduction in area. With the strain localization at the sample center, grains are elongated with the orientation along the tensile direction. At the state impending material failure, the sample cross sectional area has reduced by 74.5%; the grain aspect ratio is greatly increased to 6.35. As shown in Fig. 42f, grains are highly stretched into a thin and long texture to accommodate the large plastic deformation, indicating the initiation of geometrical dynamic recrystallization. For further grain elongation, the grain width will be reduced and grain

boundaries will become serrated. New grains will nucleate when the serrated grain boundaries come into contact with each other in some locations.

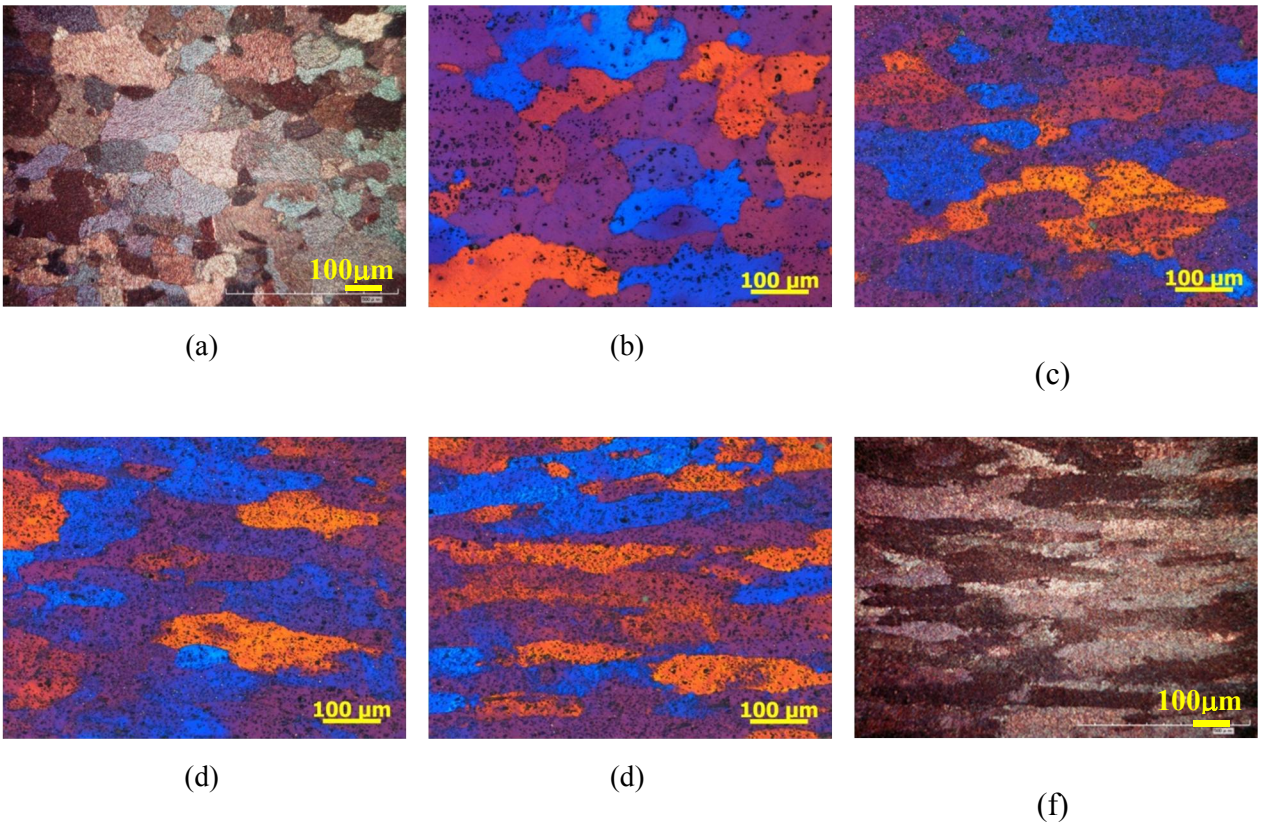

Fig. 42 Al6061 grain structures (200x, rolling surface) of (a) as-received sample (b) 400ºC, 0MPa, ε = 0%, and (c)-(f) 400ºC, 20MPa creep samples, ε = 25% , 36%, 47% and 58%

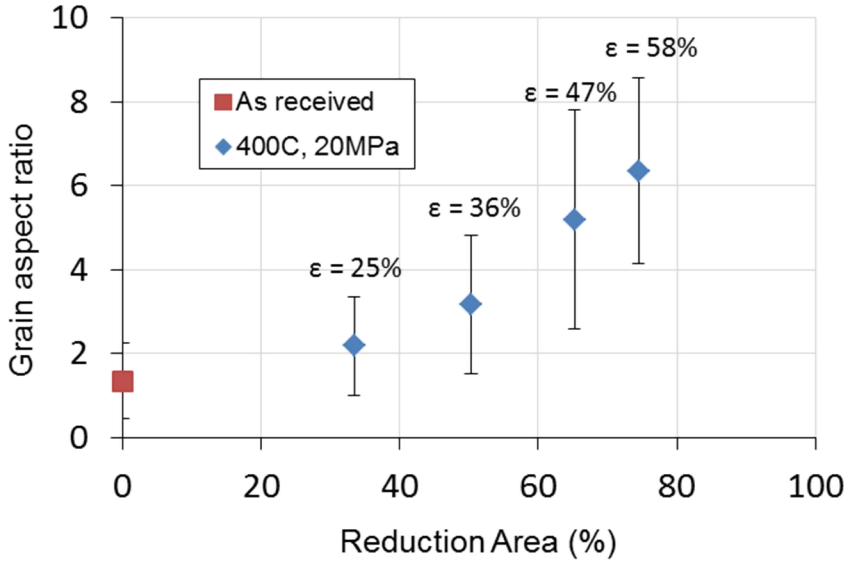

Fig. 43 Al5083 grain aspect ratio (calculated based on rolling surface grains) for 400°C, 20MPa creep samples

In addition to the dynamic grain structure evolution, dynamic precipitation is another feature of Al6061 during the thermo-mechanical process. As mentioned above, the β′ phase dissolution peak is between 350°C and 420°C and the β precipitation peak is identified at ~460°C. 400°C is within the temperature range in which β′ phase precipitation dissolves and the β phase formation. The β phase is relatively large and the only precipitation phase which can be observed from the SEM image. As seen in Fig. 44b, only small amount of β phase is displayed in the microstructure of 400°C exposed sample. With increasing heating duration, more precipitates are shown in the microstructure in Fig. 44c. These precipitates are identified as the needle-shape Si precipitates and the plate-shape precipitates contain Mg and Si, as shown in Fig. 45. The plate-shape precipitates contain Mg and Si might be the equilibrium β phase (Mg_2Si), which has limited contribution to the material strength [20]. Similar precipitates are observed in the strained sample in Fig. 44d. However, for the same heating duration, the precipitate volume fraction in the strained sample are smaller than the unstressed one in Fig. 44c. Less precipitation in the strained sample might be caused by some alloying elements dissolving back into the matrix during the dynamic precipitation process [47]. The strengthening mechanism of the second-phase particles in Al-Mg-Si alloy during severe plastic deformation was studied by Cabibbo et al. [60]. The second-phase Si particles (rod shape) were found to dissolve progressively and become less effective with the increasing deformation. Second-phase Mg_2Si particles (plate shape) are cut and fragmented by the dislocations during deformation, only have limited contribution to material strength.

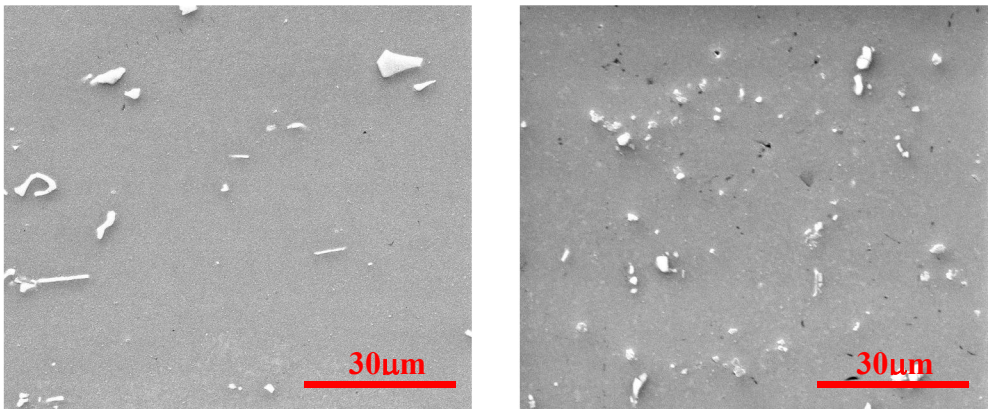

(a) (b)

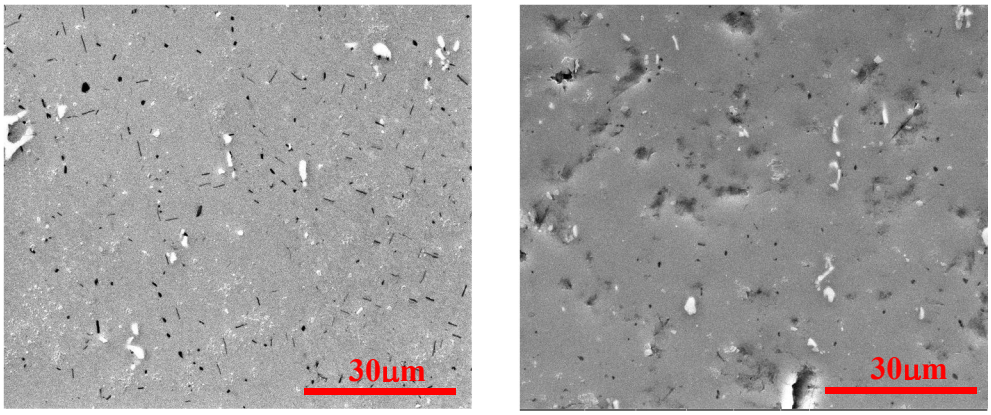

(c) (d)

Fig. 44 Al6061 microstructures (SEM, 2800x, Normal surface) (a) as-received sample (b) 400ºC, 0MPa, 0s, (c) 400ºC, 0MPa, 2900s, and (c) 400ºC, 20MPa, 2900s, ε = 58%

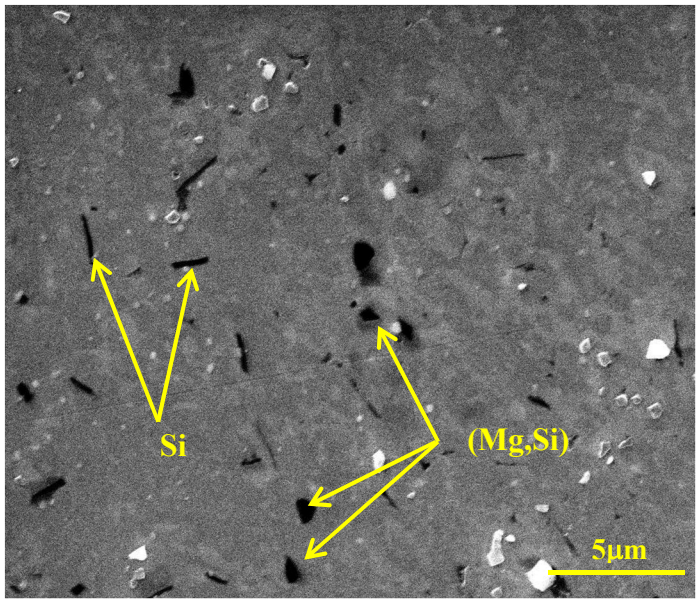

Fig. 45 Precipitates in 400°C, 2900s exposure sample

4.5 Creep Mechanism Difference in Al5083 & Al6061

The above study exhibits different dynamic microstructure evolution features for both alloys during creep process: Al5083 displays large crack-like cavities, significant grain elongation, and dynamic recrystallization before creep failure while Al6061 shows small spherical cavities and greatly elongated grains before sample fracture. To study the difference in creep mechanisms, the sample true strain in the localized neck region is calculated from the reduced cross sectional area and compared with the longitudinal grain strain along the tensile direction. Results for both alloys deformed at 400°C are listed in Fig. 46.

At the low creep strain levels, the longitudinal grain strain for Al5083 exhibits similar value with true strain in the neck region. However, at higher creep strain levels, the longitudinal grain strains appear smaller than the true strain in the localized neck region. The strain difference increases progressively with the accumulation of creep strain. At the just-before-fracture state, only about 60% of the sample true strain is contributed by the longitudinal grain strain. This observation reveals that grain deformation in Al5083 can accommodate the small creep strains, but shows high incompatibility with larger creep strains. Grain boundary sliding will take place when the grain deformation cannot accommodate the large plastic deformation and will contribute to the creep strain. More than 30% of true strain is contributed by grain boundary sliding before Al5083 creep failure. The large amount of grain boundary sliding also promotes significant cavity growth during plastic deformation. A previous study indicates that cavities are observed to grow in the plane of the sliding boundary during the continuous plastic deformation under thermo-mechanical condition [39]. Thus the spherical shape cavities at the low strain level will be developed into large cylindrical cavities along tensile direction as a result of grain boundary sliding.

In contrast, Al6061 data displays distinct features during creep process. The longitudinal grain strain shows coincident values with the true strain in the sample localized neck region for both low and high creep strain levels, indicating that the grain deformation in Al6061 can accommodate the sample true strain, even during large plastic deformation. Thus, sample creep strain is primarily composed of grain elongation with almost no grain boundary sliding contribution until sample approaches creep rupture. Since no grain boundary sliding occurs during Al6061 creep process, only limited creep strain (about 60% strain over 22mm gage length) has been developed before material failure, which is much smaller than the large creep strain induced by grain boundary sliding in Al5083. The cavities developed in Al6061 sample also remain small spherical shape until sample failure.

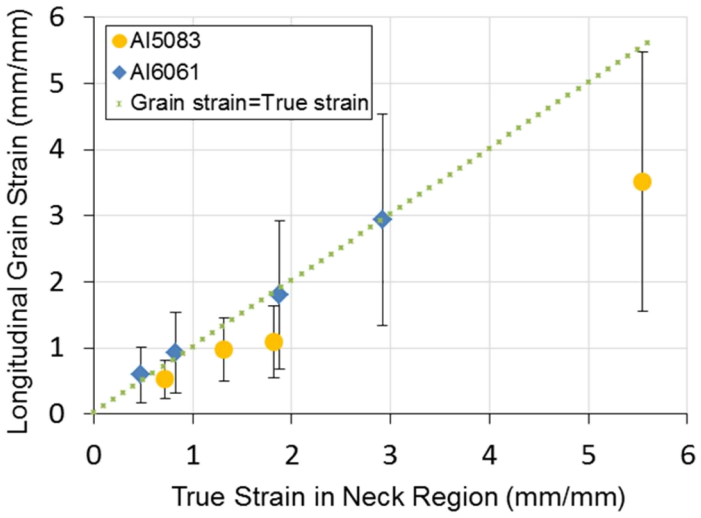

Fig. 46 Relation between longitude grain strain and true strain in the neck region for Al5083 and Al6061

4.5 Conclusion

The stress-induced damage on the grain structure and precipitation evolution of Al5083 and Al6061 are investigated in this chapter. Both unstressed thermally exposed states and mechanically strained states were examined to separate the stress-induced damage, which is manifested as dynamic recrystallization and dynamic precipitation. The stress-induced microstructural damages exhibit different mechanisms at different heat treatment temperatures for both alloys. The difference in creep mechanisms between Al5083 and Al6061 are also discussed.

Al5083 exhibits no obvious change in the strained grain structure before creep failure at 200°C due to the limitation of ductility at such a low temperature. However, geometrical dynamic recrystallization takes place at higher strain levels. Since static recrystallization has not occurred when the material reaches 300°C, the grains are stretched from the pancake structure to thin and long shape. Because static recrystallization has been fully completed after 400°C exposure, grains evolve from an equiaxed grain structure to a textured thin grain structures. The grain aspect ratio increases significantly and grain boundaries become serrated with the increase of plastic strain/reduction in area. New grains are observed to nucleate at some locations due to the contact of serrated grain boundaries during creep. However, the highly elongated grain still cannot accommodate the large creep strain at high creep strain levels. Grain boundary sliding

also takes place and makes great contribution to the sample true strain. Large cylindrical cavities along tensile direction are also developed as a result of grain boundary sliding at high creep strain levels.

Al6061 exhibits distinct features in grain structure evolution that contrast with those seen in Al5083. No obvious change takes place in the 200°C strained grain structure; a slight increase in grain aspect ratio is observed for the 300°C strained grain structure; the 400°C strained samples display progressively stretched grain structures corresponding to the creep strain levels. The relation between longitudinal grain strain and sample true strain in the localized neck region reveals the different mechanism in Al6061: grain deformation accommodates the creep strain until sample failure. Sample creep strains are primarily developed by the grain elongation; there is almost no grain boundary sliding contribution until sample approaches creep rupture. Thus the grain structure evolution and spherical cavities developed in Al6061 are limited to its low creep strain before sample failure. Dynamic precipitation also occurs during the thermo-mechanical process of Al6061. Larger second phase Si and Mg-Si rich precipitates are observed in the 400°C treated sample. These large precipitates are found to dissolve with the increase of plastic strain and have limited contribution to material strength.

CHAPTER 5 – Post-fire Residual Material Strength

5.1 Introduction

Aluminum alloys have increasing application in light weight load-bearing structures, such as bridge, vehicle, aircraft and ships. In these applications, fire safety is one of the most important concerns in the design of aluminum structures. During fire exposure, permanent change may take place in the microstructure and the post-fire residual strength will be degraded. Thus, it is urgent that we investigate the thermo-mechanically induced microstructural damage and evaluate the structural stability of the damaged aluminum structures after a fire.

Aluminum alloys exhibit strength degradation during elevated temperature exposure, which are summarized by Eurocode 9 and the American Society of Metals Handbook [11, 12]. During thermal exposure, internal microstructural damage may be accumulated in the aluminum structures which survive the fire and return to ambient conditions. The residual (post-fire) strength degradation due to thermally-induced damage for both Al5083 and Al6061 was investigated by Summers, et al. [5]. Both alloys' residual strength evolves from lightly affected to severely degraded due to different microstructure changes which occur with increasing thermal exposure.

The major contribution to the strength degradation in Al5083 is the grain structure change. The post-fire yield strength of Al5083 exhibits an initial decline from about 150°C - 280°C, then experiences a more severe decline from about 280°C - 380°C. More than a 50% reduction in yield strength was measured after prior exposure to 380°C. For further exposure above 380°C, almost no further strength reduction was observed up to 500°C. Static dislocation recovery and static grain recrystallization are the primary factors to cause of Al5083 strength degradation during stress-free thermal exposure. The initial strength reduction in Al5083 below 280°C is primarily caused by the subgrain coarsening during dislocation recovery [79] while the primary strength reduction between 280°C to 380°C is due to static grain recrystallization, which annihilates the subgrain structure.

In contrast, strength degradation in Al6061 is primarily caused by the evolution of precipitation during heat treatment. A relatively steady reduction with temperature in the Al6061 post-fire

residual yield strength occurs from 200°C - 450°C. After exposure to 500°C, an increase in yield strength is observed. Strength degradation during unstressed thermal exposure results from the corresponding changes in precipitation. The initiation of yield strength degradation is caused by the precipitate transformation from the metastable β″ to the β′ phase at temperatures between approximately 250 - 300°C. The β′ precipitate dissolution and the equilibrium β phase formation cause the significant reduction in residual yield strength after exposure to 400°C. When large β precipitates govern the strengthening phase, the residual yield strength will drop to its minimum value. This precipitate evolution in Al6061 has strong dependence on the heating rate. The peak temperature of β″, β′, and β-phase precipitation will increase with the increase of heating rate. As a result, the material's post-fire response will also be affected due to the change in precipitate peak temperature.

These previous studies only reported the influence of thermally-induced microstructural damage on residual material strength. It is possible that stress-induced microstructural damage will cause an additional effect on the post-fire response in the load-bearing aluminum structures. Cavity nucleation, growth, and coalescence take place associated with the plastic deformation in creep. As a result, the materials' residual yield and ultimate strength may be decreased due to the cavitation development. When cavity growth is driven by creep plasticity, micro cracks may be developed as the cavities coalescence. The interlinkage and propagation of micro cracks may then lead to fracture of the material [87].

In additional to cavitation, dynamic recovery, dynamic recrystallization and dynamic precipitation also occur during the thermo-mechanical process. Dynamic recovery will cause strength degradation by removal or rearrangement the dislocations in the deformed grains. Grains will be stretched along the tensile direction with the accumulation of plastic strain during geometric dynamic recrystallization. A strength model coupling grain orientation and grain size/shape effects has been developed [57]. In it, the yield strength was found to have a minimum value at the equiaxed grain structure, and then increase with increasing grain aspect ratio. Similar flow stress strengthening with the increase of hot deformation strain for other materials were also discussed [58]. Grain elongation is similar to the work hardening process; as the material is work hardened it becomes increasingly saturated with new dislocations. Thus dislocation density will increase with the increasing grain strain. Subgrain structures which are divided by dislocations

are also refined during the generation of new dislocations. Smaller subdomains will be developed and result in subgrain strengthening in the residual material strength [19].

However, before this study the influence of stress-induced microstructural damage on the residual (post-fire) mechanical properties for both Al5083 and Al6061 had not been fully investigated. We expect that cavitation will cause material strength degradation and that dynamic recrystallization will strengthen the material by subgrain structure refinement. The integrated effect caused by both cavitation development and dynamic recrystallization on residual (post-fire) material strength has not been fully understood yet.

In this work, residual material strengths for samples subjected to combined elevated temperature and mechanical loading were calculated based on deformed cross sectional area were analyzed to investigate the impact of stress-induced microstructural damage on the post-fire material response. The competing effects of strength degradation caused by cavitation and strengthening resulting from grain elongation were studied. To support structural designs, the residual material strengths for the same samples based on original cross sectional area were also calculated.

5.2 Experimental

5.2.1 Materials and Sample Geometry

Since thermo-mechanical tests had already been conducted for the marine-grade aluminum alloys AA5083-H116 and AA6061-T651 to investigate stress-induced microstructure damage, these two alloys were also selected to perform the post-fire tensile tests to evaluate their post-fire performance after fire damage. These two alloys are strengthened by different mechanism and manufactured from distinct processes; as a result, we expect the stress-induced microstructure damage will have different influences on the post-fire residual strength for both alloys. AA5083-H116 is a strain hardened alloy with high dislocation density in the deformed grains from manufacturing process to strengthen the material. AA6061-T651 is a precipitation hardened alloy with high precipitate density to act as obstacles to dislocation movement and strengthen the material. Thus, the grain deformation and precipitate evolution during the thermo-mechanical tests will cause different post-fire response for both alloys.

Both materials were supplied by Alcoa in the form of 6.35mm sheets. Same dog-bone sample geometry is selected based on the ASTM standard E21-09. Specimens were also machined by Tormach PCNC 1100 Mill to be 304.8mm long dog-bones with 190.5 mm of gage length, and uniform width and thickness for 12.7 mm and 6.35mm, respectively. Thermo-mechanical test is conducted prior to the post-fire tensile test to introduce creep damage. Subsequently, residual mechanical properties of the damaged sample were determined from the post-fire tensile tests.

5.2.2 Post-Fire Tensile Tests

The thermo-mechanical tests were interrupted at multiple creep strains to examine the stress-induced damage. As shown in Fig. 47, duplicate samples with the same creep damage used for the microstructural examination are prepared for conducting the post-fire tensile test to measure the residual mechanical properties.

Fig. 47 Post-fire test samples with creep damage in the center

All uniaxial tensile tests were conducted after the damaged sample cooled to the ambient temperature. Post-fire tensile tests were conducted in an MTS 880 Test Frame equipped with a 10 kN load cell. The test procedure are programed and controlled by a MTS 458.91 Micro Profiler. Hydraulic grips in the load frame provide constant grip force to both ends of the dog bone sample. A uniaxial tensile load was applied until sample failure. Tests were performed under displacement control at a strain rate of 0.2 mm/s. Sample strain was measured over the localized neck region by a MTS 634.11E-54 type extensometer with 1 inch gage length and 50% calibrated range. A Vishay 2310 Signal Conditioning Amplifier was used to provide the excitation voltage for the strain signal. Data acquisition was performed through a LabView program. The real time load, stroke, strain, and time data during the post-fire tensile tests were recorded.

5.3 AA5083-H116 Post-fire Residual Material Strength

Our observations of the post-fire microstructure of Al5083 indicated that cavitation development and dynamic grain structure evolution are the two primary features of the stress-induced microstructural damage. These two phenomena will cause competing effects on the post-fire residual strength for Al5083. To separate the stress-induced damage from the thermally-induced damage for Al5083, both unstressed thermal exposure and strained samples are tested to compare their post-fire residual mechanical properties.

True residual material strengths were estimated based on deformed cross sectional area after the creep test to study the influence of microstructural damage. Additional changes in cross section during the residual property tests were neglected. (Prior studies on strengthening mechanisms in aluminum alloys interpret results in terms of true stress,) In addition, engineering residual material strengths calculated based on the original cross sectional area prior to the creep tests were studied to provide information for structural design. The competing mechanism between strength degradation caused by cavitation and the strengthening effect due to grain elongation is also discussed in this chapter.

5.3.1 True Residual Mechanical Properties

Results from the simulated post-fire residual material strength tests after 200°C exposure are illustrated in Fig. 48. Slight strength degradations of 15MPa and 30MPa in ultimate and yield strength, respectively, are observed in the 200°C unstressed thermally exposed samples. As discussed above, for unstressed thermal exposure, the initial material strength degradation below 280°C is primarily caused by the subgrain coarsening during the dislocation recovery and secondarily due to β-phase (Al_2Mg_3) formation. Since Mg α-matrix depletion and β-phase (Al_2Mg_3) precipitation process takes a long time (several hours) to be completed at 200°C, the strength degradation of samples heated to 200°C under 50°C/min heating rate is primarily caused by the subgrain coarsening during the static recovery. The static recovery process will continue when samples are heated above 200°C, thus increasing the exposure duration at 200°C might cause a similar effect. The slight decrease in the residual strength of samples held at 200°C for 1000s and 2000s can be attributed to the additional static recovery in the extended duration exposures.

In addition to static material strength degradation, small amounts of additional strength reduction are exhibited in the strained samples. These stress-induced strength reductions may be attributed to the dynamic recovery during the thermal-mechanical process. Dynamic recovery is a softening effect which will reduce the dislocation multiplication during work hardening. The dislocation density is reduced through the cross-slip of screw dislocations and the climb of edge dislocations. These processes are strongly dependent on the elevated deformation temperature [49]. In previous research, the dislocation tangles were observed to disappear when aluminum was deformed between 100°C and 200°C. After deformations at 250°C, the dislocation tangles are nearly gone [48]. Although the mechanisms are similar between dynamic recovery and static recovery, the dynamic recovery proceeds at a rate controlled by the applied stress or strain rate, while static recovery proceeds at a declining rate which is affected by the internal stresses to cause heterogeneity [50]. Thus, compared to the strength degradation induced by static recovery, the dynamic recovery may cause more material strength degradation during deformation.

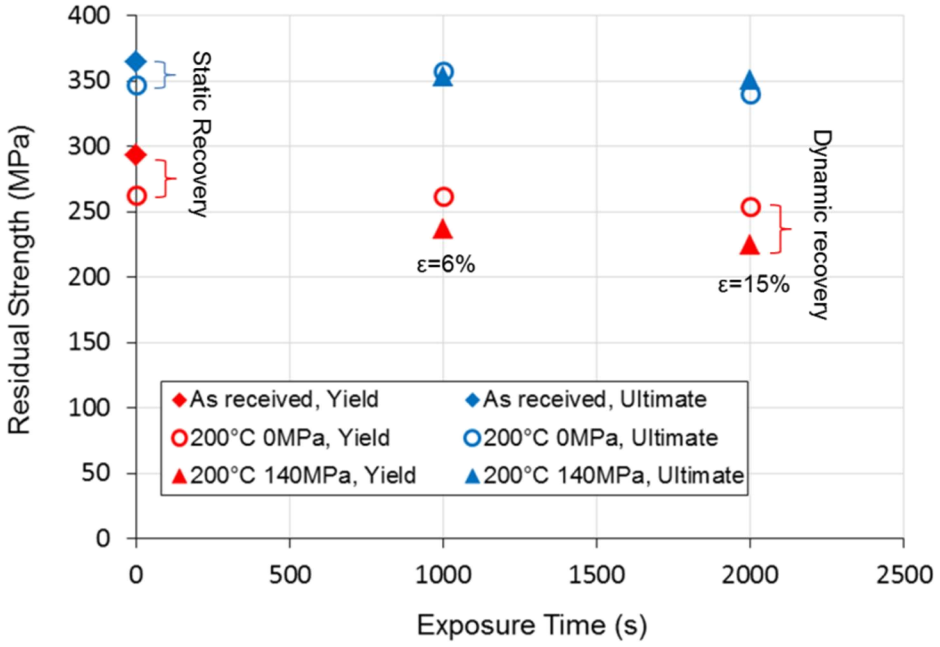

Fig. 48 Post-fire true residual strength of Al5083 after 200°C exposure

The different mechanisms in grain structure evolution resulting from 300°C exposure will also lead to differences in post-fire material response. Fig. 49 shows the post-fire residual material strength for both unstressed thermally exposed samples and strained creep samples. The samples initially heat treated to 300°C demonstrate approximately 30MPa and 60MPa reduction in post-

fire ultimate and yield strength. The initial strength degradations are caused by both static recovery below 280°C and the initiation of dynamic recrystallization at 300°C. When samples are held at 300°C for extended time periods, the stored energy of deformation from material processing is released due to the additional absorption of thermal energy. Then grain recrystallization will take place to attain a minimum energy state inside the material. Thus, there are continuing reductions in the post-fire ultimate and yield strength with the grain recrystallization process which is observed until the grain structure reaches an equilibrium state (sometime during the 1000s exposure). No further strength degradation occurs after grains are fully recrystallized at 1000s exposure for the unstressed thermal exposure samples.

The samples strained at 300°C exhibit strengthening behavior compared with the unstressed samples. The strengthening effect is smaller in the samples subjected to the smallest strain values--only 15-20MPa strength increment is observed in the 13%-30% strained samples. However, the strengthening effect becomes significant in the highly strained sample. The post-fire ultimate and yield strength increases by 50MPa and 120MPa respectively in the 100% strained samples. The amount of strength increase can be attributed to the grain elongation during the geometric dynamic recrystallization. Previous research suggests that the increase in strength is related to the growth in grain aspect ratio. Yield strength will increase as structure evolves from the equiaxed grain structure to the high aspect ratio grains [57]. Thus the elongated grain structure highly strengthens the material after large plastic deformation. This mechanism is similar to the hot rolling process in material manufacturing. Grain thickness is greatly reduced during the superplastic deformation and the flow stress will be strengthened with the increase of hot deformation strain [58, 88]. Simultaneously, cavity growth is also promoted by creep plasticity in the highly strained sample, as shown in Fig. 49b. Since the cavitation causes material strength degradation, there is a competing process between cavitation and grain elongation during the high plastic strains. In the 300°C, 100% strained sample, the cavity volume fraction is still relatively low (about 1.5%). Thus the material is strengthened due to the high grain aspect ratio and minimal cavitation.

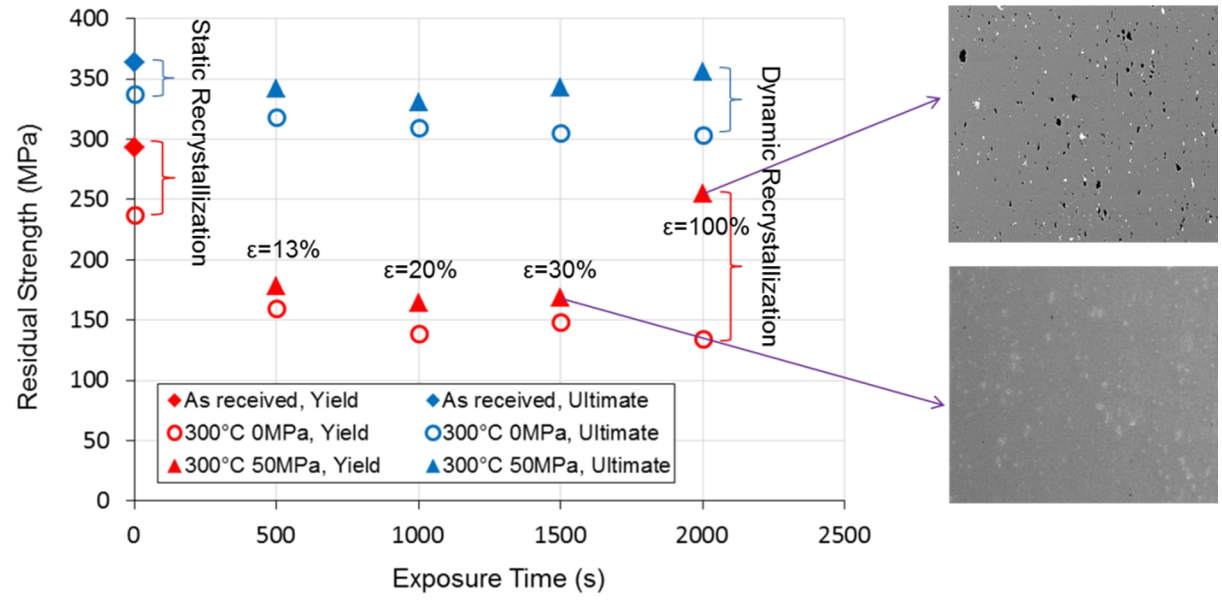

Fig. 49 (a) Post-fire true residual strength of Al5083 after 300°C exposure, (b) Cavitation in 100% strained sample and (c) Microstructure in 30% strained sample

Post-fire residual strength for samples exposed at 400°C exhibits similar behavior compared with samples exposed at 300°C except for the initial strength degradation due to thermal exposure. For the sample initially heated to 400°C, the material strength decreases primarily due to the static grain recrystallization. This results in a decrease in the residual yield and ultimate strengths of 160MPa and 50MPa, respectively. As the soak time increases, residual strength of the thermal exposure samples remains constant, which is due to the fact that material has fully recrystallized by the time sample reaches 400°C.

The strained samples exposed to 400°C show similar strengthening effects with 300°C exposed ones. This effect is more apparent in the highly strained samples than in those subjected to smaller strains. Compared to unstressed samples, residual material strengths of the strained samples have similar yield strength at low strain levels (25% and 50% strain). However, the yield strength of strained samples increases by 30MPa at the high strain levels (100% and 143% strain). This strengthening response in post-fire strength is also related to the grain structure evolution. The dramatic increase of grain aspect ratio from 0.91 to 7.5 in Fig. 37a is the evidence of geometric dynamic recrystallization during 400°C deformation. As we discussed in the 300°C section, yield strength is believed to be at a minimum value at the equiaxed state, then to increase

with the increase of grain aspect ratio [57]. Dislocations are also recreated during the grain elongation and new small grains form, resulting in the refinement of the dislocation sub-structures. Smaller subdomains are developed with the accumulation of creep strain. Based on Huskins' model, the material's residual strength will increase due to the size refinement of the subgrain structures [19]. Thus the increase of yield strength with strain was attributed to the strengthening by grain elongation and subgrain refinement during the geometric dynamic recrystallization at high stain levels.

The previous discussion reveals two completing mechanisms during creep deformation: cavitation which degrades the residual strength by introducing defects inside the material and grain elongation which strengthens the material by strain hardening of the grains. From Fig. 37a and b, the effects of these two mechanisms are enhanced with an increase in creep strain. Thus no change in strength was observed for strains of 50% due to the small amount of cavitation and grain elongation as seen in Fig. 37. At high strain levels (100% and 143%) where cavitation is significant and grains become highly elongated, the two effects counteract each other resulting in only a small difference in the yield strength.

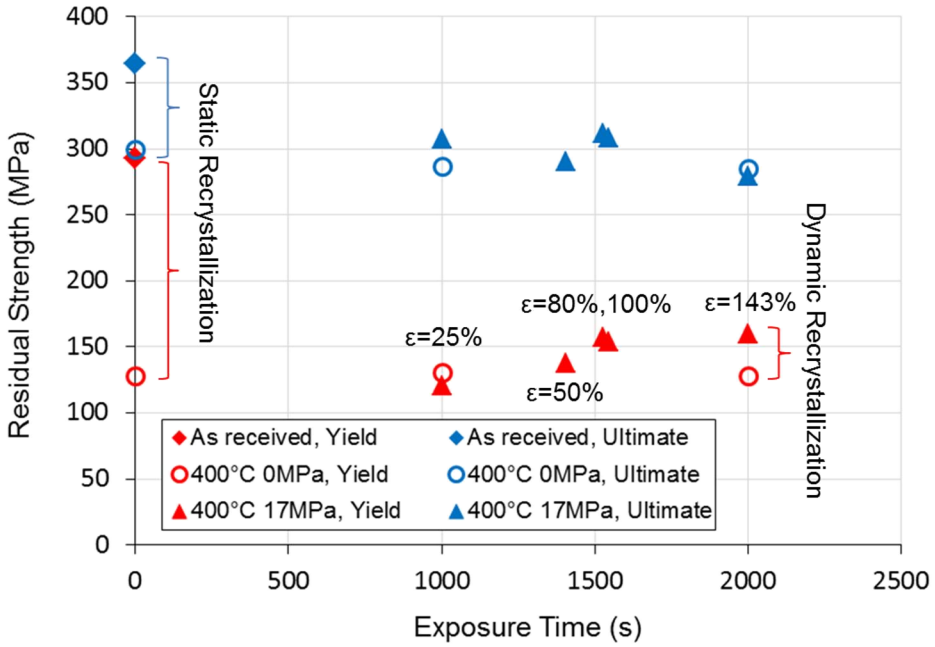

Fig. 50 Post-fire true residual strength of Al5083 after 400°C exposure

Previous numerical simulations have suggested that a material's yield stress display parabolic relationship versus the logarithm of the grain aspect ratio [57]. During the competing process

between grain elongation and cavitation, the effect of cavitation can be neglected in the low cavity area fraction sample. Thus the residual yield strength which is primarily strengthened by grain elongation can be represented as a parabolic function of the logarithm of the grain aspect ratio, as shown in Fig. 51. Minimal strength occurs at the equiax grain structure; then the residual yield strength increases parabolically with increasing logarithm of the grain aspect ratio. In the situation that the microstructure has been seriously damaged, strength degradation induced by high cavity area fraction will counteract the strengthening effect due to grain elongation. Compared to the parabolic curve at low cavitation state, about 80MPa reduction in residual yield strength is caused by the high cavity volume fraction in the seriously damaged sample. However, the significant increase in grain aspect ratio still cause an increase of approximately 30MPa in residual yield strength, suggesting that grain elongation is the dominant effect to cause residual strength increase during Al5083 creep process, even at a high cavitation state.

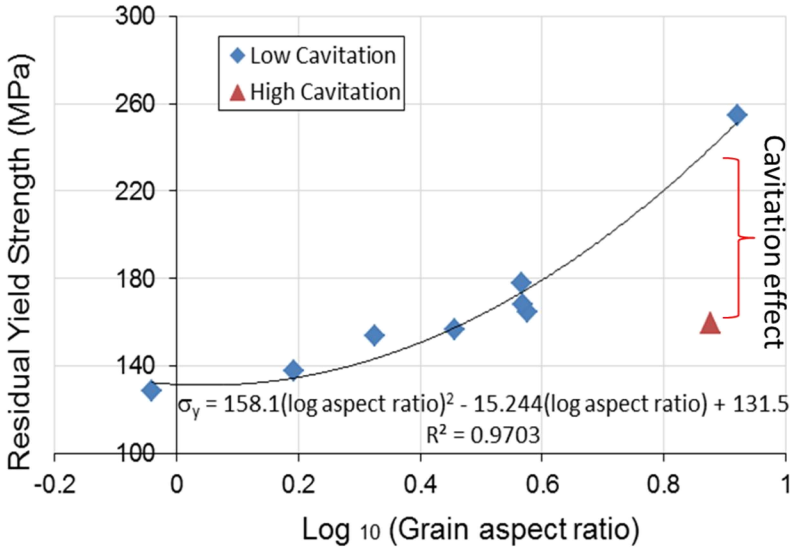

Fig. 51 Post-fire true residual strength of Al5083 as a function of logarithm of grain aspect ratio

5.3.2 Engineering Residual Mechanical Properties

The post-fire mechanical properties for load-bearing 5083 aluminum alloy deformed at various temperatures are summarized in Table 2. Both residual material strengths calculated based on the deformed cross sectional area after creep tests (true stress: $\sigma_{0.2\%\_T}$, σ_{ult_T}) and the original cross sectional area before creep tests (engineering stress: $\sigma_{0.2\%\_E}$, σ_{ult_E}) are listed.

As discussed above, the true residual material strength is affected by the internal stress-induced microstructural damage during the thermo-mechanical test. The competing mechanism between cavitation development and dynamic recrystallization causes negligible effect on the true residual strength at low strain level. However, the significant grain elongation causes obvious strengthening response in true residual strength at high creep strain. This true residual strength evaluation provides an insight of the linkage between microstructure change and the post-fire material behavior.

Table 2 Post-fire Mechanical Properties of 5083 Aluminum Alloy

Sample	Creep T_c (°C)	Creep σ_c (MPa)	Creep ε_c (%)	Reduction in Aera (%)	Post-fire $\sigma_{0.2\%\_T}$ (MPa)	Post-fire σ_{ult_T} (MPa)	Post-fire $\sigma_{0.2\%\_E}$ (MPa)	Post-fire σ_{ult_E} (MPa)	Post-fire ε_{ult} (%)
200_1	200	140	6	5.8	236.7	353.5	223	332.9	23.7
200_2	200	140	15	11.1	224.5	350.4	199.7	311.6	23.4
300_1	300	50	13	13.1	177.9	342.1	154.6	297.3	26.5
300_2	300	50	20	21.4	164.5	330.7	129.3	259.8	29.8
300_3	300	50	30	33.2	168.2	342.9	113.1	229.2	34.5
300_4	300	50	100	77.1	254.8	355.7	59.8	83.3	3.5
400_1	400	17	25	17.2	120.4	307.2	99.7	254.4	54.6
400_2	400	17	50	41	137.5	290.1	81.1	171.2	20.7
400_3	400	17	80	55.7	153.7	308.3	68	136.4	15.6
400_4	400	17	100	63.8	156.7	311.9	56.5	112.8	12.7
400_5	400	17	143	84.3	159.6	279.2	25	43.8	3.7

The engineering residual material strength is calculated based on the original structural geometry before the thermo-mechanical deformation, thus is provides information relevant for structural design and assessment of the residual load carrying capability of a structure in comparison to its initial load carrying capability. Since great reduction in net section will reduce the structures'

performance after fire exposure, large amount of localized plastic strain will cause significant strength degradations in material. As shown in Fig. 52, the engineering residual material strength decreases as a function of the reduced cross sectional area of strained samples. During the residual strength degradation, the unstressed thermal exposure sample provides the baseline for the strained sample at each temperature, as illustrated in Fig. 53. Further strength degradation base on the heat affected strength is accumulated with the increase of reduced area in the strained sample.

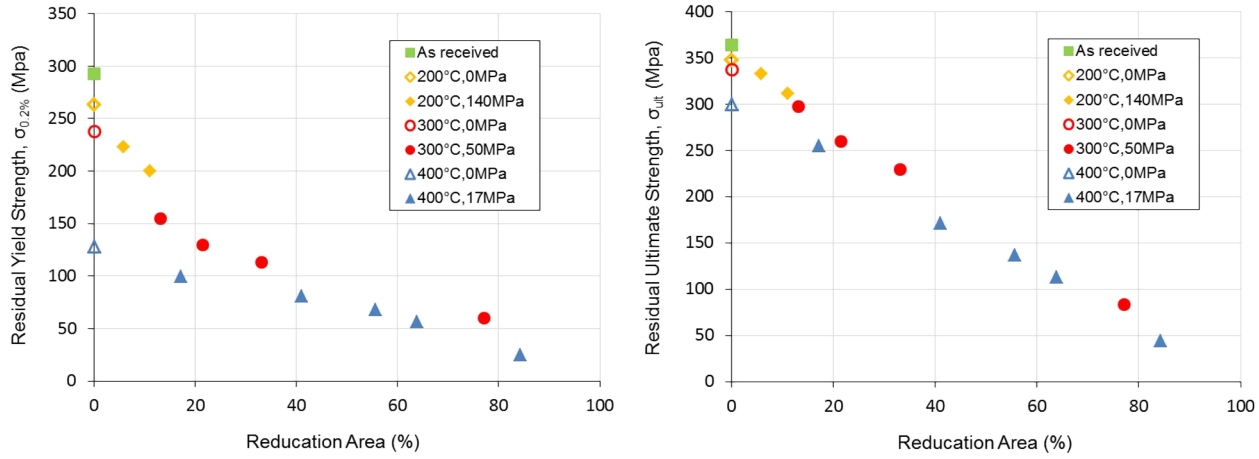

(a) (b)

Fig. 52 Engineering residual material strength vs. Cross sectional reduction of area for Al5083

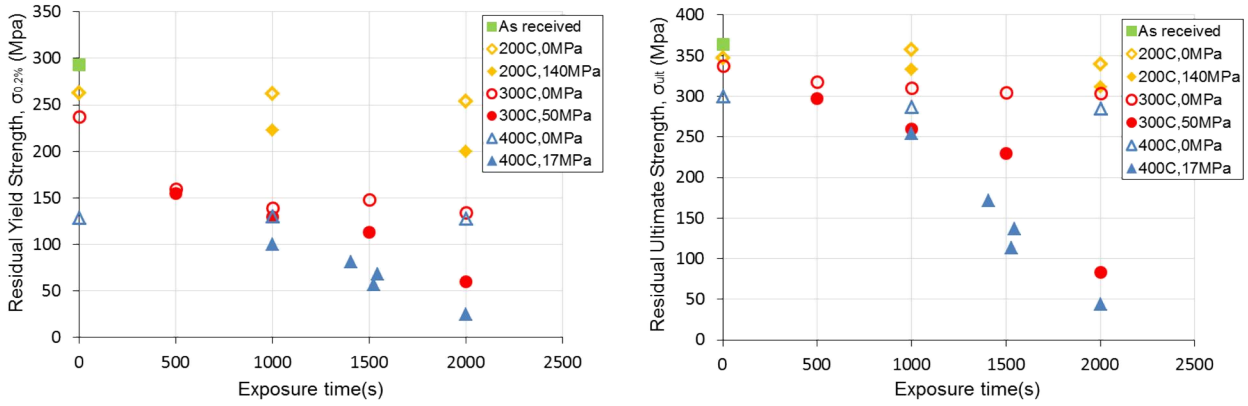

(a) (b)

Fig. 53 Engineering residual material strength vs. Exposure Time for Al5083

For the strained samples exposed at low temperature (200°C), the increase in material's ductility is limited, only 15% of creep strain can be developed before material failure. The plastic strain localized (necking) is also not that significant, only 11% of cross sectional area is reduced at the

strained sample before 200°C creep failure. Thus the residual strength does not exhibit large decline; about 70% of engineering residual yield strength is retained in the strained sample before the 200°C creep failure occurs.

However, the microstructure will be greatly changed after high temperature exposure (300°C and 400°C), grains are highly elongated during geometrical dynamic recrystallization process. Grain boundary sliding also occurs and contributes to material's ductility. Thus, the ductility of Al5083 is significant increased at 300°C and 400°C exposure, more than 80% of cross sectional area can be reduced before failure in the thermo-mechanical condition. Therefore, the load-bearing structure will be deformed severely before creep failure during high temperature exposure and exhibits significant strength degradation, only 10%~20% residual yield strength is retained before material failure.

Fig. 54(a) displays the ultimate tensile strain in the post-fire tensile test (Post-fire Ductility) for both unstressed thermal exposure and strained Al5083 samples. Compared to the as received sample, the post-fire ductility of the 200°C unstressed samples are slightly increased and remain constant after longer heating duration. The 200°C strained samples show similar post-fire ductility with unstressed one due to their low creep strain. The post-fire ductility of 300°C unstressed samples is also slightly increased at the initial exposure state but increases with the increase of exposure time, while the 300°C strained samples display decreasing post-fire ductility with the increase of exposure time/creep strain. In contrast, the post-fire ductility at 400°C unstressed thermal exposure is significantly increased to the maximum value, and then slightly decreases with the increasing exposure time. The 400°C strained samples exhibit significant decrease in post-fire ductility with the increasing exposure time due to the significant increase in creep strain.

The total plastic strain in both creep and post-fire tensile test (Total Ductility) for Al5083 heat treated samples are illustrated in Fig. 54(b). The strained samples display higher total ductility than the unstressed thermally exposed ones due to the accumulation of creep strain. Total ductility for 200°C strained samples is only slightly increased with exposure time because only 15% of creep strain can be developed before creep failure. However, the total ductility of high temperature strained samples (300°C and 400°C) is significantly increased with the increase of exposure time/creep strain. The large creep strains developed during 300°C and 400°C creep

tests primarily contributes to the total ductility of Al5083 samples. As discussed in the previous chapter, both grain deformation and grain boundary sliding have made significant contributions to the creep strain, and then contribute to the total ductility of material.

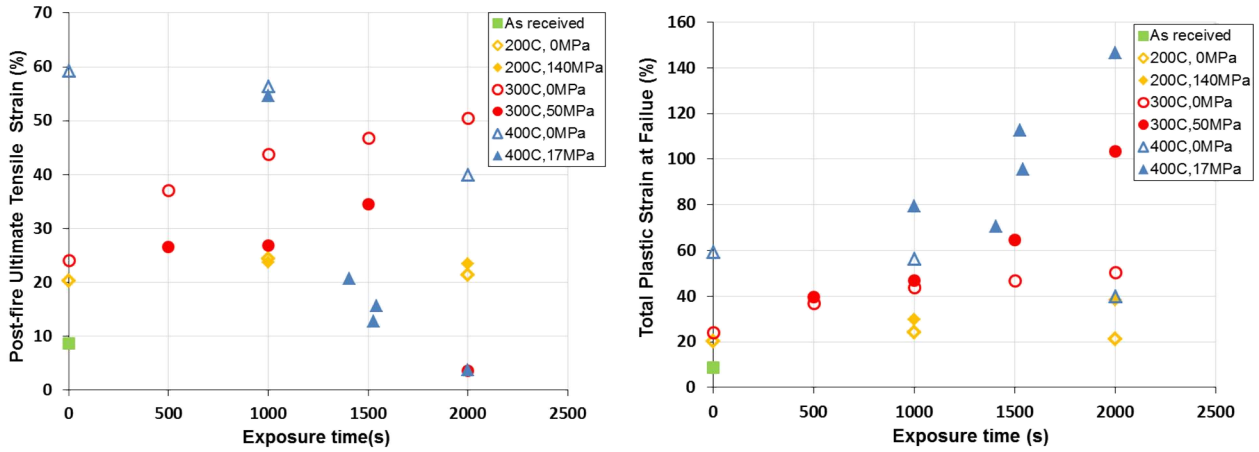

(a) (b)

Fig. 54 (a) Post-fire ultimate tensile strain (b) Total plastic stain in both creep and post-fire tensile test for Al5083

5.4 AA6061-T651 Post-fire Residual Material Strength

Al6061 has a distinct strengthen mechanism in comparison with Al5083--the precipitation sequence during thermal exposure makes the primary contribution to the residual strength of Al6061. In addition to the cavitation development and dynamic recrystallization in Al5083, dynamic precipitation also occurs in Al6061 during the thermo-mechanical deformation. These stress-induced microstructural damages have caused diverse post-fire response at different exposure temperature for Al6061.

True residual strength calculated based on deformed cross sectional area of Al6061 creep samples is compared to the unstressed thermal exposure sample to separate the stress influence. Engineering residual strengths calculated based on original cross sectional area before creep damage is also listed to provide guidance for aluminum structural design. Similar competing mechanism between cavitation and grain elongation are also discussed for high strained Al6061 sample tested at 400°C.

5.4.1 True Residual Mechanical Properties

True residual strength results for post-fire Al6061 strained samples exposed at 200°C are shown in Fig. 55. Residual strength for as received and unstressed thermal exposure samples is also listed for comparison. Compared to the as received material strength, the initial exposure to 200°C does not cause significant change in both residual yield and ultimate strength for Al6061. The extension of exposure duration at 200°C only causes slight decrease in residual material strength (approximately 10MPa in residual yield strength and 35MPa in residual ultimate strength). As discussed above, the transformation from metastable β″ phase precipitation to β′ phase occurs between approximately 250°C - 300°C to cause initial strength degradation in Al6061. Thus, for the unstressed sample initially heated to 200°C, no precipitate transformation has taken place to cause material strength degradation. However, during the additional soak time at 200°C, more thermal energy is absorbed to promote β″ phase precipitate transform to β′ phase. Thus some small strength degradation is observed due to the initial β″ precipitate formation process with time.

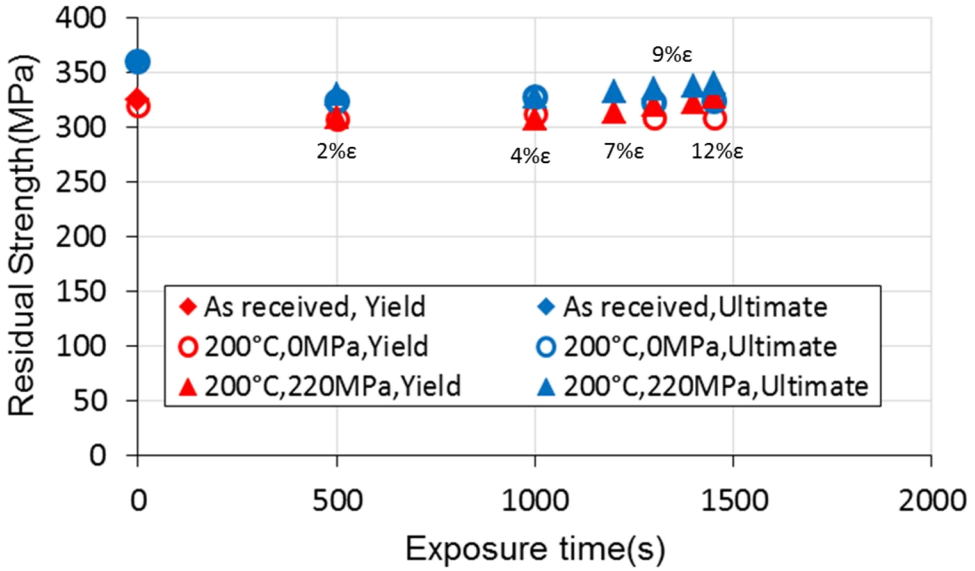

Fig. 55 Post-fire true residual strength of Al6061 after 200°C exposure

The strained samples display similar post-fire residual strength with the unstressed thermally exposed samples. Almost no change in both residual yield and ultimate strength is observed between the strained and unstressed thermal exposure samples. Due to the low ductility of 200°C exposed samples, limited strain has been developed before 200°C creep failure. No measurable

cavitation and almost no grain elongation are observed in the microstructure of 200°C strained samples. Thus, the applied stress does not cause any additional effect on the post-fire residual strength of Al6061 samples tested at 200°C.

The post-fire residual strength of damaged sample treated at 300°C displays different behavior with 200°C. A small amount of strength degradation (80MPa and 90MPa in residual ultimate and yield strength, respectively) is observed in the unstressed samples initially heated to 300°C. A continuing decrease in residual strength is shown for unstressed samples soaked at 300°C. Previous studies [22] reveal that the metastable β″ phase precipitate evolves to β′ phase between approximately 250°C - 300°C under the heating rate of 20°C/min. When a sample is heated to 300°C at 20°C/min, the metastable β″ phase precipitate transforms to β′ phase. The size of the β′ phase precipitates is larger than the fine β″ precipitates. Thus the strengthening effect of the fine β″ precipitates will be decreased; the precipitate size increase in the form of β′ phase will reduce the interaction with dislocations and cause the initial strength degradation in Al6061. A previous study also suggested that the β′ precipitation peak temperature at ~310°C [22]. With a continued hold at 300°C, the β′ phase precipitation will peak and subsequently dissolve with the continuous absorption of thermal energy, which resulting in the continuing decline in post-fire residual strength with time.

The strained samples deformed at 300°C thermo-mechanical tests also exhibit similar residual strength with the unstressed thermally exposed ones. No additional change in both residual yield and ultimate strength has been developed due to the applied stress. Recall the stress-induced microstructural damages discussed in previous two chapters: 300°C exposure does not show any cavitation until a large number of cavities appear at the last stage just before brittle failure. Only minimal elongation is observed in the grain structure due to the limitation of strain before creep failure. These combined phenomena provide an insight into the competing effect between cavitation and grain elongation before creep failure at 300°C. However, less than 20% creep strain has been developed before 300°C creep failure; the effects of both minimal cavitation and slight grain elongation are too weak to cause a significant residual strength change in the 300°C strained sample. The similar strength degradation with unstressed thermal exposure samples is caused by similar precipitation process during the same heating duration.

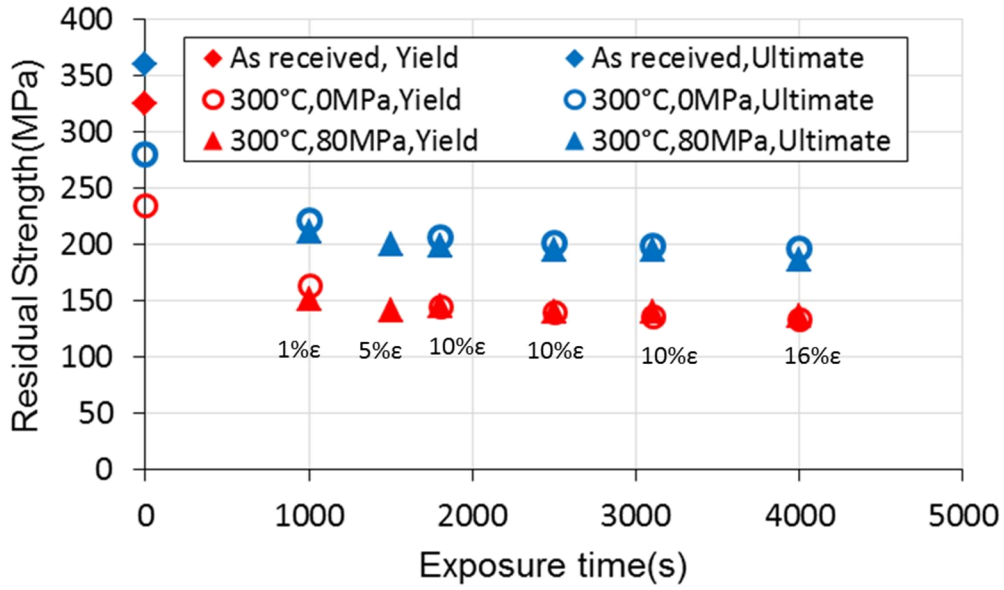

Fig. 56 Post-fire true residual strength of Al6061 after 300°C exposure

The unstressed samples exposed to 400°C exhibit similar residual strength degradation phenomenon with those exposed to 300°C. Large strength degradations (225MPa and 160MPa in the residual yield and ultimate strength respectively) are observed in the sample initially heated to 400°C. For a continuing hold at 400°C, a small additional decrease (about 50MPa in ultimate strength and 40MPa in yield strength) is observed in the unstressed thermally exposed sample. These observations can also be explained by the previous research [22]. 400°C is within the range of the β′ phase dissolution peak between 350°C and 420°C, and then β phase precipitates. The size of β phase precipitates is several microns, which is much larger than the β′ phase precipitates. Thus, the formation of the equilibrium β phase causes the significant reduction in residual strength after samples are exposed to 400°C. The equilibrium β phase peak is identified to be ~460°C, thus β phase precipitation continuously appears during sample soaking at 400°C. When large β precipitates govern the strengthening phase, the residual yield strength drops to the minimum value.

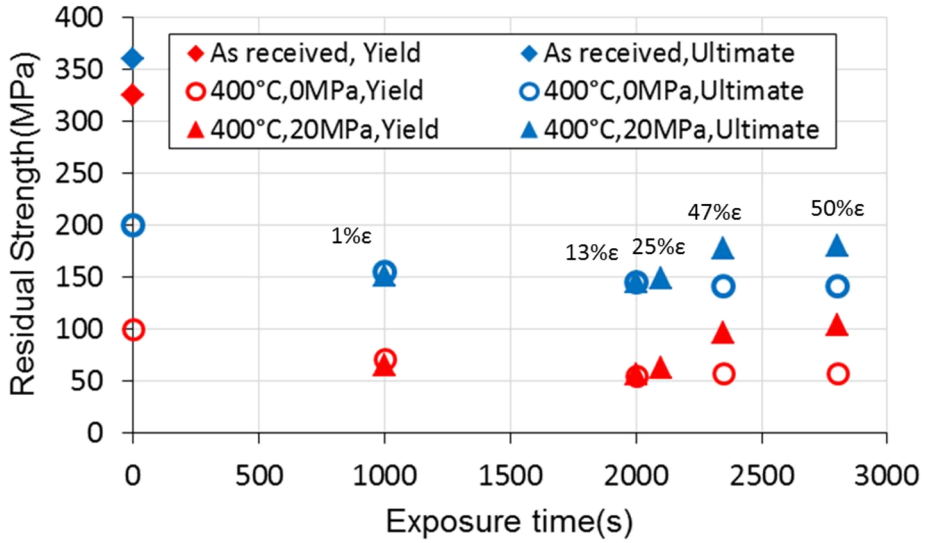

Fig. 57 Post-fire true residual strength of Al6061 after 400°C exposure

The residual strength of strained samples exhibits similar values with the unstressed thermally exposed samples at low strain levels. However, slight increases in both residual yield and ultimate strength are observed in the highly strained samples. About 40MPa yield and ultimate strength increase is displayed in both 47% and 50% creep strain samples. The post-fire mechanical properties are closely related to the microstructural changes. During 400°C thermo-mechanical tests for Al6061, cavity nucleation, dynamic grain structure evolution, and dynamic precipitation take place concurrently. During dynamic precipitation at 400°C, the second phase Si precipitates are found to dissolve with the accumulation of creep strain, while other second-phase Mg_2Si particles are cut and fragmented by the dislocations during plastic deformation. Thus dynamic precipitation at 400°C only has limited contribution the material strength [60]. Cavitation development is also small during the 400°C creep test. All the cavities remain small and spherical until failure; and the cavity volume fraction before creep failure at 400°C is only 1.9%. In contrast, dynamic recrystallization has a strong effect on the grain structure. Grain aspect ratio is significantly increased from 1.34 in the as received state to 6.35 in the just-before-rupture state, as shown in Fig. 43.

Based on previous study, the change of grain shape will affect material strength [56]. During the grain structure evolution, the increase in grain aspect ratio will cause material's yield strength to increase [57]. Moreover, grain elongation is similar to the strain hardening process. Dislocation density will be increased during the grain elongation. The resulting size refinement in subgrain

structures divided by dislocations will cause strengthening effect in material strength [19]. Thus during all the stress-induced microstructural damage in Al6061, dynamic grain structure evolution has the controlling effect on the post-fire material response. The increase in yield strength at high strain levels was attributed to the strengthening by grain elongation and subgrain refinement during the dynamic grain structure evolution. The strength degradation caused by cavitation development is completely counteracted by the strengthening effect of grain elongation.

The cavitation effect in Al6061 is weaker than Al5083; only 1.9% of cavity area fraction has been developed before Al6061 creep failure. Thus the residual yield strength in Al6061 can also be represented as a parabolic function of logarithm of the grain aspect ratio, as shown in Fig. 58. Unlike Al5083, minimum yield strength occurs in the as received state due to no grain recrystallization takes place in Al6061. The increase rate of residual yield strength also appears more slower in Al6061. For the same grain aspect ratio, the increase in Al5083's residual yield strength is twice of the strength increase in Al6061. However, grain elongation also dominates the post-fire true residual strength due to low cavitation in Al6061.

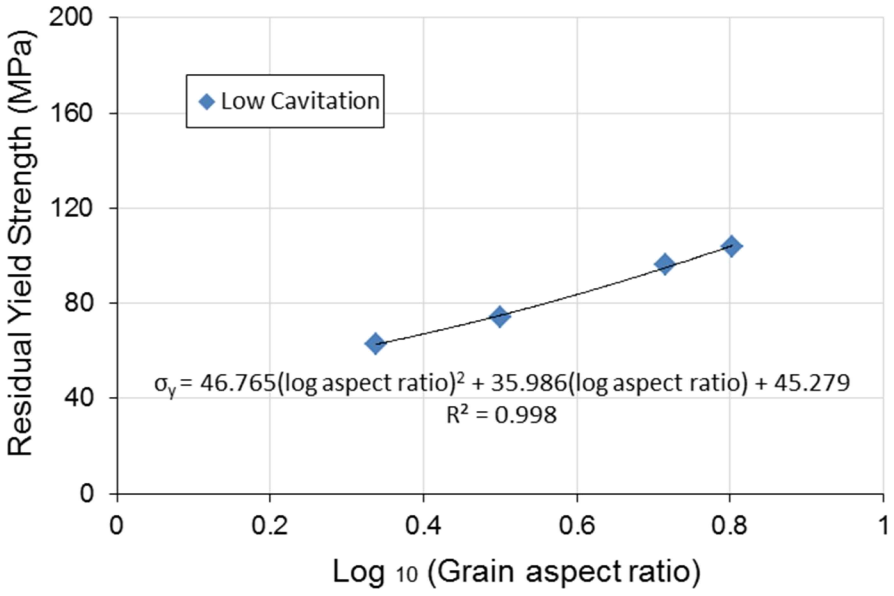

Fig. 58 Post-fire true residual strength of Al6061 as a function of logarithm of grain aspect ratio

5.4.2 Engineering Residual Mechanical Properties

Table 3 contains summarized post-fire residual mechanical properties for the load-bearing 6061 aluminum alloy strained to multiple strains at various temperatures. True residual material strengths calculated based on the deformed cross sectional area after creep tests (true stress: $\sigma_{0.2\%\_T}$, σ_{ult_T}) and engineering residual material strengths calculated based on the original cross sectional area before creep tests (engineering stress: $\sigma_{0.2\%\_E}$, σ_{ult_E}) are listed for comparison.

As discussed in the previous two chapters, cavitation, dynamic grain structural evolution, and dynamic precipitation take place concurrently during the thermo-mechanical tests. The post-fire true residual strength in the strained sample results from the combined effect of these stress-induced microstructural damages. Since the cavitation development and grain structural evolution are not obvious due to the low strains before creep failure at low exposure temperatures (200°C and 300°C), almost no stress effect is observed on Al6061's true residual strength. However, the competing mechanisms of grain elongation and cavitation at high strain levels during 400°C creep tests cause some increase in true residual strength. The second phase Si and Mg-Si rich precipitates are observed to dissolve during plastic deformation and only have limited strength contribution.

Table 3 Post-fire Mechanical Properties of 6061 Aluminum Alloy

Sample	Creep T_c (°C)	Creep σ_c (MPa)	Creep ε_c (%)	Reduction in Aera (%)	Post-fire $\sigma_{0.2\%\_T}$ (MPa)	Post-fire σ_{ult_T} (MPa)	Post-fire $\sigma_{0.2\%\_E}$ (MPa)	Post-fire σ_{ult_E} (MPa)	Post-fire ε_{ult} (%)
200_1	200	220	2	1.9	308.6	330/5	302.9	324.4	19.1
200_2	200	220	4	5.3	308.1	327.5	291.7	310.1	15.4
200_3	200	220	7	9.4	313.6	332	284.2	300.9	13.0
200_4	200	220	9	13.9	319.5	335.2	275	288.6	10.4
200_5	200	220	9	14.5	322.6	337.3	276	288.5	9.7
200_6	200	220	12	19	327.2	340.5	265.1	275.8	7.6
300_1	300	80	1	0.93	151.7	210.9	150.3	208.9	20.9

300_2	300	80	5	6.4	141.2	199.8	132.1	187	18.3
300_3	300	80	10	15.7	144.6	198.2	121.9	167.2	13.2
300_4	300	80	10	11.7	140.2	195.1	123.7	172.2	13.9
300_5	300	80	10	12.9	140.5	194.7	122.5	169.7	12.8
300_6	300	80	16	27.7	136.8	186.1	98.9	134.5	7.1
400_1	400	20	1	1	64.6	151.0	64.0	149.5	27.7
400_2	400	20	6	6.0	56.3	142.6	52.9	134.1	29.1
400_3	400	20	13	16.4	56.9	144.5	47.6	120.8	24.8
400_4	400	20	5.5	7.2	61.6	161.0	51.6	134.8	29.5
400_5	400	20	25	33.4	63.0	148.4	42.0	98.9	17.1
400_6	400	20	43	50.3	74.3	138.3	37.9	68.7	10.5
400_7	400	20	37	56.7	96.1	178.1	41.61	77.2	9.1
400_8	400	20	50	67.5	103.7	179.9	33.4	58.4	6.1

The engineering residual material strength of strained Al6061 samples deformed from 200°C to 400°C are listed in Fig. 59 and Fig. 60. For each exposure temperature, the engineering residual material strength decreases as a function of the reduced cross sectional area of the strained samples. The unstressed thermally-induced residual strength also provides the baseline for stress-induced strength degradation, as shown in Fig. 60. The additional strength degradation in strained Al6061 sample primarily depends on the reduction in area.

Since only small amount of strength degradation occurs during Al6061 samples held at 200°C, and limited strain has been developed before 200°C creep failure, the residual strength of strained sample does not exhibit signification degradation due to the small reduced area (19%) before failure. Thus about 80% of as received yield strength can be retained before load-bearing structure failure at 200°C.

Samples treated at 300°C display more strength degradation due to the β′ precipitation peak and dissolution process with holding time. However, the ductility of Al6061 is still low as no significant grain boundary sliding during 300°C creep. Only 19% creep strain and 27% reduced cross sectional area are developed before 300°C creep failure. Thus most of the residual strength degradation at 300°C is caused by thermal exposure; only small amount of residual strength is decreased by the limited reduced area in the neck region. Only 30% of as received yield strength can be retained before structure failure at 300°C.

Al6061 samples tested at 400°C exhibit the minimum residual strength due the equilibrium β phase formation. Great increase in ductility and reduced cross sectional area are also observed in the 400°C creep samples. About 60% creep strain and 67% reduced cross sectional area will be achieved before 400°C creep failure. The combination of the equilibrium β phase formation during thermal exposure and large cross sectional area reduction cause about 90% of residual yield strength degradation before structure failure at 400°C.

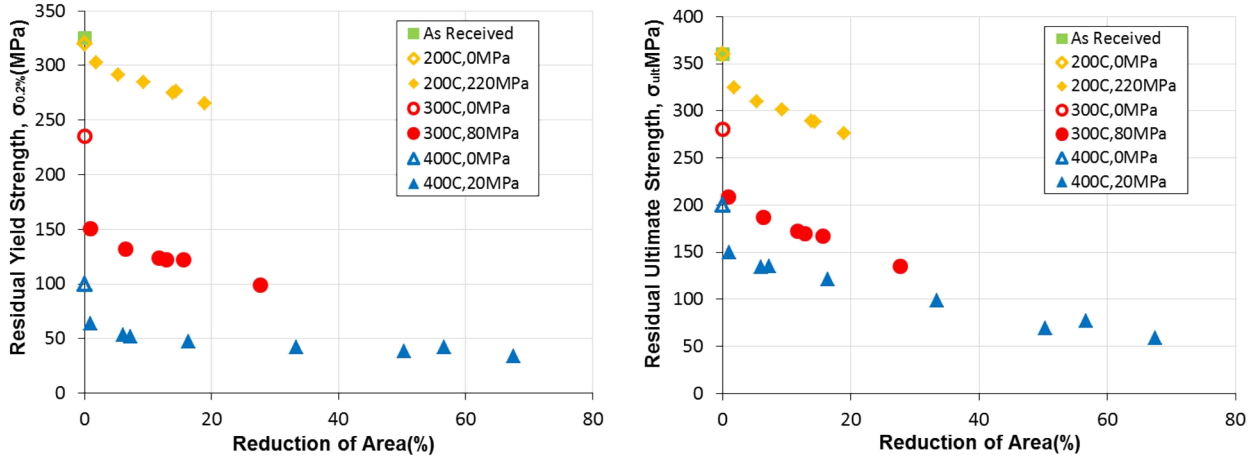

(a) (b)

Fig. 59 Engineering residual material strength vs. Cross sectional reduction of area for Al6061

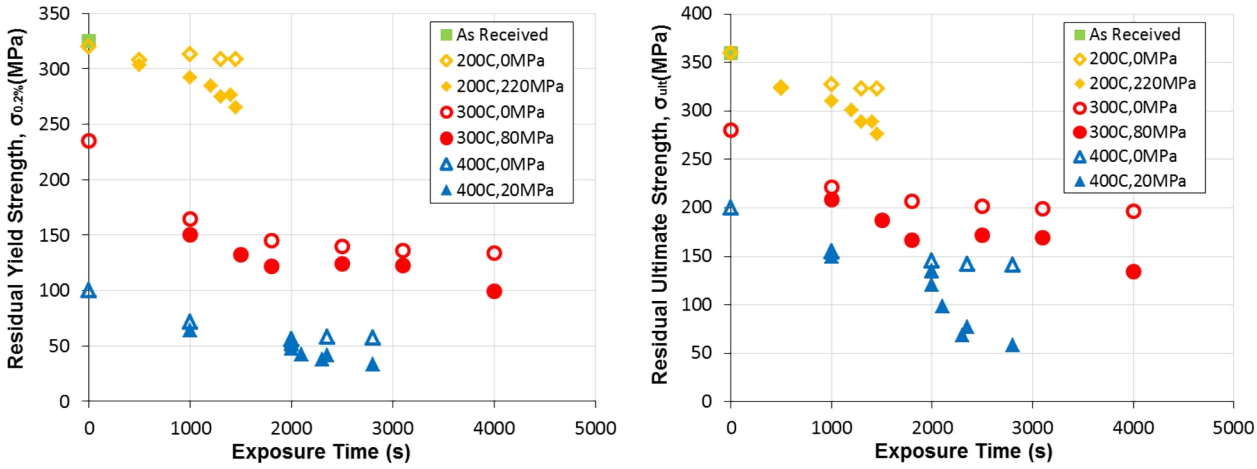

(a) (b)

Fig. 60 Engineering residual material strength vs. Exposure Time for Al6061

The post-fire ultimate tensile strains (Post-fire Ductility) for both unstressed and strained Al6061 samples treated at different temperature are listed in Fig. 61(a). Unstressed heat treatment from 200°C to 400°C causes similar increase in material's post-fire ductility (about 12% compared to the as received value). The extended heating duration at 200°C and 300°C only slightly affects the post-fire ductility. However, the increasing exposure time at 400°C cause material's ductility to increase to 36% and then stay nearly constant. Strained samples display lower post-fire ductility than the unstressed ones. The ductility of strained samples is observed to decrease with the accumulation of creep strain. Similar ductility (about 6%) is observed in the strained samples before creep failure at 200°C to 400°C.

Fig. 61(b) exhibits the total plastic strain (Total Ductility) in both creep test and post-fire tensile tests. The 200°C and 300°C strained samples display similar total ductility (about 22%) with the unstressed thermal exposure samples due to limited contribution from the low creep strain before creep failure. However, the total ductility for 400°C strained samples is significantly increased compared with the unstressed ones due to the large creep strain developed during 400°C creep tests. Since grain deformation can accommodate the creep strain in Al6061 samples, grain elongation is the primary contribution to both creep ductility and total ductility of Al6061.

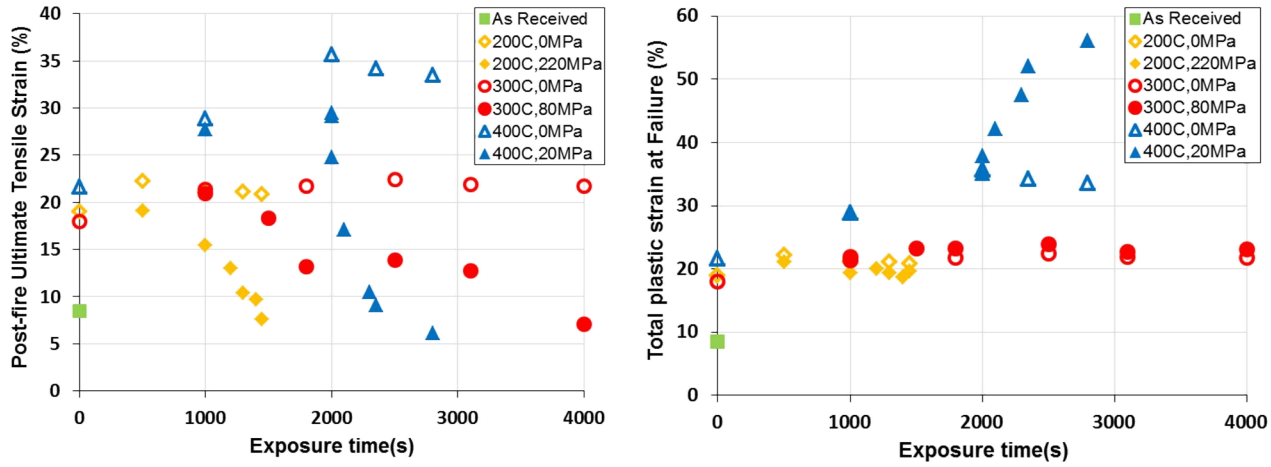

(a) (b)

Fig. 61 (a) Post-fire ultimate tensile strain (b) Total plastic stain in both creep and post-fire tensile test for Al6061

5.5 Conclusion

This chapter has studied the stress-induced post-fire response of Al5083 and Al6061. Post-fire uniaxial test is applied to measure the residual strength of both alloys after thermo-mechanical tests. The residual mechanical properties of unstressed thermally exposed samples are also measured to provide baseline for the stress-induced post-fire response. True residual material strengths based on deformed cross sectional area after the creep test are calculated to provide the insight of how microstructural damage affects the post-fire material response.

For Al5083 mechanical strained samples, minimal effect of stress on strength degradation for samples exposed to 200°C temperatures is observed. Static recovery causes the initial strength degradation during thermal exposure to 200°C. The subsequent dynamic recovery in the strained samples causes only slight additional strength degradation. However, material strained at 300°C and 400°C displays distinct behavior in post-fire response. The stress effect on the post-fire residual strength is minimal at the low strain levels due to low cavitation and minimal grain elongation. At high strain levels, geometrical dynamic recrystallization causes grains to evolve from an equiaxed grain structure to a textured thin grain structure. The grain aspect ratio increases significantly with the increase of plastic strain/reduction in area. Thus, the material is strengthened by subgrain structure refinement during grain elongation. Simultaneously, the

cavity volume fraction is also greatly increased to degrade the material strength with the accumulation of plastic strain. The reduction in strength due to cavitation is counteracted by the strengthening effect of grain elongation. Therefore, the competing process between cavitation and grain elongation caused an increase in strength over unstressed samples despite significant cavitation at high strain levels.

Al6061 exhibits distinct post-fire response with Al5083. Samples mechanically strained at 200°C and 300°C display similar strength with the unstressed thermally exposed ones. Almost no stress influence on the residual strength is observed due to the low ductility before 200°C and 300°C creep failure. Thus, the major contribution to 200°C and 300°C residual strength degradation is the precipitation transformation during thermal exposure. The stress effect on residual strength is also minimal at the 400°C low strain levels due to low cavitation and minimal grain elongation. However, material is strengthened at the high strain levels in the 400°C creep test by the dominate effect of dynamic grain structure evolution. Grains are highly elongated to cause increases in the dislocation density increase and subgrain refinement during large plastic deformation at 400°C. Thus in the competing process between highly elongated grain structure and low cavitation at 400°C, the subgrain strengthening effect caused by grain elongation overcomes the weakening effect induced by cavitation. Dynamic precipitation also takes place and is represented as the dissolution of second phase precipitates during creep at high temperature, which makes almost no contribution to residual strength.

In additional to true residual strength analysis, engineering residual material strengths calculated based on the original cross sectional area prior to creep tests are also studied to provide guidance for structural design. Similar observations are displayed in engineering residual strength for both alloys: the residual strength in the strained sample decrease with the increase of reduced cross sectional area in the neck region; while the total ductility of creep samples increases due to the accumulation of creep strain. Unstressed thermally exposed samples provide the baseline of residual strength and ductility at each exposure temperature.

CHAPTER 6 – Conclusions & Recommendations

6.1 Conclusions

Stress-induced microstructural damages and their linkages to post-fire material response for both Al5083-H116 and Al6061-T651 have been studied in this work. Thermo-mechanical tests were conducted at various temperatures and stresses to simulate the fire scenarios for load-bearing aluminum structures. Materials damaged at multiple creep strain levels were examined by scanning electrical microscopy and high resolution optical microscopy to study the microstructural features. To separate the effects of the stress-induced damage, microstructure evolution in both strained and unstressed thermally exposed samples heated for the same duration were examined. Cavitation development, dynamic recovery, dynamic recrystallization, and dynamic precipitation which occurred during the thermo-mechanical process were classified as stress-induced microstructural damage. The influence of stress on these microstructural damages exhibited distinct features at different heated temperatures.

At low heated temperature, no significant change appears in the damaged microstructure. The ductility of aluminum alloys studied was not significantly increased during low temperature exposure–less than 15% creep strain can be developed before aluminum failure in the 200ºC thermo-mechanical tests. Thus, during 200ºC creep grains in both alloys still maintain similar morphology with the as received state, with no obvious change in the grain aspect ratio until creep failure takes place. Cavitation has also not been developed in the 200ºC thermo-mechanical test due to the limited creep strain before failure. However, dynamic recovery occurred during 200ºC creep and the dislocation density was reduced to cause a softening effect in Al5083. For Al6061, the initial exposure to 200ºC was not high enough to cause precipitate transformation.

Thermo-mechanical tests conducted at high temperature caused great increases in the ductility of Al5083. More than 130% creep strain was developed before creep failure at 300ºC and 400ºC. Grains were highly stretched and grain boundaries become serrated at the high strain levels. Geometrical dynamic recrystallization took place to cause new grain formation at the location where the serrated grain boundaries contacted each other. Dislocations were also regenerated during the grain elongation, resulting in the refinement of the dislocation sub-structures. Cavity

nucleation and growth occurred in association with the increase of creep strain. The morphology of the cavities changed from a small spherical shape at low strain to a large crack-like cylindrical shaped with an orientation along the rolling/loading direction at high strain. The cavity volume fractions were observed to increase as a function of creep strain.

In contrast, the microstructure in Al6061 exhibited distinct features for 300ºC and 400ºC strained samples. The increase in ductility of Al6061 was small during 300ºC creep tests but significant at 400ºC. About 20% and 60% creep strains were developed before facture in tests at 300ºC and 400ºC, respectively. Thus grains were only slightly elongated in 300ºC strained samples, but exhibited large grain aspect ratios during 400ºC creep test. Compared to Al5083, relatively low cavitation was exhibited in Al6061 strained samples due to the limitation in the elevated temperature ductility. The cavities which did form remained spherically shaped until sample failure. The cavity area fraction in strained samples before failure at 400ºC was only 1.9%. Samples strained at 300ºC exhibited more cavities and as a result exhibit brittle fracture. For samples strained at 400ºC, the combination of higher ductility and low cavitation led to ductile failure.

The distinct observations in stress-induced damage resulted from the differences in creep mechanisms of Al5083 and Al6061. Grain deformation in Al5083 can accommodate small creep strains, but shows incompatibility with larger creep strains. Thus both grain elongation and grain boundary sliding contribute to the creep strain at high strain levels; large cylindrical cavities along tensile direction are developed as a result of grain boundary sliding at high strain. For Al6061, grain deformation can accommodate the creep strain and almost no grain boundary sliding occurs before creep failure. Thus the creep strain is primarily a result of elongation; cavities which do form remain small and spherical until creep fracture.

In order to evaluate the future performance of aluminum structures after fire damage, post-fire uniaxial test were also performed to measure the residual mechanical properties for both alloys. Residual material strength values calculated by deformed cross sectional area after creep tests provide insight into the influence of stress-induced microstructural damage on the post-fire material response. The post-fire performance also exhibited distinct features between the alloys at various exposure temperatures.

Corresponding to the microstructural damage, applied stress had minimal effect on the residual strength of Al5083 during 200°C creep. Dynamic recovery in the 200°C strained sample caused only slight strength degradation in addition to the initial strength degradation caused by static recovery during thermal exposure. For high temperature creep at 300°C and 400°C, the stress effect on the residual strength was minimal at the low strain levels due to low cavitation and minimal grain elongation. At high strain levels, grain elongation and cavitation occurred simultaneously to cause competing effects on the residual strength. During the competing process between dynamic recrystallization and cavitation development, the reduction in strength due to cavitation was counteracted by the strengthening effect of grain elongation. Therefore, subgrain refinement during grain elongation caused an increase in strength over unstressed samples despite significant cavitation at high strain levels.

Al6061 exhibited almost no stress effect on the residual strength for low temperature creep. The major contribution to residual strength degradation at 200°C and 300°C creep tests was the precipitate transformation during thermal exposure. The low ductility before 200°C and 300°C creep failure resulted in no stress influence on the residual strength. The high temperature creep of Al6061 displayed similar behavior with Al5083. Minimal stress effect on residual strength was observed at 400°C creep low strain levels due to low cavitation and minimal grain elongation. At high strain levels, the subgrain strengthening effect caused by grain elongation overcame the weakening effect induced by cavitation. Thus the competing mechanism between grain elongation and cavitation caused an increase in residual strength. Dynamic precipitation had no contribution to residual strength because of the large second phase precipitate formation and dissolution with accumulation of creep strain.

During the competing mechanism between grain elongation and cavitation, grain elongation is the dominant effect to cause increase in true residual strength for both alloys. Cavitation effect is negligible at low cavitation state; thus the true residual yield strength can be represented as the parabolic function of the logarithm of grain aspect ratio. Strength data at high cavitation state also support the statement that the strengthening effect induced by grain elongation overwhelms the weakening effect caused by cavitation.

The engineering residual material strength calculated based on original cross sectional area prior to fire damage is more important for engineering structural design. The initial residual strength

degradation in both alloys is caused by the thermally-induced microstructure changes, i.e., grain structure evolution in Al5083 and precipitates transformation in Al6061, which have great dependence on heat treated temperature. Additional engineering residual strength degradation is caused by the reduction in cross-sectional area during thermo-mechanical process (i.e., it was primarily determined by the material's ductility). In Al5083, high temperature creep will cause highly increase in material's ductility and great reduction in engineering residual strength before creep failure. However, the influence of stress is not that significant in Al6061's engineering residual strength due to limited ductility has been developed during creep.

Thus, during extreme fire-load condition, heated temperature is the primary factor is to determine materials' engineering residual strength in both alloys. About 60% and 70% engineering residual strength have been reduced in Al5083 and Al6061 respectively after material reach 400°C. Reduction in cross-sectional area as a secondary factor is also important to determine additional engineering residual strength degradation in Al5083. Additional 30% residual strength degradation is caused by reduced cross-sectional area before Al5083 creep failure. In contrast, less than 10% residual strength degradation is caused by stress effect before Al6061 creep failure. Therefore, stress effect can be neglected on the engineering residual strength in Al6061due to relative low creep ductility.

6.2 Recommendations for Future Work

While this research has made substantial progress on the linkage between stress-induced microstructural damage and post-fire mechanical properties, some potential research on evaluating post-fire materials response of aluminum alloys is as follows:

- Cavity coalescence and the following creep crack growth at the just-before-fracture state should be analyzed to determine the critical flaw size lead to creep failure.
- TEM observation should be conducted to examine the dislocation and precipitation evolution with the accumulation of creep strain. Strength model based on the dislocation/precipitation density can be considered.
- Compressive creep tests should be performed to study the different stress-induced damage mechanism and its influence on residual mechanical properties. Solid cylinder samples should be designed for the compressive tests.

- The case in which the stress is applied across the sample's rolling direction should be investigated to observe the grain deformation and cavitation development, and their roles in the material's residual strength.
- Multi-axial creep tests should be conducted to analyze the multi-axial stress effect in microstructural damage evolution. Residual mechanical properties data should be collected and correlated to the microstructural damage.
- Residual strength model including grain strengthening, dislocation strengthening, precipitates strengthening and cavitation effect should be developed to predict the post-fire residual strength for aluminum alloys.

Reference:

[1] "Aluminium in shipbuilding " *http://www.aluminiumleader.com/en/around/transport/ship*.

[2] "USS Belknap (CG-26)," *http://en.wikipedia.org/wiki/USS_Belknap_%28CG-26%29*.

[3] "Chief of Navy inspects fire damage to HMAS Bundaberg," *http://news.navy.gov.au/en/Aug2014/Fleet/1302/Chief-of-Navy-inspects-fire-damage-to-HMAS-Bundaberg.htm#.VFKU3rRkukE,* 2014.

[4] B. Allen, "Creep and Elevated Temperature Mechanical Properties of 5083 and 6061 Aluminum," *M.S. thesis, Virginia Tech,* 2012.

[5] P. T. Summers, S. W. Case, and B. Y. Lattimer, "Residual Mechanical Properties of AA5083-H116 and AA6061-T651 after Fire," *Engineering Structures,* vol. 76, pp. 49-61, 2014.

[6] F. A. Leckie and D. R. Hayhurst, "Creep Rupture of Structures," *Proc. R. Soc. Lond. A,* pp. 323-347, 1974.

[7] J. Lin, Y. LIU, and T. A. DEAN, "A Review on Damage Mechanisms, Models and Calibration Methods under Various Deformation Conditions," *International Journal of Damage Mechanics,* vol. 14, pp. 299-319, 2005.

[8] G. Hénaff, G. Odemer, and B. Journet, "Creep and creep fatigue crack growth in aluminium alloys," *Aluminium Alloys, Theory and Applications,* pp. 259-282, 2011.

[9] R. Volkl and B. Fischer, "Mechanical testing of ultra-high temperature alloys," *Experimental Mechanics,* vol. 44, pp. 121-127, Apr 2004.

[10] J. Codrington, P. Nguyen, S. Y. Ho, and A. Kotousov, "Induction heating apparatus for high temperature testing of thermo-mechanical properties," *Applied Thermal Engineering,* vol. 29, pp. 2783-2789, Oct 2009.

[11] "EN 1999-1-2, Eurocode 9: Design of Aluminum Structures," *London: BSI,* 1999.

[12] H. R. Voorhees and J. W. Freeman, "Report on the elevated-temperature properties of aluminum and magnesium alloys," *American Society for Testing Materials, Philadelphia,* 1960.

[13] J. Maljaars, J. Fellinger, and F. Soetens, "Fire exposed aluminium structures.pdf," *HERON,* vol. 50, 2005.

[14] J. Maljaars, "Heating of Aluminium exposed to fire.pdf," *TNO report,* 2005.

[15] "Norsk Standard NS 3478, Brannteknisk dimensjonering av bygningskonstruksjoner Beregning (Design for structural members for fire resistance), 1st edition," 1979.

[16] R. D. Matulich, "Post-fire Mechanical Properties of Aluminum Alloys and Aluminum Welds," *M.S. thesis, Virginia Tech,* 2011.

[17] W. Wen and J. G. Morris, "An investigation of serrated yielding in 5000 series aluminum alloys," *Materials Science and Engineering: A,* vol. 354, pp. 279-285, 2003.

[18] J. May, M. Dinkel, D. Amberger, H. W. Höppel, and M. Göken, "Mechanical Properties, Dislocation Density and Grain Structure of Ultrafine-Grained Aluminum and Aluminum-Magnesium Alloys," *Metallurgical and Materials Transactions A,* vol. 38, pp. 1941-1945, 2007.

[19] E. L. Huskins, B. Cao, and K. T. Ramesh, "Strengthening mechanisms in an Al–Mg alloy," *Materials Science and Engineering: A,* vol. 527, pp. 1292-1298, 2010.

[20] G. A. Edwards, K. Stiller, G. L. Dunlop, and M. J. Couper, "The precipitation sequence in Al-Mg-Si alloys.pdf," *Acta Materialia,* vol. 46, pp. 3893-3904, 1998.

[21] M. J. Starinka and A. M. Zahra, "β′ and β precipitation in an Al–Mg alloy studied by DSC and TEM.pdf," *Acta Materialia,* vol. 46, pp. 3381-3397, 1998

[22] A. Simar, Y. Brechet, B. de Meester, A. Denquin, and T. Pardoen, "Microstructure, local and global mechanical properties of friction stir welds in aluminium alloy 6005A-T6," *Materials Science and Engineering a-Structural Materials Properties Microstructure and Processing,* vol. 486, pp. 85-95, Jun 15 2008.

[23] M. E. Kassner and T. A. Hayes, "Creep cavitation in metals," *International Journal of Plasticity,* vol. 19, pp. 1715-1748, 2003.

[24] J. N. Greenwood, D. R. Miller, and J. W. Suiter, "Intergranular cavitation in stressed metals," *Acta Metallurgica,* vol. 2, pp. 250-258, 1954.

[25] H. E. Evans, "Mechanisms of creep fracture," *London : Elsevier Applied Science,* 1984.

[26] H. Riedel, "Cavity Nucleation at Particles on Sliding Grain-Boundaries - a Shear Crack Model for Grain-Boundary Sliding in Creeping Polycrystals," *Acta Metallurgica,* vol. 32, pp. 313-321, 1984.

[27] C. Gandhi and R. Raj, "Intergranular Fracture in Bicrystals .2.," *Acta Metallurgica,* vol. 30, pp. 505-511, 1982.

[28] D. C. Dunand, B. Q. Han, and A. M. Jansen, "Monkman-grant analysis of creep fracture in dispersion-strengthened and particulate-reinforced aluminum," *Metallurgical and Materials Transactions a-Physical Metallurgy and Materials Science,* vol. 30, pp. 829-838, Mar 1999.

[29] C. Chen and E. Machlin, "On a mechanism of high temperature intercrystalline cracking," *AIME TRANS,* vol. 209, pp. 829-835, 1957.

[30] A. Ayensu and T. G. Langdon, "The inter-relationship between grain boundary sliding and cavitation during creep of polycrystalline copper," *Metallurgical and Materials Transactions a-Physical Metallurgy and Materials Science,* vol. 27, pp. 901-907, Apr 1996.

[31] M. H. Yoo and H. Trinkaus, "Interaction of Slip with Grain-Boundary and Its Role in Cavity Nucleation," *Acta Metallurgica,* vol. 34, pp. 2381-2390, Dec 1986.

[32] H. Trinkaus and M. H. Yoo, "Nucleation under Time-Dependent Supersaturation," *Philosophical Magazine a-Physics of Condensed Matter Structure Defects and Mechanical Properties,* vol. 55, pp. 269-289, Mar 1987.

[33] P. M. Anderson and P. G. Shewmon, "Stress redistribution and cavity nucleation near a diffusively growing grain boundary cavity," *Mechanics of Materials,* vol. 32, pp. 175-191, Mar 2000.

[34] D. Hulla and D. E. Rimmera, "The growth of grain-boundary voids under stress," *Philosophical Magazine,* vol. 4, pp. 673-687, 1959.

[35] R. Raj and M. F. Ashby, "Intergranular Fracture at Elevated-Temperature," *Acta Metallurgica,* vol. 23, pp. 653-666, 1975.

[36] R. Raj, "Intergranular Fracture in Bicrystals," *Acta Metallurgica,* vol. 26, pp. 341-349, 1978.

[37] L. E. Svensson and G. L. Dunlop, "Growth-Mechanism of Intergranular Creep Cavities in Alpha-Brass," *Metal Science,* vol. 16, pp. 57-64, 1982.

[38] C. T.J. and J. R. Rice, "The shape of intergranular creep cracks growing by surface diffusion," *Acta Metallurgica,* vol. 21, pp. 1625–1628, 1973.

[39] I. W. Chen, "Mechanisms of Cavity Growth in Creep," *Scripta Metallurgica,* vol. 17, pp. 17-22, 1983.

[40] H. Riedel, "Fracture at High Temperatures.," *Springer-Verlag, Berlin,* 1987.

[41] B. F. Dyson, "Constraints on diffusional cavity growth rates," *Metal Science* pp. 349-353, 1976.

[42] J. W. Hancock, "Creep cavitation without a vacancy flux," *Metal Science,* vol. 10, pp. 319-325, 1976.

[43] W. D. Nix, "Mechanisms and Controlling Factors in Creep Fracture," *Materials Science and Engineering a-Structural Materials Properties Microstructure and Processing,* vol. 103, pp. 103-110, Aug 1988.

[44] A. C. F. Cocks and M. F. Ashby, "Creep fracture by coupled power-law creep and diffusion under multiaxial stress," *Metal Science,* vol. 16, pp. 465-474, 1982.

[45] W. D. Nix, D. K. Matlock, and R. J. Dimelfi, "A model for creep fracture based on the plastic growth of cavities at the tips of grain boundary wedge cracks," *Acta Metallurgica,* vol. 25, pp. 495–503, 1977.

[46] S. Agarwal, P. E. Krajewski, and C. L. Briant, "Dynamic recrystallization of AA5083 at 450 degrees C: The effects of strain rate and particle size," *Metallurgical and Materials Transactions a-Physical Metallurgy and Materials Science,* vol. 39A, pp. 1277-1289, Jun 2008.

[47] X. H. Fan, M. Li, D. Y. Li, Y. C. Shao, S. R. Zhang, and Y. H. Peng, "Dynamic recrystallisation and dynamic precipitation in AA6061 aluminium alloy during hot deformation," *Materials Science and Technology,* 2014.

[48] E. U. Lee, H. H. Kranzlein, and E. E. Underwood, "Dynamic Recovery in Aluminum," *Materials Science and Engineering,* vol. 7, pp. 348–356, 1971.

[49] G. E. Totten and D. S. MacKenzie, "Physical Metallurgy and Processes," *Handbook of Aluminum* vol. 1, 2003.

[50] H. J. Mcqueen and E. Evangelista, "Substructures in Aluminum from Dynamic and Static Recovery," *Czechoslovak Journal of Physics,* vol. 38, pp. 359-372, 1988.

[51] E. V. Konopleva, H. J. Mcqueen, and E. Evangelista, "Serrated Grain-Boundaries in Hot-Worked Aluminum-Alloys at High Strains," *Materials Characterization,* vol. 34, pp. 251-264, Jun 1995.

[52] R. A. Yund and J. Tullis, "Compositional Changes of Minerals Associated with Dynamic Recrystallization," *Contributions to Mineralogy and Petrology,* vol. 108, pp. 346-355, 1991.

[53] G. Quan, "Characterization for Dynamic Recrystallization Kinetics Based on Stress-Strain Curves," *Recent Developments in the Study of Recrystallization,* vol. Chapter 2, 2013.

[54] H. E. Vatne, K. Marthinsen, R. Orsund, and E. Nes, "Modeling recrystallization kinetics, grain sizes, and textures during multipass hot rolling," *Metallurgical and Materials Transactions a-Physical Metallurgy and Materials Science,* vol. 27, pp. 4133-4144, Dec 1996.

[55] E. O. Hall, "The Deformation and Ageing of Mild Steel: III Discussion of Results " *Proceedings of the Physical Society. Section B,* vol. 64, p. 747, 1951.

[56] H. J. Bunge, F. Wagner, P. I. Welch, and P. Vanhoutte, "A New Way to Include the Grain Shape in Texture Simulations with the Taylor Model," *Journal De Physique Lettres,* vol. 46, pp. 1109-1113, 1985.

[57] S. Sun and V. Sundararaghavan, "A probabilistic crystal plasticity model for modeling grain shape effects based on slip geometry," *Acta Materialia,* vol. 60, pp. 5233-5244, Aug 2012.

[58] R. Liu, M. Salahshoor, S. N. Melkote, and T. Marusich, "A unified internal state variable material model for inelastic deformation and microstructure evolution in SS304," *Materials Science and Engineering a-Structural Materials Properties Microstructure and Processing,* vol. 594, pp. 352-363, Jan 31 2014.

[59] H. J. Roven, M. P. Liu, and J. C. Werenskiold, "Dynamic precipitation during severe plastic deformation of an Al-Mg-Si aluminium alloy," *Materials Science and Engineering a-Structural Materials Properties Microstructure and Processing,* vol. 483-84, pp. 54-58, Jun 15 2008.

[60] M. Cabibbo, E. Evangelista, and M. Vedani, "Influence of severe plastic deformations on secondary phase precipitation in a 6082 Al-Mg-Si alloy," *Metallurgical and Materials Transactions a-Physical Metallurgy and Materials Science,* vol. 36A, pp. 1353-1364, May 2005.

[61] E. Evangelista, A. Forcellese, F. Gabrielli, and P. Mengucci, "Microstructural behaviour of hot deformed AA 6015 alloy," *International Journal of Materials and Product Technology,* vol. 5, pp. 84-94, 1990.

[62] Y. N. Wu, H. C. Liao, Y. B. Liu, and K. X. Zhou, "Dynamic precipitation of Mg2Si induced by temperature and strain during hot extrusion and its impact on microstructure and mechanical properties of near eutectic Al-Si-Mg-V alloy," *Materials Science and Engineering a-Structural Materials Properties Microstructure and Processing,* vol. 614, pp. 162-170, Sep 22 2014.

[63] H.-T. Yao, F.-Z. Xuan, Z. Wang, and S.-T. Tu, "A review of creep analysis and design under multi-axial stress states," *Nuclear Engineering and Design,* vol. 237, pp. 1969-1986, 2007.

[64] H. Kraus, "Creep Analysis," *Wiley, New York.,* 1980.

[65] F. A. McClintock, "A criterion for ductile fracture by growth of holes," *Journal of Applied Mechanics,* vol. 35, pp. 363-371, 1968.

[66] J. R. Rice and D. M. Tracey, "On the ductile enlargement of voids in triaxial stress field," *Journal of the Mechanics and Physics of Solids,* vol. 17, pp. 201–217, 1969.

[67] G. H. Edward and M. F. Ashby, "Intergranular fracture during power-law creep," *Acta Metallurgica* vol. 9, 1979.

[68] L. M. Kachanov, "On creep rupture time.," *Proc. Acad. Sci. USSR Div. Eng. Sci.,* vol. 8, pp. 26-31, 1958.

[69] Y. N. Robotnov, "Creep Rupture," *Proceedings of the XII International Congress on Application Mechanisms. Springer, Berlin.,* 1969.

[70] J. Lemaitre and A. Plumtree, "Application of Damage Concepts to Predict Creep-Fatigue Failures," *Journal of Engineering Materials and Technology,* vol. 101, pp. 284-292, 1979.

[71] D. R. Hayhurst, "CDM mechanisms-based modelling of tertiary creep: ability to predict the life of engineering components," *Archives of Mechanics,* vol. 57, pp. 103-132, 2005.

[72] D. Tabor, "The Hardness of Metals," *Clarendon Press, London,* 1951.

[73] J.R.Cahoon, W.H.Broughton, and A.R.Kutzak, "The determination of yield strength from hardness measrements," *Metallurgical transactions,* 1971.

[74] X. L. Gao, X. N. Jing, and G. Subhash, "Two new expanding cavity models for indentation deformations of elastic strain-hardening materials," *International Journal of Solids and Structures,* vol. 43, pp. 2193-2208, Apr 2006.

[75] K. Kannan and C. H. Hamilton, "Inhomogeneities in initial cavity distribution in a superplastic Al 5083 alloy," *Scripta Materialia,* vol. 38, pp. 299-305, 1998.

[76] N. Chandra and Z. Chen, "Cavity Nucleation in Al5083 Alloys," *Materials Research Society,* vol. 601, pp. 235-246, 2000.

[77] I. C. Hsiao and J. C. Huang, "Deformation Mechanisms during Low- and HighTemperature Superplasticity in 5083 Al-Mg Alloy," *Metallurgical and Materials Transction A,* vol. 33A, pp. 1373-1384, 2002.

[78] F. M. R. Kaibyshev, D.R. Lesuer, T.G. Nieh, "Superplastic behavior of an Al–Mg alloy at elevated temperatures," *Materials Science and Engineering,* vol. A342 pp. 169-177, 2003.

[79] M. Popovic and E. Romhanji, "Characterization of microstructural changes in an Al-6.8 wt.% Mg alloy by electrical resistivity measurements," *Materials Science and Engineering a-Structural Materials Properties Microstructure and Processing,* vol. 492, pp. 460-467, Sep 25 2008.

[80] B. Pan and K. Li, "A fast digital image correlation method for deformation measurement," *Optics and Lasers in Engineering,* vol. 49, pp. 841-847, Jul 2011.

[81] K. H. Tsutomu Tanaka, "Cavitation Behavior in Superplastically Deformed Zn-22 mass%Al Alloy at room temperature," *Materials Transactions,* vol. 45, pp. 2547-2551, 2004.

[82] M. K. Rao, B. P. Kashyap, and A. K. Mukherjee, "Cavity growth during superplastic deformation in 7475 aluminum alloys," *Pergamon Press, Oxford,* pp. 2311-2317, 1984.

[83] A. C. F. Cocks and M. F. Ashby, "Intergranular fracture during power-law creep under multiaxial stresses " *Metal Science,* vol. 14, 1980.

[84] B. Budiansky, J. W. Hutchinson, and S. Slutsky, "Void growth and collapse in viscous solids," *Mechanics of Solids,* vol. The Rodney Hill 60th Anniversary Volume, 1982.

[85] J. P. Li, J. Shen, X. D. Yan, B. P. Mao, and L. M. Yan, "Microstructure evolution of 7050 aluminum alloy during hot deformation," *Transactions of Nonferrous Metals Society of China,* vol. 20, pp. 189-194, Feb 2010.

[86] G. Z. Quan, Y. P. Mao, G. S. Li, W. Q. Lv, Y. Wang, and J. Zhou, "A characterization for the dynamic recrystallization kinetics of as-extruded 7075 aluminum alloy based on true stress-strain curves," *Computational Materials Science,* vol. 55, pp. 65-72, Apr 2012.

[87] S. H. Goods and W. D. Nix, "Coalescence of Large Grain-Boundary Cavities in Silver during Tension Creep," *Acta Metallurgica,* vol. 26, pp. 753-758, 1978.

[88] X. S. Li, L. Z. Wu, J. Chen, and H. B. Zhang, "New approach for modeling flow stress of aluminum alloy 6A10 considering temperature variation," *Transactions of Nonferrous Metals Society of China,* vol. 20, pp. 1482-1487, Aug 2010.